Università degli Studi di Milano
Facoltà di Scienze e Tecnologie
Corso di Laurea Magistrale in Fisica

VIBRATIONAL MODES IN THE CRUST OF NEUTRON STARS

Tesi di Laurea di
Valentina Craveia
Matricola
808522

Relatore: Prof. Gianluca Colò
Correlatore: Prof. Pierre Massimo Pizzochero
Correlatore: Dott. Xavier Roca-Maza

Anno Accademico 2015-2016

In conclusione di questo percorso,
non posso che rivolgere un pensiero ai presenti e agli assenti, a tutti quelli che mi hanno accompagnata lungo il cammino e che hanno contribuito a rendere indimenticabili gli anni universitari.
Un grazie a Gabriele,
per i pomeriggi di studio e lo scambio incessante di appunti.
Un grazie a Giuliano,
per avermi trasmesso la passione per questa affascinate disciplina.
Un grazie a Federica, Cristina, Chiara, Marta,
per dimostrami come la lontananza sia semplicemente un ostacolo immaginario e come i tanti anni di amicizia condivisa siano un ottimo pretesto per brindare assieme con quell'ultimo bicchiere di troppo.
Un grazie ad Enrica e ad Elsa,
per i momenti di svago e per il calore familiare.
Un grazie alle mie nonne Giancarla e Giuliana,
per le lodi smisurate dopo ogni esame superato
e per l'affetto che solo i nonni sanno dare.
Un grazie ai miei genitori Anna e Roberto,
per aver risposto ai miei mille perché da piccola e che ora si divertono a sottopormi i più disparati quesiti scientifici, per il tempo concessomi, la pazienza dimostrata,
per i piccoli grandi gesti d'amore quotidiani.
Un grazie speciale a Dario,
per avermi incoraggiata, supportata e in alcuni casi sopportata, per aver avuto completa fiducia nelle mie capacità e per avermi ricordato che lo studio è importante,
ma anche il riposo è sacro, soprattutto se meritato.
Un grazie a chi ha creduto in me tanto da spingermi a sognare di arrivare fin sulla Luna a bordo di un razzo spaziale costruito nel capanno di casa.
A tutti loro dedico la mia tesi.

Contents

Introduction

Neutron stars are among the most fascinating objects in the Universe. Born from the catastrophic gravitational core collapse of massive stars during type-II supernova explosions, neutron stars are extraordinarily compact, with masses of the order of 1-2 solar masses and radii of about 10 kilometers, and consequently internal densities around the nuclear saturation density $n_\infty = 0.16$ fm^{-3} (2.8×10^{14} g cm^{-3}).

Since the theorization and the much later discovery of neutron stars, these objects have attracted growing interest for their peculiarities: their extreme macroscopic stellar properties (e.g. rotational frequencies up to several hundreds times per second, maximum magnetic fields $\sim 10^{14}$ G and mean temperatures around 10^8 K) are complemented by their extreme microscopic nuclear properties (e.g. bulk superfluidity, central density larger than $\approx 3n_\infty$, neutrino reactions). They are ideal astrophysical laboratories for testing theories of dense matter physics and provide connections among nuclear physics, particle physics and astrophysics.

One of the most intriguing challenges is to design an appropriate equation of state to describe the matter inside the neutron star. In spite of considerable progresses during recent years, the current physical knowledge can not supply an accurate enough equation of state. The understanding of dense matter is far from been completed, particularly for densities larger than the nuclear density where particles heavier than nucleons, or perhaps even deconfined quarks, may show up.

The theoretical problems in nuclear physics are that not only the correct form of the nuclear potential is still uncertain but also that a fully satisfactory many-body computational method for solving the Schrödinger equation, given a potential, remains to be developed. Also, even if it could be done, the possible degrees of freedom to be included in equations to describe the matter above the nuclear saturation density are unknown. Under the experimental point of view, laboratory data that may reproduce neutron star conditions are impossible to obtain (in accelerators, where high density matter is produced, the thermal energies of the particles are much bigger then their rest masses; in neutron

stars however, due to strong gravitational field, we have the possibility to study cold dense matter). Despite the existence of NS masses measured in a quite accurate way and the fact that they can provide some constraints regarding the matter composition, there are no such rigorous observations about the mass-radius relation of neutron stars (because of the difficulties in measuring the dimensions of such small objects, in comparison with other astrophysical objects) which may give more restrictive boundaries.

Since neutron stars are also seismic active objects, the observational data and the study of the crustal excitations may lead to relevant information about the composition of the crust and the thermal relaxation of the whole star. The aim of this work is to develop a model to describe the matter inside the neutron star crust, with particular attention on the inner crust, in order to calculate the velocities of the vibrational modes. From the values of the velocities it is possible to obtain some useful quantities such as for example the heat capacity associated with the crust. These quantities can be eventually compared with observational data or with other theoretical models.

In our model we consider the crust as made up by a lattice of neutron-rich nuclei surrounded by a superfluid of dripped neutrons and a gas of ultrarelativistic electrons in Wigner-Seitz approximation. We use the compressible liquid drop model approach to describe the energy of nuclei, various types of equations of state to describe the nucleons and the free Fermi gas energy for electrons. Vibrational modes are studied employing a superfluid hydrodynamical approach, in which we consider the effects of coupling between the lattice and the superfluid, and of entrainment of dripped neutrons by the lattice nuclei.

Even if the composition of the crust is reasonably understood, some details may not. We show an example of such variety making a comparative analysis between our model and others known in literature, underlining differences and similarities concerning the structure of the matter in the crust and the velocities of the collective excitations. Moreover, we make a sensitivity analysis under the variation of few parameters of the employed nuclear effective interaction, i.e. we study if the composition of the matter and the velocities values may have a dependence on the variation of the symmetry energy coefficient, the effective mass of neutrons and protons and the bulk modulus. We also evaluate the effects due to the neutron entrainment on the velocities. As an application, we calculate the heat capacity contributions for the different constituents of the crust and we briefly discuss how entrainment may affects the results.

Chapter 1

Generalities about neutron stars

1.1 Characteristics of neutron stars

1.1.1 Formation

A neutron star corresponds to the collapsed core of a massive ordinary star, with more than $8M_{\odot}$, at the end of its life, as a consequence of a type-II supernova explosion. The proto-neutron star (the newly formed neutron star), with approximate mass around $M_{\odot}$ and radius of about 20 km, initially rich in leptons (mostly electrons and ν_e), rapidly compresses because of neutrino emission and consequently pressure loss. This provokes the neutronization of the matter (forcing electrons and protons to combine and making the matter more neutron-rich) and the growth of the core temperature until 6×10^{11} K. However, after few seconds, the steady flow of neutrinos begins to cool the interior till the average temperature reaches 10^8 K in few years. The final result is a neutron star with average mass of $1.4M_{\odot}$ and radius approximately 10-12 km.

As the core of the star collapses, its rotation rate increases as a result of the conservation of angular momentum; the consequence is that the newly formed neutron star swiftly rotates, with a period ranging from 10^{-3} s to 10 s. Concerning the magnetic field, the high values of B arise naturally from the collapse of a main sequence star with a typical "frozen-in" surface magnetic field of 100 G. The decrease in radius by a factor of $\sim 10^5$ leads to an increase in the magnetic field by a factor $\sim 10^{10}$ (*1*). This mechanism however does not explain all observed magnetic fields which can reach at the surface up to 10^{14} G (*1*).

1.1.2 Structure

We can have an approximate idea of the structure of neutron stars (NSs) by imagining as it is formed by a thin solid crust floating on superfluid mantles. Specifically, its structure is described by a layering configuration, in which the concentric shells are identified by characteristic densities and composition of the matter (*1*, *2*). The *surface*, $n < 10^{-10}$ fm^{-3} ($\rho < 10^{6}$ g cm^{-3}), is the outer part of the NS: it is composed by ordinary iron nuclei and its thickness is about few centimetres. The *outer crust*, $n \sim 10^{-9} - 10^{-5}$ fm^{-3} ($\rho \sim 10^{7} - 10^{11}$ g cm^{-3}), is made by ionized exotic nuclei, rich in neutrons and arranged in a Coulomb lattice in β equilibrium with relativistic degenerate electron gas, while the *inner crust*, $n \sim 10^{-5} - 10^{-2}$ fm^{-3} ($\rho \sim 10^{11} - 10^{14}$ g cm^{-3}), also presents a superfluid neutron gas. At $n \sim 10^{-1}$ fm^{-3} (few 10^{14} g cm^{-3}) there is a transition region called the *mantle*, composed by nuclear clusters, superfluid neutrons and electrons. The core region, $n > 0.15$ fm^{-3} ($\rho > 10^{14}$ g cm^{-3}), is divided into the *outer core*, uniform nuclear matter of superfluid neutrons with a small concentration of electrons and superfluid protons, and the *inner core*. The more accredited phenomena which may exist in NS core are: a Bose-Einstein condensate of pions, free quark, abundance of hyperons. The composition of this region depends on the EoS and consequently on the typical densities permitted; typical densities allowed vary from 3 up to 10 times the

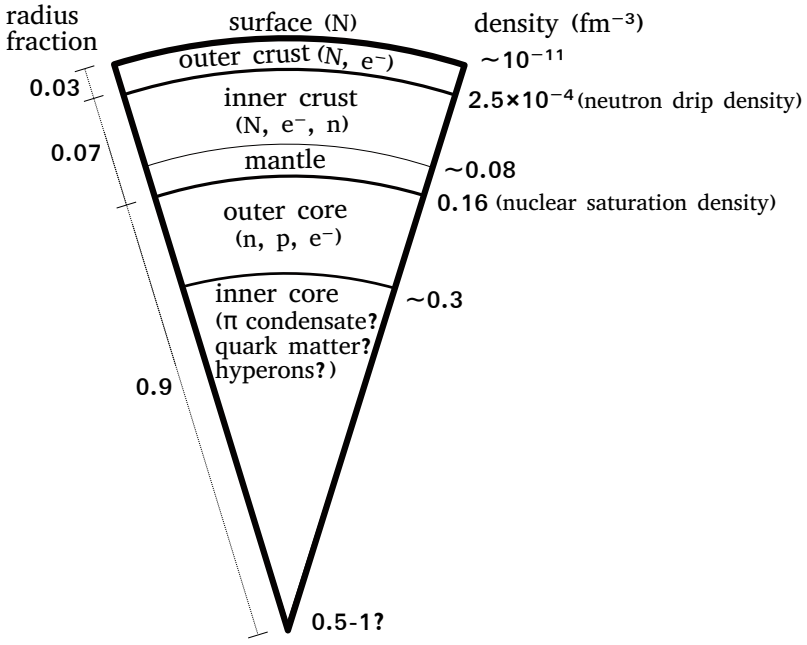

Figure 1.1: Cross section of a NS illustrating the structure and the regions discussed in the text.

saturation density.

Neutron stars may be classified according to the core composition. Ordinary NS are made by standard hadronic matter; because of the high densities supposed for the core, it is proper to consider also Hyperonic NS and Hybrid NS, whose interiors contain a combination of exotic particles permitted by the physics of strong interactions (hyperons alone or with a mixture of deconfined quarks). It is generally assumed that pulsars and other observed neutron stars belong from these categories. However, following the Bodmer-Witten hypothesis, strange quark matter (SQM) NSs are also theorized. A relevant difference between the more classic NS and the SQM stars is that the latter are self-bound by means of the strong force, so gravity is not required to hold them together.

1.1.3 Properties

To summarize, a neutron star has a typical mass of $1.4M_{\odot}$ and a radius of 10 km, is characterized by a wide range of densities that spans about 10 orders of magnitude, with ordinary matter at the surface and a central density a few times higher than the saturation density (even if the exact value is unknown). It rotates at up to several hundred times per second, presents high magnetic field up to 10^{14} G and an average mean temperature of 10^8 K (*3*). Currently, only a few aspects of neutron stars can be inferred from observations, such as masses for NSs in binary systems (timing the pulse and mapping an orbit, even if such a measure is quite complicated), approximate ages knowing the period of pulsation and its time derivative, spin rates and magnetic field strengths.

Other crucial properties, important for understanding the structure and the evolution of NSs like radii and surface temperatures, may be estimated in a few cases from optical and X-ray observations of cooling neutron stars as well as from X-ray bursts and flares occurring on neutron star surfaces (*4*).

For a comprehensive study of neutron stars it is required to have an understanding of the interplay between the long-range gravitational and electromagnetic interactions with the short-range weak and strong nuclear forces. As an example, the choice of the equation of state (EoS) for the nuclear matter influences the relation between mass and radius of the whole NS (*5*). A simultaneous measurement of mass and radius of some average mass neutron stars may help to give more restrictive constraints and to discriminate among the families of possible EoSs. Unfortunately, such a measuring is not currently available, but it is possible to have ranges of values for mass and radius. The minimum stable NS mass is about $1M_{\odot}$ while the maximum limit, which is based on purely general relativistic considerations, is $\sim 3M_{\odot}$ (the maximum observed mass is $\sim 2M_{\odot}$ (*6*)). Beyond this value, neutron stars are believed to collapse into black holes. A realistic range for the total radius is $10.7-13.1$ km

(*7*). The constraints on the radius are given by the Schwarzschild condition $R \leq 2GM/c^2$ and by causality $R \leq 3GM/c^2$. There is also a lower limit for rotation constraint (*5*). A consequence of uncertainty about the EoS in the internal parts is that different models predict a wide range in the pressure value close to the saturation density, which leads to nearly 50% variation in predictions of the radii (*5*). For example, the exotic models which consider the presence of pions and hyperons in the core are correlated to a higher central density and this is supposed to lead to softer EoS (which means smaller neutron pressure at saturation density) and consequently to smaller NS. On the contrary, the stiffer the EoS (and smaller values of the central density), the bigger the NS (*1*).

1.1.4 Pulsars

Neutron stars are observed as pulsars. A pulsar is a highly magnetized object that rotates rapidly and produces beams of electromagnetic radiation at low energy (radio emission) and high energy (X,γ emission). We know that pulsars are Galactic objects because they are concentrated in the Galactic plane and they show dispersion measure characteristics of signal propagation over

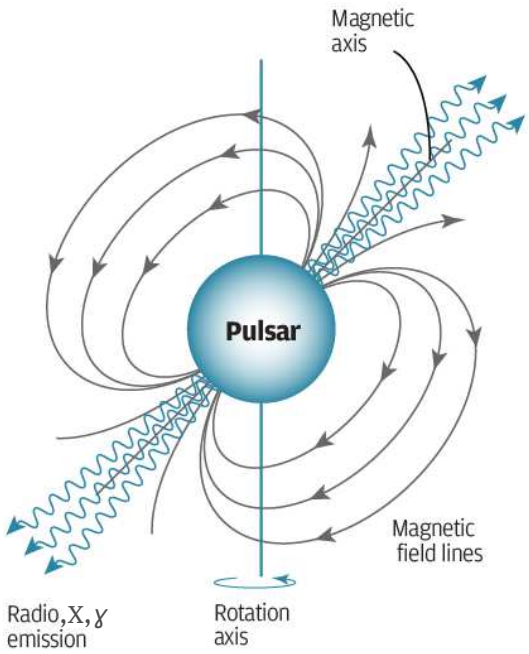

Figure 1.2: A raffiguration of the "lighthouse model"; while the pulsar rotates, electromagnetic radiation is emitted along the magnetic field axis.

Galactic distances (*1*). The pulsing behaviour of the emission is explained as radiation emission by a rotating magnetic dipole, described by the so-called "lighthouse model": in fact a distant observer, if in the right line of sight, sees the rotation of the narrow radiation beam as a pulsation.

Pulsar periods have a remarkable stability, decrease very slowly and do not increase, except for occasional disruptions of the regular pulse called "glitches". Glitches are sudden spin-ups of pulsing period and their behaviour suggest they are global phenomena. The current glitch model involves a massive and sudden transfer of angular momentum from the superfluid to the normal component inside the inner crust, however the detailed mechanism remains uncertain. Glitches observed in the Crab NS with $\Delta\Omega/\Omega \sim 10^{-8}$ and the Vela NS with $\Delta\Omega/\Omega \sim 2 \cdot 10^{-6}$ show that the decrease in period is accompanied by an increase in period derivative, $(\delta\dot{\Omega})/\dot{\Omega} \sim 10^{-4}$ for Crab, $(\delta\dot{\Omega})/\dot{\Omega} \sim 10^{-3}$ for Vela, which decays away in several days (*1*).

It is possible to divide the known pulsars into three classes, according to the mechanism that generates the electromagnetic radiation.

The **rotation-powered pulsars** are NSs for which the loss of rotational energy provides the energy for the beam emission. In this category we have the radio pulsars, isolated neutron stars with strong dipolar magnetic field and high rotational speed, which emit mainly at radio frequencies. Prototypes of this category are the Crab and the Vela NSs.

The **accretion-powered pulsars** are neutron stars in binary systems in which the periodic pulse is due to gravitational potential energy of accreted matter: material falling from the companion to the NS can form a hotspot that rotates in and out of view, producing X-rays that are observable from the Earth. Moreover, the accretion can strengthen old pulsars and potentially cause them to gain mass and spin-up to very fast rotation rates with a period less than 10 ms, forming the so-called millisecond pulsars. This category includes most but not all X-ray pulsars. A particular scenario is given by a X-ray binary system in which the companion star has a mass $\lesssim M_\odot$, and spectral type A or later, known as a low-mass X-ray binary (LMXB).

The **magnetars** are isolated neutron stars characterized by a huge magnetic field, in some cases more than 10^{14} G (*1*, *8*), for which the decrease of the extremely strong magnetic field provides the energy for the emitting pulsation. Two classes of astronomical objects are believed to be magnetars: the anomalous X-ray pulsars (AXPs) and the soft gamma repeaters (SGRs) (*9*). The AXPs are young magnetars, characterized by narrow periods, ~ 10 s, and are identified as having modest X-ray luminosities, in the range $10^{34} - 10^{35}$ erg s^{-1} (*10*). The SGRs are astronomical objects which emit large bursts of γ-rays and X-rays at irregular intervals; this phenomena are called *giant flares* with peak

luminosities of $\sim 10^{44} - 10^{46}$ erg s^{-1}, various orders of magnitude higher than the quiescent SGR luminosity. Giant flares are typically followed by a decaying tail which may last $\sim$ 100 s. The timing analysis of the decaying tail revealed several quasi-periodic oscillations (QPOs), which indicates a quasi-periodic behaviour in X-ray emissions and whose frequencies are included between $18 - 1800$ Hz. QPOs in SGRs have been commonly interpreted as shear modes, excited from crustal deformations during the flare.

In fact neutron stars are seismically active bodies. Oscillations are produced by crustal glitches, by the impact of accreting matter and by thermonuclear explosions. This seismic activity may be manifest as quasi-periodic microstructure in radio pulsar, as periodicity in bursting X-ray sources, as gamma-ray bursts or as quasi-periodic oscillations in nonpulsing, low mass X-ray binaries (*11*). An important and interesting event interrelated with oscillations is the emission of gravitational waves from the excited modes (*12*). In fact the crust can support non-axial deformations which, combined with rapid rotation, could generate gravitational radiation (*13*). Gravitational waves themselves damp the oscillations, so it is required to estimate the decay timescale for gravitational radiation damping. Moreover, the gravitational wave emission may be detectable, and so could provide independent measurements of frequencies and damping times.

The generation of oscillations in pulsars is one of the reasons for which they are studied. In particular, neutron stars are useful for the study of stellar seismology mainly because they offer a good prospects for supporting observable shear modes with respect to other astrophysical compact objects. Being the crust the only solid component of the whole NS, it is subject to fracture and vibrations, allowing the production and the propagation of crustal oscillation modes. Since the crust is thin (compared with the total radius) and subject to little friction from the liquid core below, large-amplitude shear oscillations could be excited with much less energy than it would be required in solid bodies.

1.2 The neutron star crust

There are several reasons why the neutron star crust plays an important role in many observational findings on neutron stars. Even if it contains only a small percentage of the total mass of a NS, the crust is crucial for many astrophysical phenomena (*2*), determining the stability and the structure of NS (*14*) and taking part during the core collapse of the supernovae (*15*).

Heat transport and magnetic field evolution in the crust are sensitive to the composition of the crust; any emission eventually coming from the core must

flow through its layers. This, in turn, might influence various transport properties such as electrical and thermal conductivities, shear modulus and shear viscosity in the crust (*16*). The heat capacity and the thermal conductivity, and to a less extent neutrino emissivity (*17*), of the inner crust influence the whole cooling process of the NS (*13*, *18*) and contribute to determine the duration of the thermal relaxation process (*2*, *19–21*). Moreover, it is thought that oscillations could lead to instabilities responsible for glitches in pulsar timing and quasi periodic oscillations in SGRs (*2*, *20*, *22*).

Neutron star crusts are cosmic laboratories suitable to demonstrate various hypothesis of theoretical physics and hopefully to confront with neutron star observations.

1.2.1 Composition

After the atmosphere, the crust is the most external part of a neutron star and its thickness is around the 10% of the total radius of a typical neutron star. This region is divided into two parts, the outer crust and the inner crust. The outer crust is composed by completely ionized neutron-rich nuclei arranged in a lattice and surrounded by a Fermi gas of electrons. The thickness of the outer crust is about few hundred meters and includes a wide range of densities.

The outer crust is defined to start at densities of the order of 10^{-11} fm^{-3} (10^4 g cm^{-3}) where complete ionization occurs and to end at the neutron drip density $n_{drip} \approx 2.5 \times 10^{-4}$ fm^{-3} ($\rho_{drip} \approx 4 \times 10^{11}$ g cm^{-3}) where it starts to be energetically favourable that neutrons in nuclei drip. This represents the end of the outer crust and the beginning of the inner crust.

The inner crust is then formed by heavy neutron-rich nuclei disposed in a lattice, in coexistence with a gas of dripped neutrons and surrounded by an electron gas. Within a more realistic picture photons, positrons, α particles and free protons are thought to be present in the inner crust although frequently their effects are neglected in the study of the equation of state (EoS), because some of them are present in small fraction and they do not alter the EoS, and eventually both the reasons.
The inner crust extends for ~ 1 km, till around the nuclear saturation density $n_\infty = 0.16$ fm^{-3} ($\rho_\infty = 2.8 \times 10^{14}$ g cm^{-3}), in accordance with the beginning of the outer core which is formed by uniform nuclear matter, mostly composed by neutrons with a small fraction of protons and electrons. At lower densities, down to $\sim 0.5 n_\infty$ the inner crust contains only spherical nuclei (*13*). Once reached the approximate density of $0.06 - 0.08$ fm^{-3} (*13*, *19*, *23*), inhomogeneous phases of nuclear matter should be considered, since spherical nuclei are so closely packed that global deformation could occur. Actually, the bottom layers of the inner crust, also called the mantle, are characterised by possible

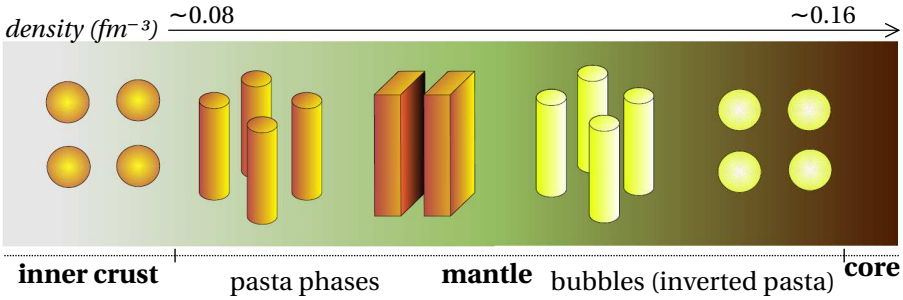

Figure 1.3: Example of possible shapes of nuclear clusters in the bottom layers of the inner crust, in order spheres, rod, slab, tube and spherical bubble. For pasta phases neutrons and protons are inside the nuclear clusters and superfluid neutrons are outside. For inverted pasta the superfluid gas is immersed in a denser phase composed by protons and neutrons.

changes of the nuclear shapes that are energetically favoured (*24*, *25*), such as rod, slab, tube and bubble-like (see e.g. (*23*)). These exotic shapes are usually called *nuclear pasta*.

1.2.2 Temperature and entrainment

Generally, the characteristic energy required for nuclear excitations are larger than the typical thermal energy (*24*). The average temperature of $T = 10^8$ K for all but the youngest neutron stars corresponds to a thermal energy contribution of $\sim 10^{-2}$ MeV. The superfluid energy gap Δ is the latent heat associated with the phase transition to a paired state (*1*). The gap energy Δ depends on the strength of the pairing interaction and, in turn, on the density. At nuclear densities the typical superfluid gap energies of neutrons and protons are ~ 1 MeV. Since $T \ll \Delta$, the effects due to the temperature do not affect the dynamic of nucleons, so the nuclear matter can be considered with a good approximation to be in its ground state at zero temperature ((*26*) for a further discussion).

In the approximation of zero temperature (when the value of T is below the critical temperature T_c defined in (*27*)), part of neutrons outside the nuclei with opposite spins and zero orbital angular momentum forms Cooper's pairs. This phenomenon is similar to the formation of Cooper's pair of electrons in conventional superconductors. These pairs are considered as bosons and they behave coherently on a very large scale, as if they constitute a neutron condensate. These neutrons are so called *superfluid* because they can flow without any viscosity. A first evidence for superfluidity in NS has been discussed in (*28*) after the discovery of the first pulsars, in connection with the observation

of glitches. The superfluid character of NS matter should not be neglected because induces collective excitations of the neutron gas, which can give an important contribution to the heat capacity in certain regions (*29*). Regardless the superfluid behaviour, some neutrons may still be *entrained* by the lattice nuclei in the crust (*29*). Entrainment is a non-dissipative effect that arises in the crust, in particular it has been theoretically estimated to be very strong especially in the intermediate region of the inner crust at average baryon densities $n \sim 0.02 - 0.03$ fm^{-3} (*30*)). It arises by the fact that free neutrons can be elastically scattered by the lattice (*31*, *32*) and then can not propagate. These neutrons, reflected by the lattice, can interfere constructively but only for specific incident angles given by Bragg's law. Scattered neutrons are so called entrained because their dynamic is coherent with the lattice.

1.2.3 Equations of state

At the lower densities of the outer crust, the matter does not have a very large neutron excess in general. Actually, experimentally measured nuclei in laboratory are thought to form such layers of the outer crust. Once the neutron excess in nuclei becomes larger, properties of nuclei can only be extrapolated through the nuclear mass models. Under extreme conditions of density and neutron asymmetry, current model predictions widely differ (*33*, *34*). The formation of the different structures at the bottom of the inner crust strongly depends on the effective nucleon-nucleon interaction, in particular on the strength of the nuclear surface energy (*35*) (caused by the increasing number of bound nucleons and consequently increasing value of binding energy, since larger radius means smaller surface energy) and the Coulomb energy (*17*) (because the distances between nuclei became comparable with the nuclear sizes). This prediction has been confirmed within different models (*36*) assuming zero temperature that is a good approximation for cooled neutron stars, since at some critical temperature (of the order of several MeV) the pasta structures may disappear due to thermal excitations (see (*17*) and references wherein it). It is therefore possible to have different shapes of nuclear cluster which coexist (*19*, *37*), depending on the characteristics of the model. The study of nuclear pasta is important because exotic nuclei would lead to modified transport and elastic properties of the crust, compared to a classical Coulomb lattice formed by spherical nuclei (*25*).

There are different approaches to describe matter into the NS crust, which consistently incorporate effects caused by increasing densities into nuclear models (see for example (*19*, *21*, *38*, *39*)).

Microscopic models, as the works (*19*, *39*) based on Hartree-Fock calculations, are of great interest because they can take into account quantal effects

which are not treated in a classical approach, but it can be sometimes difficult to understand the most relevant physical properties useful to characterise the inner star crust. Semi-classical models (Thomas-Fermi approximation and its extensions) and classical models, like the compressible liquid drop model (CLDM, introduced by (*24*)) in (*38*, *40*, *41*), are widely used because, despite their simplicity, they offer a way to better understand the most important physical mechanisms at work.

Chapter 2

Theoretical model for the inner crust

In this thesis, we study the NS inner crust by adopting the following model: nuclei are arranged in a body-centered cubic (bcc) lattice in coexistence with a gas of dripped neutrons and are surrounded by an electron gas (*14*). The equilibrium structure is expected to be a bcc lattice, since this gives the smallest lattice energy (see for example (*1*)). Part of the dripped neutrons, that we name outside neutrons, forms a superfluid gas while the rest that are not strictly bound to the lattice nuclei are assumed to be entrained: together with the neutrons inside nuclei we call them inner neutrons. Electrons are treated as ultrarelativistic particles (see Appendix C for a more detailed discussion).

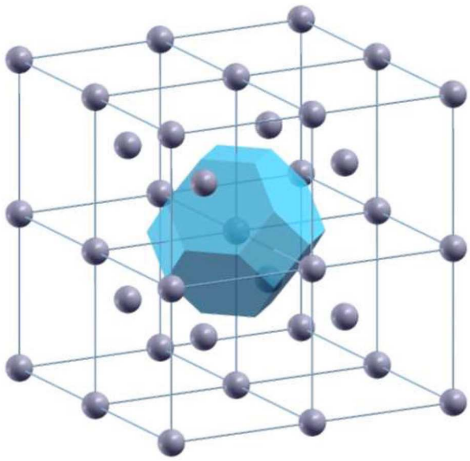

Figure 2.1: Wigner-Seize cell of a body-centered cubic lattice (from (*2*)).

We work in the Wigner-Seitz approximation (*42*), which means that the physical unit cell of the lattice is replaced by one of equal volume with the same

geometry of the nuclear cluster (*43*), that we assume to be spherical. WS cells are approximated as spheres because it is both the simplest choice and it is convenient to compare the cell radius and the nucleus radius. We consider to have one spherical nucleus located at the center of a symmetric spherical cell which is filled with the gas of superfluid neutrons and electrons. The various cells are not in contact with each other, i.e. they are isolated and independent and can not exchange particles, so the total baryonic number per cell must be constant. We also impose charge neutrality inside every WS cell. The uniform charge distribution is the simplest choice in order to avoid any spurious effect caused by a local charge imbalance.

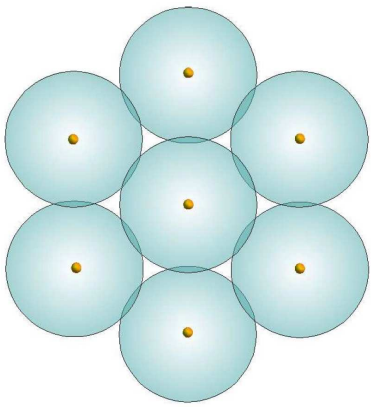

Figure 2.2: Example of a two-dimensional crystal in WS approximation: it is composed by spherical cells centered around the nuclei at each site of the lattice (from (*2*)).

The most relevant variables characterising our system, describing the cell and the matter inside, are the following: the radius of the WS cell r_C, the nuclear radius r_N, the total baryon number density n, the densities inside nuclei n_i and outside nuclei n_o, the electron number density n_e. It is also important to know the ratio of protons (or electrons) and neutrons, so we use the total proton fraction Y_e and the proton fraction inside nuclei Y_i.

We decide to use the Helmholtz energy, as in (*38*), instead of the Gibbs energy (*44*). At zero temperature, the Helmholtz free energy $F = E - TS$ is equivalent to the total internal energy E in our system. We define the energy per baryon $e = \frac{E}{A}$, where A is the total baryon number inside the cell, and the energy per volume (energy density) $\epsilon = \frac{E}{V_C} = ne$, where $V_C = \frac{4\pi}{3}{r_C}^3$ is the volume and r_C the radius of the Wigner-Seitz cell. The nuclear volume is defined as $V_N = \frac{4\pi}{3}{r_N}^3$, where r_N is the nuclear radius. We can write $A = A_i + N_o = Z + N_i + N_o$, where Z is the total proton number, N_i the neutron number inside nuclei and N_o the neutron number outside nuclei.

It follows that the densities for the different species are defined as:

$$n = \frac{A}{V_C} = n^p + n^n$$

is the baryon density, given by the sum of the total neutron and proton densities;

$$n_i = \frac{A_i}{V_N} = n_i^p + n_i^n$$

is the density "inside" nuclei, given by protons and neutrons both bound and entrained;

$$n_o = \frac{N_o}{V_C - V_N} = n_o^n$$

is the density of the superfluid neutron gas;

$$n_e = \frac{Z}{V_C}$$

is the density of the electron gas (we use Z because of charge neutrality).

Because the cell radius is bigger than the nuclear radius, the volume occupied by the nucleus is just a fraction of the total volume. We define the fraction occupied by nuclei as $u = \frac{V_N}{V_C}$; consequently, $1 - u$ indicates the fraction of volume available for the neutron gas. On the other hand, we suppose that electrons occupy all the volume V_C and simply permeate the whole space (Appendix C). Finally, we describe the total proton fraction as $Y_e = \frac{Z}{A}$ and the proton fraction inside nuclei as $Y_i = \frac{Z}{A_i}$. The dimensions of our variables are the following: energy per baryon in MeV, energy density in MeV fm^{-3}, density in fm^{-3}, radius in fm, volume in fm^3.

The purpose of the following sections is to write the equations of interest and give the equilibrium conditions.

2.1 Energy contributions

We now describe the different contributions to the total energy of our system. The total energy density is given by the sum of three different terms (see also Appendix B)

$$\epsilon = \epsilon_e + \epsilon_o + \epsilon_N, \tag{2.1}$$

where ϵ_e indicates the energy density of the electron gas, ϵ_o describes the neutron gas and ϵ_N is the energy associated with the nucleons in the nucleus.

We consider only the most relevant species of the inner crust (neutrons, protons and electrons), omitting the presence of negligible components (like α particles, photons, etc.) because their presence is not relevant for our study and to keep our model the simplest possible (for more details see (*19*, *24*, *29*, *41*, *45–47*)). We decide to construct our model with a classical approach, in which the nuclei in the inner crust are described by taking the compressible liquid drop model (CLDM) with some empirical parameters derived from avaliable Skyrme functionals. In this model by definition shell effects are neglected. We decide to take $T = 0$ K in order to completely avoid nuclear excited states, but also to neglect thermal energy, and to consider the matter to be in β equilibrium.

In the simplest form, the energy of a nucleus for the liquid drop model may be written as (*24*)

$$\epsilon_N = \epsilon_{bulk} + \epsilon_s + \epsilon_C; \tag{2.2}$$

the term ϵ_{bulk} indicates the volume energy for bulk nuclear matter, which include the kinetic, the volume and the asymmetry terms and it is used to describe the asymmetric and the symmetric matter; ϵ_s is the surface energy and ϵ_C the Coulomb energy. We neglect pairing effects (*24*). The correct dimension of each term is analysed in Appendix B. The choice of the CLDM allows us to separate bulk, surface, Coulomb contributions from the expression of total energy (*24*, *40*, *48*, *49*).

We try to use as much as possible a microscopic input for the energy terms. We choose a microscopic approach to implement the bulk energy term, in particular we use a Skyrme-type effective interaction solved at the mean-field level (*50*).

For the surface contributions we choose the liquid drop model approximation but we also put on some inputs of the Skyrme parametrization, following the approach of (*40*) and used by (*38*, *41*). The Coulomb energy term is written using the approach of the liquid drop model, based on the work (*24*).

2.1.1 Electron gas energy

We consider here only the free electron energy, i.e. the electron Fermi gas energy. All electrostatic electron contributions are included in the Coulomb energy (see subsection 2.1.4) (*24*). Electron screening effects can be ignored because the electron screening length is larger than the distance between ions (*38*, *40*)(see Appendix C). For the typical range of densities in the inner crust,

we use the ultra relativistic expression of the electron Fermi gas (*1*)

$$e_{Fermi} = \frac{3}{4}\hbar c(3\pi^2 n_e)^{1/3}. \tag{2.3}$$

2.1.2 Bulk energy

For the Skyrme parametrization solved at the mean-field level, we write the expression for asymmetric nuclear matter (ANM) (*50*) as

$$\begin{aligned}\tilde{e}_{bulk}(n,Y) =& \frac{3}{10}\frac{\hbar^2}{m}\left(\frac{3\pi^2}{2}\right)^{2/3} n^{2/3}F_{5/3}+ \\ &+ \frac{1}{8}t_0 n[2(x_0+2) - F_2(2x_0+1)]+ \\ &+ \frac{1}{48}t_3 n^{\kappa+1}[2(x_3+2) - F_2(2x_3+1)]+ \\ &+ \frac{3}{40}\left(\frac{3\pi^2}{2}\right)^{2/3} n^{5/3}\Big\{F_{5/3}[t_1(x_1+2)+t_2(x_2+2)]+ \\ &+ \frac{F_{8/3}}{2}[t_2(2x_2+1) - t_1(2x_1+1)]\Big\},\end{aligned} \tag{2.4}$$

where the term

$$F_m = F_m(Y) = 2^{m-1}[Y^m + (1-Y)^m] \tag{2.5}$$

is a function of the proton fraction $Y = \frac{Z}{A}$. A special case of (2.4) is given by the value $Y = \frac{1}{2}$ which indicates the symmetric nuclear matter (SNM). All the quantities t_0, t_1, t_2, t_3, x_0, x_1, x_2, x_3, κ are parameters defined by the particular choice of the Skyrme force. The expression of the bulk energy (2.4) is used in our model to describe nuclear matter (n_i, Y_i) and neutrons outside nuclei (n_o, $Y_o = 0$).

In general, the bulk energy per particle can be expanded around saturation density of SNM, obtaining (*48*, *49*, *51*)

$$\begin{aligned}\tilde{e}_{bulk}(n,Y) =& e_\infty - Y\Delta + \frac{K_\infty}{18}\left(1-\frac{n}{n_\infty}\right)^2 + \\ &+ \left[J + \frac{L}{3}\left(1-\frac{n}{n_\infty}\right)\right](1-2Y)^2 + \dots.\end{aligned} \tag{2.6}$$

where we have introduced different parameters that characterize the EoS around saturation. Those are the saturation density n_∞ and the saturation energy e_∞, the incompressibility of SNM (bulk modulus) K_∞, the symmetry energy at

saturation density J and the symmetry energy density derivative coefficient L (the definitions of the parameters and a brief introduction about the bulk energy are given in subsection 4.3.1). The term $\Delta = 1.293\,\mathrm{MeV}$ is the neutron-proton mass difference and is included because the energy is taken with respect to the neutron rest mass. It comes from the relation $\frac{M(A,Z)}{A} - m_n = -Y\Delta - \frac{BE}{A}$, where $M(A,Z)$ indicates the mass of a nucleus, m_n is the neutron mass and $\frac{BE}{A}$ is the binding energy per baryon given by (2.6) minus the $Y\Delta$ term.

There are several parameters included in the bulk energy term (2.6); some of them are well determined in laboratories under specified conditions (usually for symmetric nuclear metter at zero temperature, close to saturation density), but some others strictly depend on the choice of the nuclear force model. All of them can be empirically estimated.

Their typical values are $n_\infty \approx 0.16\ \mathrm{fm}^{-3}$ and $e_\infty \approx -16\ \mathrm{MeV}$: these two quantities are well known in literature and are considered as constants. For the other parameters we indicate reasonable ranges found in more recent works: $K = 240 \pm 30\,\mathrm{MeV}$ (*52*), $J = 30 \pm 3\,\mathrm{MeV}$ (*53*), $30 \lesssim L \lesssim 120\,\mathrm{MeV}$ (*54*). The importance and the role of these parameters are discussed in chapter 4.

In Appendix A we employ also the model based on the work (*38*) for nuclear matter, as an example of possible parametrization of the bulk energy term.

2.1.3 Surface energy

The nuclear surface energy can be written in a semi-classical approach as (*40*)

$$\tilde{e}_s(r_N, n_i, Y_i) = \frac{4\pi {r_N}^2}{A_i}\sigma(Y_i). \tag{2.7}$$

This functional form comes from the definition of surface tension σ, which is the ratio of the energy over a surface $\sigma = \frac{E}{S}$. In (2.7) we neglect higher order effects (*38*). As the baryon density n grows, the matter inside nuclei becomes more neutron rich and the difference in composition between the matter inside and outside nuclei becomes small, so the surface energy decreases and in the limit of uniform matter (close to the core transition) it vanishes.

In order to respect the conditions of bulk equilibrium across the surface between inside nuclear matter and outside neutron gas, the surface energy depends on the density and on the proton fraction of the nuclear matter, since r_N in our model is written as a function of n_i, Y_i as well (see section 2.2). Using the expression of r_N in (2.21) and the definition of A_i, it may be clear that the surface energy dependences are

$$\tilde{e}_s(n_i, Y_i) \propto \frac{\sigma(Y_I)}{n_i^{1/3}} Y_i^{2/3}.$$

Many parametrizations exist for the surface tension: we decide to take a parametrization based on Thomas-Fermi surface calculations (*55*), used also by (*38*, *40*), in which the surface tension depends on Y_i (*40*) as

$$\sigma(Y_i) = \sigma_s \frac{16+Q}{Y_i^{-3}+Q+(1-Y_i)^{-3}} \text{ [MeV fm}^{-2}] \tag{2.8}$$

and where

$\sigma_s = \sigma(1/2, 0)$ [MeV fm^{-3}] is the surface tension for symmetric nuclear matter (SNM);

$Q = \frac{384\pi {r_o}^2 \sigma_s}{S_s} - 16$ is the surface stiffness coefficient (*38*), which measures the resistance of the system against separation of neutrons from protons to form a neutron skin around the nucleus;

$S_s = -\frac{{A_i}^{1/3}}{8} \frac{\partial^2 e_s}{\partial {Y_i}^2}\Big|_{n_\infty,1/2,0}$ [MeV] is the surface symmetry coefficient (*38*);

$r_o = \frac{r_N}{A^{1/3}} = \left(\frac{3}{4\pi n_\infty}\right)^{1/3}$ [fm] is the radius of the space occupied by a nucleon.

In literature is often used another quantity, the surface energy of SNM a_s instead of our choice of σ_s. The relation to pass from one to the other is

$$4\pi {r_o}^2 \sigma_s = a_s. \tag{2.9}$$

2.1.4 Coulomb energy

The Coulomb energy of our system is the sum of various terms, as described in (*24*): the nuclear Coulomb energy, the interaction energy between nuclei, the nucleus-electron interaction and the electron-electron interaction energy. In our model, we neglect the electron screening since is a small correction to the lattice contribution (*24*).

The nuclear Coulomb energy for an uniformly charged sphere of radius r_N and total charge Zq (where q is the elementary electric charge) is

$$E_n = \frac{3}{5}\frac{Z^2 q^2}{r_N}. \tag{2.10}$$

We neither consider the surface thickness correction nor the proton exchange energy (*38*) that may have some effect but within our approximations can be

neglected. All the other terms are included in the so called lattice Coulomb energy (*14*), which is the energy of a lattice of positively charged nuclei immerse in an uniform gas of electrons in WS approximation (*24*, *38*). If we suppose that the electrons are uniformly distributed, we have that the lattice energy is (*24*)

$$E_L = -\frac{9}{10}\frac{Z^2q^2}{r_N} + \frac{1}{2}\frac{Z^2q^2\,\langle r^2\rangle}{r_C^3}. \tag{2.11}$$

The first term is the lattice energy of a point nucleus, a reasonable approximation of the exact resulting energy for a bcc lattice. The second term is the contribution to lattice energy due to the finite size of the nucleus, i.e. the finite-size correction to the total energy independent by the WS approximation. The term $\langle r^2\rangle$ indicates the mean square radius of a nuclear charge distribution. Considering a uniform proton charge distribution inside nuclei, it becomes $\langle r^2\rangle = \frac{3}{5}r_N^2$ (*24*). The total Coulomb energy per cell is the sum of the previous contributions

$$E_C = \frac{3}{5}\frac{Z^2q^2}{r_N}\left(1 - \frac{3}{2}\frac{r_N}{r_C} + \frac{1}{2}\frac{r_N^3}{r_C^3}\right). \tag{2.12}$$

As the density n increases, r_N becomes larger while r_C diminishes and eventually the matter inside nuclei fills the WS cell: the Coulomb energy decreases its value and goes to zero when r_N goes to r_C (*24*, *40*). We prefer to work with the energy per baryon inside nuclei, so

$$\tilde{e}_C(r_N, n_i, Y_i, u) = \frac{3}{5A_i}\frac{Z^2q^2}{r_N}D(u) = \frac{4\pi}{5}q^2{Y_i}^2{r_N}^2 n_i D(u). \tag{2.13}$$

The function $D(u) \equiv 1 - \frac{3}{2}u^{1/3} + \frac{1}{2}u$ simply represents all the electrostatic corrections to a uniform charge sphere due to the presence of the lattice and to the finite size of the nuclei in terms of the volume fraction u.

2.1.5 Total energy

We finally have the total energy, given by the sum of all the contributions

$$e = e_e + e_o\frac{n_o}{n} + e_N\frac{n_i}{n}. \tag{2.14}$$

where, for the CLDM

$$e_N = e_{bulk,i} + e_s + e_C; \tag{2.15}$$

(for more details see Appendix B).

Since nuclei form a Coulomb lattice and we are at zero temperature, we can neglect translational energy and all the other thermal contributions.

2.2 Equilibrium conditions and equations

Summarizing, the expressions of the energy for the different species in our model are:

- electron ultra relativistic Fermi gas

$$e_e = \frac{3}{4} Y_e \hbar c (3\pi^2 n_e)^{1/3}; \tag{2.16}$$

- neutron gas outside nuclei

$$\begin{aligned} e_o = (1-u)\Bigg[& \frac{3}{10}\frac{\hbar^2}{m}(3\pi^2)^{2/3} {n_o}^{2/3} + \frac{1}{4} t_0 n_o (1-x_0) + \\ & + \frac{1}{24} t_3 {n_o}^{\phi+1} (1-x_3) + \\ & + \frac{3}{40}(3\pi^2)^{2/3} {n_o}^{5/3} [t_1(1-x_1) + 3t_2(1+x_2)] \Bigg]; \end{aligned} \tag{2.17}$$

- nucleons inside nuclei, both neutrons and protons

$$\begin{aligned} e_N = & u\Bigg[\frac{3}{10}\frac{\hbar^2}{m}\left(\frac{3\pi^2}{2}\right)^{2/3} {n_i}^{2/3} F_{5/3} + \frac{1}{8} t_0 n_i [2(x_0+2) - F_2(2x_0+1)] + \\ & + \frac{1}{48} t_3 {n_i}^{\kappa+1} [2(x_3+2) - F_2(2x_3+1)] + \\ & + \frac{3}{40}\left(\frac{3\pi^2}{2}\right)^{2/3} {n_i}^{5/3} \Big\{ F_{5/3}[t_1(x_1+2) + t_2(x_2+2)] + \\ & + \frac{F_{8/3}}{2}[t_2(2x_2+1) - t_1(2x_1+1)] \Big\} \Bigg] + \\ & + u\left[\frac{3}{r_N n_i}\sigma(Y_i) + \frac{4\pi}{5} e^2 {Y_i}^2 {r_N}^2 n_i D(u) \right], \end{aligned} \tag{2.18}$$

$$F_m(Y_i) = 2^{m-1}[Y_i^m + (1-Y_i)^m].$$

We give as the input of the algorithm the variable n. This choice allows us to study the range of typical densities of the inner crust, from $\approx 10^4$ fm^{-3}, close to the neutron drip density, till around half the value of the saturation density, ~ 0.08 fm^{-3}.

Other necessary inputs in our framework are the Skyrme parameters t_0, t_1, t_2, t_3, x_0, x_1, x_2, x_3, κ. We often discuss the role of n_∞, e_∞, K_∞, J, L, m^*, S_s, σ_s and we use some of them to calculate the approximate value of the surface tension σ as we discuss in subsection 2.1.3. Throughout the use of the algorithm we find the values of the quantities n_e, n_o, n_i, u, Y_e, Y_i, r_N. Some of them can be calculated analytically by setting few physical conditions which allow us to reduce the number of equations to solve numerically.

The conditions are:

- neutrality of charge: $nY_e = un_iY_i = n_e$
- conservation of the barionic number: $n = un_i + (1-u)n_o$
- nuclear "virial theorem": $e_s = 2e_C$.

The latter is the result from the minimization of the total energy as a function of the nuclear radius $\frac{\partial e}{\partial r_N} = 0$. It can be seen that this derivative is analytic and the solution may be written in terms of surface and Coulomb energy (*21*, *24*, *38*, *40*).

The previous conditions are used to fix the following relations:

$$nY_e = n_e \tag{2.19}$$

$$u = \frac{nY_e}{n_iY_i} \tag{2.20}$$

$$r_N = \left(\frac{15\sigma}{8\pi q^2 Y_i^2 n_i^2 D}\right)^{1/3} \tag{2.21}$$

$$n_o = \frac{n - un_i}{1-u}. \tag{2.22}$$

We gather analytically from the above conditions the expressions for the variables n_e, n_o, u, r_N, whereas the value of n_i, Y_e, Y_i have to be sought numerically. We need to impose some further conditions due to the nature of the system under study:

1. equality of pressure between inside nuclei and outside the neutron gas: $P_i = P_o$
2. minimization of the energy with respect to Y_i: $\dfrac{\partial e}{\partial Y_i} = 0$
3. condition of β equilibrium: $\mu_e = \mu_n - \mu_p + \Delta$

where μ indicates the chemical potential.

1. The pressure for a generic species with density n, internal energy E included in the volume V is defined as

$$P = -\frac{\partial E}{\partial V}\bigg|_A = n^2 \frac{\partial e}{\partial n}\bigg|_A . \tag{2.23}$$

In our model the two populations, neutron gas and nuclear matter, occupy different fractions of the total volume given by the WS cell. Following the idea to obtain equilibrium, we impose the two pressures to be equal. We write

$$P_o = {n_o}^2 \frac{\partial e_o/(1-u)}{\partial n_o} \tag{2.24}$$

$$P_i = {n_i}^2 \frac{\partial e_N/u}{\partial n_i} \tag{2.25}$$

so

$$P_i - P_o = 0$$

to guarantee the mechanical equilibrium. In equations (2.24) and (2.25) we must divide the energies per particle by the volume fraction as a consequence of our definitions of e_o and e_N.

2. The second equation is the derivative of the total energy with respect to the composition. Because of the electron gas energy does not depend on the variable Y_i, we derive only the terms e_o, e_N with respect to Y_i. We obtain

$$\frac{\partial e_o}{\partial Y_i}\bigg|_{n,Y_e,n_i} + \frac{\partial e_N}{\partial Y_i}\bigg|_{n,Y_e,n_i} = 0.$$

3. For the condition of β equilibrium, we can first evaluate the values for the chemical potential of the different contributions of our system:

$$\mu_e = \frac{3}{4}\hbar c (3\pi^2 n_e)^{1/3} \tag{2.26}$$

$$\mu_n = \frac{\partial \epsilon}{\partial n} - \frac{Y_e}{n}\frac{\partial \epsilon}{\partial Y_e} \tag{2.27}$$

$$\mu_p = \frac{\partial \epsilon/n}{\partial Y_e} + \mu_n - \mu_e. \tag{2.28}$$

During a β^- decay, a neutron decays forming a couple proton-electron and an antineutrino, while for a β^+ decay a proton is converted into a neutron and

a positron, plus a neutrino. When the reactions reach the equilibrium, the number of β^- decays equals to the number of β^+ decays. Having chemical equilibrium, we must impose $\mu_n^i = \mu_n^o$, the neutron chemical potential inside nuclei must be equal to the chemical potential of neutrons outside nuclei. The β equilibrium is given by the relation

$$\begin{aligned} \beta = 0 &= \mu_e - \mu_n + \mu_p - \Delta \\ &= \frac{\partial \epsilon / n}{\partial Y_e} - \Delta. \end{aligned} \tag{2.29}$$

Finally, we need to search the roots of the following system of equations

$$\begin{cases} {n_i}^2 \dfrac{\partial e_N / u}{\partial n_i} - {n_o}^2 \dfrac{\partial e_o / (1-u)}{\partial n_o} = 0 \\ \dfrac{\partial e_o}{\partial Y_i} + \dfrac{\partial e_N}{\partial Y_i} = 0 \\ \dfrac{\partial \epsilon / n}{\partial Y_e} - \Delta = 0. \end{cases} \tag{2.30}$$

Chapter 3

Vibrational modes in the inner crust

In the present chapter we introduce the vibrational collective modes of the inner crust of neutron stars, in particular we focus on the calculation of the dispersion relations of long-wavelength collective modes, which are a superposition of lattice vibrations and sound waves in the neutron superfluid. We use the approximation that the wave lengths are much larger than the scale of the variations of the different physical quantities in our system.

We derive the equations of motion using an approximation in which the scale of spatial variations is larger compared with the lattice spacing and the superfluid coherence length (*29*). The lattice spacing defines the size of the unit cell of a crystal lattice. For a bcc lattice its value is $a = 4r_C/\sqrt{3}$ (*56*): typical values for the inner crust are $a \sim 120 - 70$ fm for the density range $n \sim 10^{-4} - 0.08$ fm^{-3} and $a \sim 30$ fm at the saturation density (in (*24*) are listed some values of a in function of the density n). The coherence length ξ indicates the size of neutron pair wave function, i.e. the mean square distance of a Cooper pair of neutrons on top of the Fermi surface, $\xi \sim \hbar v_{Fn}/\Delta_n$, where v_{Fn} is the neutron Fermi velocity and Δ_n is the neutron superfluid energy gap. Even if there is no consensus on the exact value of the energy gaps in the inner crust, the common agreement is that they are of the order of 1 MeV (*2*). The values of neutron Fermi velocity calculated for the inner crust are $\sim 0.03c - 0.28c$ for $n \sim 10^{-4} - 0.08$ fm^{-3}, giving $\xi \sim 6 - 55$ fm while for the saturation density we have $v_{Fn} \sim 0.35c$ and $\xi \sim 70$ fm. As described in (*57*), the coherent length may be compared to the nuclear radius in a wide range of densities of the inner crust.

We decide to make a convenient choice considering an isotropic medium so the variables of interest do not depend on the specific position we consider (*58*). We shall neglect the effects of the gravitational potential: since its variations

are small over the crust, we can consider the space as flat (*29*).

We consider a system in thermodynamic equilibrium and then introduce a small displacement from the equilibrium position of the ions. This generates a sound wave in the neutron superfluid, a small deviation in the thermodynamic quantities that forces the system to oscillate, and lattice vibrations (*29*, *59*). The idea of considering the inner crust as an elastic medium is based on the approximation we made about the structure of that matter. The ions are supposed to be fixed in an equilibrium state forming a perfect crystal, specifically a bcc lattice which contains only one type of nuclide. We have to consider also entrained neutrons because they have a coherent dynamic with the ions, playing an important role in determining the dispersion relations of the modes (*11*) and the dynamic of the classical constituent (*32*, *43*), while superfluid neutrons are described independently from nuclei. Entrained neutrons may be coupled since they present the typical gap energy of a superfluid gas, but macroscopically this behaviour is neglected because the interaction with the nuclei is stronger and they are effectively bound to nuclei.

We now introduce the variables we use. During the study of the vibrational modes, it is more meaningful to refer as protons and neutrons separately because they behave differently under Coulomb potential. Our model establishes that all the protons are bounded by the nuclear potential inside the nuclei (n_i^p), while the neutrons are present both inside the nuclei (n_i^n) and outside the nuclei (n_o^n). They can be combined as follows

$$\begin{aligned} n_p &= u n_i^p \\ n_n^b &= u n_i^n + \alpha(1-u) n_o^n \\ n_n^s &= (1-\alpha)(1-u) n_o^n \end{aligned} \tag{3.1}$$

so

$$n = n_p + n_n^b + n_n^s + n_e. \tag{3.2}$$

The term n_n^s indicates the neutron superfluid component and n_n^b indicates the fraction of bounded neutrons, which are both present in nuclei and dripped by nuclei but still filling the nuclear potential. We neglect the presence of electrons, $n_e = 0$, because of their inertia (*47*), in fact $\frac{m_e}{m} \ll 1$ (compared to nucleons masses), so the dynamic of leptons can be studied separately from the dynamic of baryon. The parameter α indicates the fraction of entrained neutrons. We do not estimate the value of this parameter because we have not considered the band structure effects in our model, but we can give it a value as an input. In other works like (*46*) for example, it is explicitly calculated. Reasonable values of α can be obtained from (*30*, *60*) and they are discussed in section 5.4 during a more detailed entrainment analysis and in chapter 6 together with an application of the velocities in the heat capacity calculations.

We choose to use the total number density of neutrons $n_n = n_n^s + n_n^b$ and the number density of protons n_p as variables of our model because these quantities enter in the conservation law for particles number. Then we consider, as further variables, the velocities of the species, because we are interested in describing the motion of the constituents. We indicate $\mathbf{u}(\mathbf{r})$ as the small displacement from the equilibrium position, such as the velocity of the ions (protons and neutrons inside the nuclei) can be defined as $\mathbf{v}_p = \dot{\mathbf{u}}$. For superfluid neutrons we have $\mathbf{v}_n = \frac{\hbar}{m}\mathbf{k}$ (*29*, *47*), where $\mathbf{k}$ is the wave vector and m indicates the bare nucleon mass, without any difference between protons and neutrons (*29*, *46*).

3.1 Hydrodynamic equations

In the present work, based on the model of (*29*), hydrodynamic equations are simply derived from local conservation laws of the number of baryons (resulting in the continuity equations for protons and neutrons densities) and the momentum (giving the Euler equation). We are also considering the properties of the superfluid separately, which leads to an additional equation of motion that can be referred to as the Josephson relation (*29*, *47*).

Considering a spatially homogeneous equilibrium state, we introduce small perturbations, whose length scale is smaller than electron screening length. In this case, the matter is locally electrically neutral, so the total number density of electrons must be equal to the number density of protons (*29*). The continuity equation for protons is

$$\frac{\partial n_p}{\partial t} + n_p \nabla \cdot \mathbf{v}_p = 0 \tag{3.3}$$

which is linearized for small deviations of the system from the equilibrium condition. The continuity equation for neutrons is

$$\frac{\partial n_n}{\partial t} + n_n^s \nabla \cdot \mathbf{v}_n + n_n^b \nabla \cdot \mathbf{v}_p = 0 \tag{3.4}$$

also linearized. The densities n_p and n_n are constant for a spatial variation.

We suppose that our system is not affected by dissipative phenomena. So the momentum conservation equation appears in the form

$$\frac{\partial \mathbf{g}}{\partial t} = \mathbf{f}$$

where $\mathbf{g}$ indicates the momentum density and $\mathbf{f}$ the force per unit volume. First we consider a decoupled system, simply composed by a neutron fluid

and a proton fluid (we neglect the effects due to the lattice); so $\mathbf{f} = -\nabla P$ where P indicates the pressure. At the temperature $T = 0$ K the variation of the pressure is only related to the variation of the chemical potentials of the different species as indicated by Gibbs-Duhem law, so in our case

$$dP = n_n d\mu_n + n_p d\mu_p.$$

For the momentum density we have

$$\mathbf{g} = m n_n^s \mathbf{v}_n + m(n_p + n_n^b)\mathbf{v}_p.$$

Using the expressions of $\mathbf{g}$ and $\mathbf{f}$, the momentum conservation equation is expressed in the form

$$m n_n^s \frac{\partial \mathbf{v}_n}{\partial t} + m(n_p + n_n^b)\frac{\partial \mathbf{v}_p}{\partial t} + n_n \nabla \mu_n + n_p \nabla \mu_p = 0. \tag{3.5}$$

We now have to consider the existence of the lattice made by the protons, so we modify the term $n_p \nabla \mu_p$ taking into account the elastic effects of the lattice and the coupling effects with the neutrons.

For an isotropic solid we introduce the strain tensor

$$u_{ij} = \frac{1}{2}\left(\frac{\partial u_i}{\partial x_j} + \frac{\partial u_j}{\partial x_i}\right), \tag{3.6}$$

where the indexes run for the Cartesian coordinates $i, j = x, y, z$ and whose trace is related to the density by the following relation

$$u_{ii} = -\frac{\delta n_p}{n_p}. \tag{3.7}$$

It is known that it is possible to express the free energy F in a completely general way as a function of the strain tensor (*61*)

$$F = F_0 + \frac{1}{2}\lambda {u_{ii}}^2 + \mu {u_{ij}}^2 \tag{3.8}$$

given by the sum of a uniform term and terms that are quadratic into the infinitesimal displacement. The quantities λ and μ are called Lamè coefficients. Since any deformation of a generic body can be represented by the sum of a pure shear and a hydrostatic compression (*61*), we can rewrite (3.6) as

$$u_{ij} = \left(u_{ij} - \frac{1}{3}\delta_{ij} u_{kk}\right) + \frac{1}{3}\delta_{ij} u_{kk}.$$

A pure shear (first term) is a deformation in which the volume remains constant while the shape is altered. A hydrostatic compression (second term) is a deformation in which the volume is changed while there are no changes in its shape. Using the last definition of tensor u_{ij} we obtain the expression for elastic energy

$$F_{el} = \frac{1}{2}\tilde{K}{u_{kk}}^2 + S\left(u_{ij} - \frac{1}{3}\delta_{ij}u_{kk}\right)^2 \tag{3.9}$$

where $\tilde{K} = \lambda + \frac{2}{3}\mu$ is the *bulk modulus*, and $S = \mu$ is the *shear modulus*. The first term, multiplied by the diagonal elements of the strain tensor, indicates the compression, acting in perpendicular way respect to the faces of bcc lattice; the second term, which contains also the non diagonal elements of the tensor, refers to phenomena of non-perpendicular compression and stretch through the different sections.

The definition of the shear modulus is given by the relation

$$S = 0.1194\,\frac{3}{4\pi}\frac{Z^2q^2}{{r_C}^4} \tag{3.10}$$

(see section 3.4 for a more detailed description).

For a solid consisting of a single component, $\tilde{K}$ corresponds to the total bulk modulus; for our model, $\tilde{K}$ indicates the contribution to the bulk modulus when n_n is fixed. So we can define $\tilde{K}$ using the total bulk modulus (or incompressibility) $K = -V\partial P/\partial V$ (V is the volume of the system), where the derivative is evaluated for a fixed number of protons and neutrons. We have

$$K = n_p^2\,\frac{\partial\mu_p}{\partial n_p} + 2n_n n_p\,\frac{\partial\mu_n}{\partial n_p} + n_n^2\,\frac{\partial\mu_n}{\partial n_n} \tag{3.11}$$

whose terms are expressed by quantities such as $\frac{\partial\mu_\alpha}{\partial n_\beta}$, with $\alpha, \beta = n, p$. They correspond to the second derivative of the energy density ϵ and represent the residual interaction between neutrons and protons. We rewrite (3.11) as

$$K = \tilde{K} + 2n_n\tilde{L} + {n_n}^2 E_{nn} \tag{3.12}$$

using the coefficients which are defined as follows

$$\begin{aligned} \frac{\partial\mu_n}{\partial n_n} &= \frac{\partial^2\epsilon}{\partial n_n^2} = E_{nn} \\ \frac{\partial\mu_n}{\partial n_p} &= \frac{\partial^2\epsilon}{\partial n_n \partial n_p} = E_{np} = \frac{\tilde{L}}{n_p} \\ \frac{\partial\mu_p}{\partial n_p} &= \frac{\partial^2\epsilon}{\partial {n_p}^2} = E_{pp} = \frac{\tilde{K}}{n_p^2}. \end{aligned} \tag{3.13}$$

The effective n-n, n-p and p-p interactions are indicated respectively as E_{nn}, E_{np}, E_{pp}.

For the interaction energy between the lattice (protons) and neutrons we have

$$F_{l,n} = -\tilde{L}\delta n_n u_{ii} \tag{3.14}$$

which is bilinear into displacement and density variation (for a further discussion, see section 3.4).

Given the terms of elastic energy (3.9) and interaction energy (3.14), we can obtain the force for unit volume $f_{el} + f_{l,n}$ using the stress tensor σ_{ik} instead of calculating directly the gradient of energy (see (*61*) §2). We calculate

$$\sigma_{ik} = \left.\frac{\partial F_{el} + Fl, n}{\partial u_{ik}}\right|_T = \tilde{K}u_{ll}\delta_{ik} + 2S\left(u_{ik} - \frac{1}{3}\delta_{ik}u_{ll}\right)\left(1 - \frac{1}{3}\delta_{ik}\right) - \tilde{L}\delta n_n \delta_{ik}$$

and then

$$f_{(el+l,n)i} = \frac{\partial \sigma_{ik}}{\partial x_k} = \tilde{K}\nabla_i u_{ll} + 2S\nabla_i\left(u_{ik} - \frac{1}{3}\delta_{ik}u_{ll}\right) - \tilde{L}\nabla_i n_n.$$

The total force $\mathbf{f}$, made by the fluid term and the corrections of elasticity and interaction, is

$$\mathbf{f} = n_n\,\nabla\mu_n + \tilde{K}\nabla u_{ll} + 2S\nabla\left(u_{ik} - \frac{1}{3}\delta_{ik}u_{ll}\right) - \tilde{L}\nabla n_n. \tag{3.15}$$

We also have to consider the contribution of the superfluid. The hydrodynamic of a superfluid is often described within a so-called two-fluid model (well described in (*59*, *62*)). It is a macroscopical description: in the two-fluid picture, the superfluid system is formally divided into two components, the superfluid flow and normal flow, which interpenetrate each other. The superfluid component consists of the condensate, while the normal component contains the elementary excitations and its importance increases with the temperature (because it causes collective thermal motions). At zero temperature there is only the superfluid flow. Within the approximations we are considering, we use

$$\frac{\partial \mathbf{v}_n}{\partial t} + \frac{\nabla\mu_n}{m} = 0 \tag{3.16}$$

as in (*59*) to describe the motion of the superfluid neutron gas. We now briefly explain how to obtain the Josephson equation, that sets the temporal variation of phase ϕ of a superfluid with the associated chemical potential

$$\frac{\partial\phi}{\partial t} = -\frac{\mu_n}{\hbar}. \tag{3.17}$$

The superfluid can be considered like a macroscopic object which moves in space without friction and without any variation of its density. Macroscopically it is described by a complex quantity like $\Psi(\mathbf{r},t) = \Psi_0\, e^{\imath\phi(\mathbf{r},t)}$. The general phase may be written as $\phi(\mathbf{r},t) = \mathbf{k}\cdot\mathbf{r} - \omega t$ in which ω indicates the frequency and $\mathbf{k}$ indicates the wave vector. It is interesting to compare the variation of the current density $\mathbf{j}$ with the global equation of the motion (3.16) for the superfluid itself. We know that $\mathbf{j}_n = n_n^s v_n$, but furthermore we can also write the current density in terms of $\Psi, \Psi^\dagger$ as $\mathbf{j}_n = \Psi^\dagger\nabla\Psi + \Psi\nabla\Psi^\dagger \sim |\Psi|^2\,\nabla\phi$. Since $|\Psi|^2 = n_n^s$, the density does not vary during the motion of the superfluid. As a consequence, the macroscopic velocity is due to a variation of the phase, $\mathbf{v}_n = \frac{\hbar}{m}\nabla\phi$. This also explains where does the definition of superfluid velocity comes from: $\nabla\phi = \mathbf{k}$ in approximation of coarse-grained average phase (*29*, *47*), which means to consider the average of ϕ over a region in the vicinity of $\mathbf{r}$. Finally, substituting $\mathbf{v}_n$ with $\nabla\phi$ into the equation of motion (3.16) leads to the Josephson equation (3.17).

Using (3.15) and (3.16), we rewrite (3.5) as follows

$$m\left(n_p + n_n^b\right)\frac{\partial \mathbf{v}_p}{\partial t} + n_n^b\nabla\mu_n - \tilde{K}\nabla u_{ll} - 2S\nabla\left(u_{ik} - \frac{1}{3}\delta_{ik}u_{ll}\right) + \tilde{L}\nabla n_n = 0. \quad (3.18)$$

The chemical potential of neutrons may be expressed as an expansion of its terms

$$d\mu_n = \frac{\partial\mu_n}{\partial n_n}dn_n + \frac{\partial\mu_n}{\partial n_p}dn_p. \quad (3.19)$$

From equation (3.13), we have

$$d\mu_n = E_{nn}dn_n - \tilde{L}du_{ii}. \quad (3.20)$$

We obtain the final form for equation (3.18), using (3.20) and writing explicitly the terms $\nabla\cdot\mathbf{u}$ and $\nabla\times\mathbf{u}$:

$$\begin{aligned} &m\left(n_p + n_n^b\right)\frac{\partial \mathbf{v}_p}{\partial t} + n_n^b\left(E_{nn}\nabla n_n - \tilde{L}\nabla(\nabla\cdot\mathbf{u})\right) + \\ &- \tilde{K}\nabla(\nabla\cdot\mathbf{u}) - \frac{4}{3}S\nabla(\nabla\cdot\mathbf{u}) + S\nabla\times(\nabla\times\mathbf{u}) + \tilde{L}\nabla n_n = 0. \end{aligned} \quad (3.21)$$

3.2 Collective modes

We assume that the physical quantities used in the present work exhibit a space and time dependence as $e^{i(\mathbf{k}\cdot\mathbf{x} - wt)}$, typical of a plane wave. We can write the general physical variable as a sum of a uniform term and a infinitesimal variation, $a = a_o + \delta a$; $\delta a \ll a_0$.

Because of our hypothesis concerning an isotropic medium, the longitudinal and the transverse modes are decoupled (*29*, *46*, *47*). This is important because we can study them separately. Moreover, at long wavelengths the normal modes all have a sound-like dispersion relation $\omega = vk$, where v is the velocity of the mode.

3.2.1 Transverse modes

The transverse modes are defined by $\nabla \cdot \mathbf{u} = 0$. Furthermore, $\nabla n_n = 0$ for two different reasons. The first one is related to superfluids; it is known that superfluids do not react to cross forces. For a transversal wave, the variation of n_n occurs transversally respect to the direction of propagation of the wave itself. This effect is caused by the action of a shear force on the matter. The second reason is related to the approximation of long wavelengths.

Equation (3.21) is simplified in the form

$$m\left(n_p + n_n^b\right)\frac{\partial \mathbf{v}_p}{\partial t} + S\,\nabla \times (\nabla \times \mathbf{u}) = 0;$$

remembering by definition $\mathbf{v}_p = \dot{\mathbf{u}}$, we obtain a wave equation

$$\nabla^2 u - \frac{m\left(n_p + n_n^b\right)}{S}\frac{\partial^2 u}{\partial t^2} = 0$$

where the wave velocities are given by

$$v_t{}^2 = \frac{S}{m\left(n_p + n_n^b\right)}. \tag{3.22}$$

We notice how this velocity is identified only by the shear term of elastic energy (for this reason they are also called shear modes) and how $\rho^b = m\left(n_p + n_n^b\right)$ contains non superfluid terms (as told before, they are not conditioned by transversal waves). The continuity equations for protons and neutrons give the conditions $\partial_t n_p = 0$, $\partial_t n_n = 0$, so densities are uniform both spatially and temporally (*47*).

3.2.2 Longitudinal modes

The longitudinal modes are defined by $\nabla \times \mathbf{u} = 0$. Since the physical quantities are given by the sum of a uniform term and a infinitesimal variation, we linearize equations (3.4), (3.3), (3.16) and (3.21) for longitudinal modes. Using the dispersion relation $v = \dfrac{w}{k}$ we can write the set of equations

$$\begin{cases} v\delta n_p - n_p v_p = 0 \\ v\delta n_n - n_n^s v_n - n_n^b v_p = 0 \\ v\, v_n - \delta n_n \dfrac{E_{nn}}{m} - \dfrac{\delta n_p}{n_p}\dfrac{L}{m} = 0 \\ mv\left(n_p + n_n^b\right) v_p - \delta n_n \left(n_n^b E_{nn} + L\right) - \dfrac{\delta n_p}{n_p}\left(\tilde{K} + \dfrac{4}{3}S + n_n^b L\right) = 0. \end{cases}$$

The most interesting variables are δn_n, δn_p, v_p, v_n. From continuity equations we find out the following expressions for the variation of densities

$$\delta n_p = n_p \frac{v_p}{v}$$

$$\delta n_n = \frac{n_n^s v_n + n_n^b v_p}{v}$$

which allow us to simplify the set of equations from four to two equations. Using as reference (3.13), we change notation preferring $E_{\alpha\beta}$, because shows in a more directly way which interacting energies are relevant. We call $\rho^s = m n_n^s$ and rewrite the new set of equations as

$$\begin{cases} \big(\rho^s v^2 - \overbrace{E_{nn}(n_n^s)^2}^{\epsilon^{ss}}\big) v_n - \big(\overbrace{E_{nn} n_n^s n_n^b + E_{np} n_p n_n^s}^{\epsilon^{bs}}\big) v_p = 0 \\ \big(\rho^b v^2 \underbrace{- E_{nn}(n_n^b)^2 - 2E_{np} n_p n_n^b - E_{pp} {n_p}^2}_{-\epsilon^{bb}} - \dfrac{4}{3} S\big) v_p + \\ \qquad + \big(\underbrace{E_{nn} n_n^b n_n^s + E_{np} n_p n_n^s}_{\epsilon^{bs}}\big) v_n = 0. \end{cases} \tag{3.23}$$

For convenience, we choose to divide the different kinds of energy, whom are related to superfluid component ϵ^{ss}, to normal component ϵ^{bb} and to mixed terms ϵ^{bs}. We solve the set of equations calculating the determinant of coefficients matrix to obtain the relation of dispersion for the velocities

$$\begin{pmatrix} \rho^s v^2 - \epsilon^{ss} & -\epsilon^{bs} \\ -\epsilon^{bs} & \rho^b v^2 - \epsilon^{bb} - \frac{4}{3} S \end{pmatrix} \begin{pmatrix} v_n \\ v_p \end{pmatrix} = 0.$$

Calculating the determinant of the previous matrix as equal to zero, we obtain

$$\left(v^2 - \frac{\epsilon^{ss}}{\rho^s}\right)\left(v^2 - \frac{\epsilon^{bb} + \frac{4}{3} S}{\rho^b}\right) = \frac{(\epsilon^{bs})^2}{\rho^s \rho^b}$$

and in a simpler form

$$(v^2 - v_n^2)(v^2 - v_p^2) = v_{np}^4. \tag{3.24}$$

It is now possible to extract two decoupled modes, one for the superfluid component and one for the lattice, and two coupled modes.

For the decoupled modes $v_{np} = 0$. We suppose the lattice to be stationary, $v_p = 0$; we gain

$$v_n^2 = \frac{\epsilon^{ss}}{\rho^s} \tag{3.25}$$

which is the velocity of a superfluid Bogoliubov-Anderson boson: this mode corresponds to an acoustic wave of neutron superfluid (Bogoliubov-Anderson mode). Equaling the superfluid velocity to zero, $v_n = 0$, we have

$$v_p^2 = \frac{\epsilon^{bb} + 4S/3}{\rho^b} \tag{3.26}$$

which indicates the velocity of a lattice phonon: this mode corresponds to an acoustic wave of lattice, i.e. an oscillation.

For the coupled modes, we have to solve the equation (3.24) where

$$v_{np}^2 = \frac{\epsilon^{bs}}{\sqrt{\rho^s \rho^b}} \tag{3.27}$$

and the solutions are

$$v_\pm^2 = \frac{v_p^2 + v_n^2}{2} \pm \sqrt{\left(\frac{v_p^2 + v_n^2}{2}\right)^2 + v_{np}^4 - v_p^2\, v_n^2}. \tag{3.28}$$

3.3 $E_{\alpha\beta}$ coefficients

After the discussion about the velocities, we need to calculate the values of E_{nn}, E_{np}, E_{pp}. The term $E_{\alpha\beta}$ indicates the derivative of the energy density as a function of the proton and neutron density as in (3.13).

A change of variables is required. Starting from (3.1), after some algebra we can express the derivatives of the energy density in function of variables n, Y_e (using the results gained in previous chapters) instead of n_n, n_p. We obtain that the two sets of quantities are related by the transformation

$$\begin{pmatrix} \dfrac{\partial^2\epsilon}{\partial {n_n}^2} \\ \dfrac{\partial^2\epsilon}{\partial n_n \partial n_p} \\ \dfrac{\partial^2\epsilon}{\partial {n_p}^2} \end{pmatrix} = \begin{pmatrix} 1 & -2Y_e & Y_e^2 \\ 1 & 1-2Y_e & -Y_e(1-Y_e) \\ 1 & 2(1-Y_e) & (1-Y_e)^2 \end{pmatrix} \begin{pmatrix} \dfrac{\partial^2\epsilon}{\partial n^2} \\ \dfrac{1}{n}\dfrac{\partial^2\epsilon}{\partial n \partial Y_e} \\ \dfrac{1}{n^2}\dfrac{\partial^2\epsilon}{\partial {Y_e}^2} \end{pmatrix} \tag{3.29}$$

which represents the change of the variables n, $Y_e \to n_p$, n_n. If we write this condition as a system of equations, we have

$$\begin{cases} E_{nn} = \dfrac{\partial^2\epsilon}{\partial n^2} - \dfrac{2Y_e}{n}\dfrac{\partial^2\epsilon}{\partial n \partial Y_e} + \dfrac{Y_e^2}{n^2}\dfrac{\partial^2\epsilon}{\partial {Y_e}^2} \\ E_{np} = \dfrac{\partial^2\epsilon}{\partial n^2} + \dfrac{1-2Y_e}{n}\dfrac{\partial^2\epsilon}{\partial n \partial Y_e} - \dfrac{Y_e(1-Y_e)}{n^2}\dfrac{\partial^2\epsilon}{\partial {Y_e}^2} \\ E_{pp} = \dfrac{\partial^2\epsilon}{\partial n^2} + \dfrac{2(1-Y_e)}{n}\dfrac{\partial^2\epsilon}{\partial n \partial Y_e} + \dfrac{(1-Y_e)^2}{n^2}\dfrac{\partial^2\epsilon}{\partial {Y_e}^2}. \end{cases} \tag{3.30}$$

The results submitted in (3.30) are also exposed in (*47*).

We require second derivatives of density energy even for our starting variables n, Y_e. We consider the equations (2.29) and (2.23), representing the β equilibrium and the expression of the total pressure P inside the cell. We derive them again as a function of n, Y_e, obtaining

$$\begin{aligned} \frac{\partial\beta}{\partial Y_e} &= \frac{\partial^2 e}{\partial {Y_e}^2} \\ \frac{\partial P}{\partial n} &= n^2\frac{\partial^2 e}{\partial n^2} + 2n\frac{\partial e}{\partial n} \\ \frac{\partial P}{\partial Y_e} &= n^2\frac{\partial^2 e}{\partial n \partial Y_e}. \end{aligned} \tag{3.31}$$

Passing from the initial set of derivatives to the required, needs little mathematical handling and substitution of variables.

We can obtain the following relations among the variables

$$\begin{aligned} \frac{\partial^2\epsilon}{\partial {Y_e}^2} &= n\frac{\partial^2 e}{\partial {Y_e}^2} = n\frac{\partial\beta}{\partial Y_e} \\ \frac{\partial^2\epsilon}{\partial n^2} &= n\frac{\partial^2 e}{\partial n^2} + 2\frac{\partial e}{\partial n} = \frac{1}{n}\frac{\partial P}{\partial n} \\ \frac{\partial^2\epsilon}{\partial n \partial Y_e} &= n\frac{\partial^2 e}{\partial n \partial Y_e} + \frac{\partial e}{\partial Y_e} = \frac{1}{n}\left(\frac{\partial P}{\partial Y_e} + n\frac{\partial e}{\partial Y_e}\right). \end{aligned} \tag{3.32}$$

Replacing the derivatives using (3.1) and (3.31) to highlight the parameters $E_{\alpha\beta}$ and rewriting the (3.29) explicitly as a system of equations, we obtain

$$\begin{cases} E_{nn} = \dfrac{1}{n}\dfrac{\partial P}{\partial n} - \dfrac{2Y_e}{n^2}\left(\dfrac{\partial P}{\partial Y_e} + n\dfrac{\partial e}{\partial Y_e}\right) + \dfrac{Y_e^2}{n}\dfrac{\partial \beta}{\partial Y_e} \\ E_{np} = \dfrac{1}{n}\dfrac{\partial P}{\partial n} + \dfrac{1-2Y_e}{n^2}\left(\dfrac{\partial P}{\partial Y_e} + n\dfrac{\partial e}{\partial Y_e}\right) - \dfrac{Y_e(1-Y_e)}{n}\dfrac{\partial \beta}{\partial Y_e} \\ E_{pp} = \dfrac{1}{n}\dfrac{\partial P}{\partial n} + \dfrac{2(1-Y_e)}{n^2}\left(\dfrac{\partial P}{\partial Y_e} + n\dfrac{\partial e}{\partial Y_e}\right) + \dfrac{(1-Y_e)^2}{n}\dfrac{\partial \beta}{\partial Y_e}. \end{cases} \tag{3.33}$$

3.4 Shear modulus

We briefly describe the shear elastic constant. The basic idea behind the definition of the shear modulus (or shear elastic constant) is how a lattice reacts under a non-uniform compression. We consider a unit volume of a generic body, and suppose to compress this volume. We impose to not vary the volume. The compression causes for instance the reduction of one or more of its dimensions, and the other dimensions should increase to compensate the loss (for example, if we compress a cube along the x axis, keeping the volume constant, we expect that the cube extends along the y, z axis). What it is interesting to study then is how the ions in the bcc lattice react to the change of reciprocal distances, i.e. how the cohesive energies vary. To do so, we follow the discussion in (*63*).

In solid state theory, the energies among charged particles are defined as cohesive energies. The cohesive energies are given by the potential energies of classical particles localized at the equilibrium positions into the lattice structure. Because the particles we are considering are ions (electrically charged particles), by far the most relevant contribution in the interaction energy is the Coulomb energy between ions.

The calculation of this kind of interaction hides a particular difficulty. First of all, the Coulomb potential is proportional to the inverse of the distance. Secondly, the Coulomb interaction is a long range interaction. So, when we approach to infinite matter, the calculation of cohesive energy can not converge to a finite result. The solution found to elude this mathematical and physical problem is to define a unit volume in which calculate the cohesive forces, and in particular the Coulomb term, the most problematic one. The choice of the unit volume is not accidental: it must be globally neutrally charged and without unpaired charges at the surface of the volume itself. It has been calculated that it is sufficient to divide the lattice in an appropriate structure (depending on

the type of lattice), to avoid the presence of surface charges. In this way, it is possible to evaluate the Coulomb contribution into a finite volume; then, it is sufficient to calculate an infinite series of finite volumes to obtain the Coulomb term of an infinite crystal. In practise, all the above theory can be summarized into the following steps: once defined the Coulomb term of cohesive energy, it can be calculated into a unit volume and then multiplied by specific parameters to reproduce the effect of the infinite matter. These parameters, depending on the type of lattice as told before, are constant values, well calculated and available in tables, are known as the Madelung constants.

The shear modulus is a useful parameter because it describes the possible displacement terms. The definition of the shear modulus is (*64*)

$$S = \mu_{eff} \frac{n(Zq)^2}{a} \tag{3.34}$$

where $n = \frac{N}{L^3}$ indicates the ion density (N is the total particles number and L^3 the volume of the cell used for the Monte Carlo simulation by (*64*)) and $\frac{a}{L} = \left(\frac{3}{4\pi N}\right)^{1/3}$. Rewriting this last definition, we notice that $\left(\frac{4\pi a^3}{3}\right)N = L^3$, so the volume of the sphere with radius a indicates the volume available for a single particle. In our model we do not have particles but cells: so the radius a must be equal to r_C, and the corresponding volume is identified by the volume of the WS cell. We can also consider, by definition, that the ion density is the volume occupied by the ion in a single cell, so $n \equiv n_N = {V_C}^{-1}$. The value of the constant μ_{eff}, known as the effective shear modulus, depends on the structure of the matter in analysis (crystals, quenched solids or fluids). For a bcc lattice at $T = 0$ K, they calculate the value of 0.1194 in $\frac{n(Ze)^2}{a}$ units (*63*, *64*). The same relation is reported in (*2*, *47*). Using the substitutions indicated above, we obtain the following expression for the shear modulus S

$$S = 0.1194 \frac{3}{4\pi} \frac{Z^2 q^2}{{r_C}^4}. \tag{3.35}$$

Moreover, it is possible to consider the contribution due to the inhomogeneity of electron distribution, i.e. the effect of electron screening, in the shear modulus as in (*47*). The effect due to the electron screening is to reduce the shear modulus about 10% for $Z = 40$ compared to the value calculated without this effect (*65*).

After these first chapters of theoretical description of the model, in the following part we discuss the outcomes we obtain, in particular the structure and the composition of our framework, the calculated velocities of the vibrational modes and an example of application of the results.

Chapter 4

Sensitivity of the results to the physical input

In this chapter we first make a comparative discussion between a selection of models existing in literature and our model. Then we focus on our framework and we describe the results obtained by means of a sensitivity analysis in which we vary the values of few parameters. In particular we choose different Skyrme forces that are associated with different physical parameters as shown in Table 4.1.

4.1 Comparative analysis

	n_∞	e_∞	K	m^*/m	J	L	a_s	S_s	r_o
SLy4	0.1595	15.97	230	0.695	32.00	45.96	19.94	55.33	1.1438
BSk14	0.1586	15.85	239	0.800	30.00	43.90	19.23	42.52	1.1461
SkM*	0.1603	15.77	217	0.789	30.03	45.78	19.32	50.59	1.1420
SAMi	0.1587	15.93	245	0.675	28.13	43.56	19.68	43.98	1.1458

Table 4.1: Values of parameters for the four Skyrme used. The dimensions are: n_∞ [fm^{-3}]; e_∞, K, L, a_s, S_s [MeV]; r_o [fm]; m^*/m [adimensional].

4.1.1 Density range motivations

Within our framework, for the following comparative analysis, we extend the number density n range for the inner crust from the neutron drip density

$\sim n_{drip}$ to the fraction of the saturation density $\sim 0.4 n_\infty$. The choice of these values is correlated with the limits of validity of the algorithm.

Firstly we want to understand if our model can be used to describe in a quite accurate way the ordinary matter that appears in the outer crust as well, i.e. the nuclei in the iron region. The main intent behind this idea is to obtain values of the quantities of interest regarding the transition between the outer crust and the inner crust to ensure continuity in the description of the whole crust. The Skyrme interactions used fit experimental nuclear masses typical of the outer crust and may be not so reliable for exotic nuclei (far from the neutron dip density). Our algorithm however can not reproduce the energy contributions of ordinary nuclei because of some numerical problems during the minimization in our algorithm. Any further analysis of the reasons causing the failure of the code is outside of the main purpose of this work, so we simply arrange the inferior limit density of our analysis at the neutron drip density n_{drip}.

For densities typical of the bottom layers of the inner crust, in the mantle region, we observe how the algorithm can not perform reliable calculations either. Since we assume that the shape of the nuclei is spherical, we expect some spurious effects concerning the formation of pasta phases around half the saturation density.

In order to set a reasonable limiting density in our framework which is consistent with the results known in literature, we make a comparison among various models. The appearance of other shapes, bubbles and the transition with the uniform matter is model dependent. A collection of transition density values, from nuclei surrounded by free neutrons to homogeneous nuclear matter, is indicated in (*41*) for several models. The work (*45*) finds that the edge of the crust has density ~ 0.075 fm^{-3}, where uniform *npe* matter begins to form. In (*66*) are shown how the favoured shape depends on the values of K, L and, in particular, spherical nuclei may be substituted by tubes in the range $0.058 - 0.064$ fm^{-3}. The formation of bubble is provided at $n = 0.08$ fm^{-3} by (*60*) (using data from (*67*)). The works (*19*, *37*, *68*) report an analysis of possible shapes, underlining which may be energetically preferred in function of the density. In (*37*) spherical nuclei are energetically favoured till $u \sim 0.25$, which means ~ 0.06 fm^{-3} compared to our values. For (*68*) the threshold is achieved at $n/n_\infty \sim 0.25$, which leads to ~ 0.04 fm^{-3} and finally for (*19*) the change from droplet to rod takes place at ~ 0.067 fm^{-3}. We have decided to set a common upper limit value for the density, since the maximum density values n accepted by the algorithm without producing any numerical error are similar for the four Skyrme parametrizations (maximum difference $\sim 10\%$). We take $n_{edge} = 0.4 n_\infty$; higher densities are shown in the following figures in

the shadowy region but the quantities calculated may not be reliable.

4.1.2 Models in literature

There are several works in literature concerning the description and the models used for the inner crust. We consider some of them making few comparative graphs to show any possible difference, in order to underline how many resources exist to describe the inner crust.

Even if the structure of the inner crust may be clear, nowadays we are far from having a unified description and an univocal EoS. Some models are based on the CLDM, some use the Skyrme parametrization and employ a microscopic Hartree-Fock interaction, others use the Thomas-Fermi approach.

Baym *et al.* (BBP) (*24*) are the first who have introduced the CLDM. This model is created to take into account the effect of dripped neutrons. They obtain a simple parametrization of the nuclear binding energy as function of density and proton fraction. For the calculations of the infinite nuclear matter they include only the two-body potential, while the higher-order terms and relativistic terms are considered as phenomenological corrections. The liquid drop model, quite similar to that described in (*24*, *40*), is also used by Steiner (S) (*41*). The liquid drop model for this work consists of a bulk energy contribution which is determined from the EoS of homogenous nucleonic matter together with surface and Coulomb contributions. In the Douchin & Haensel model (DH) (*45*) the inner crust is treated in the CLDM approach. They formulate a unified EoS for NS on the basis of the SLy4 Skyrme nuclear effective force (*50*), which also contains certain microscopic input.

In the paper of Chamel *et al.* (CPR) (*46*) the structure of the crust is described by a nonrelativistic Skyrme effective Hamiltonian, solved using the extended Thomas-Fermi method: this is the so-called ETFSI, a mean-field method in semi-classical apprioach. These calculations are carried out with the Skyrme force BSk14 and the ground-state composition of the inner crust is given by Onsi *et al.* (*67*). Kobyakov & Pethick (KP) (*47*) calculate the derivatives for thermodynamic quantities from the microscopic calculations of the properties of matter in the inner crust made by Lattime & Swesty (LS) (*38*).

The first quantal mean field approximation is presented by Negele & Vautherin (NV) (*39*). Other authors who treated this problem, such as Lorenz *et al.* (LPR) (*25*) use additional approximations of the quantum mean-field scheme (see also (*13*, *23*) and references therein). In particular they calculate the properties of matter using a CLDM and a microscopic interaction, obtained by fitting a Skyrme-like energy-density functional to their values, for the nuclear and neutron matter.

Sharma *et al.* (BCPM) (*19*) perform self-consistent Thomas-Fermi calculations with the BCPM (Barcelona-Catania-Paris-Madrid) nuclear energy density functional (*69*) in different shape configurations. The nuclear EoS of the model is consistent with the microscopic many-body Brueckner-Hartree-Fock approach.

4.1.3 The analysis

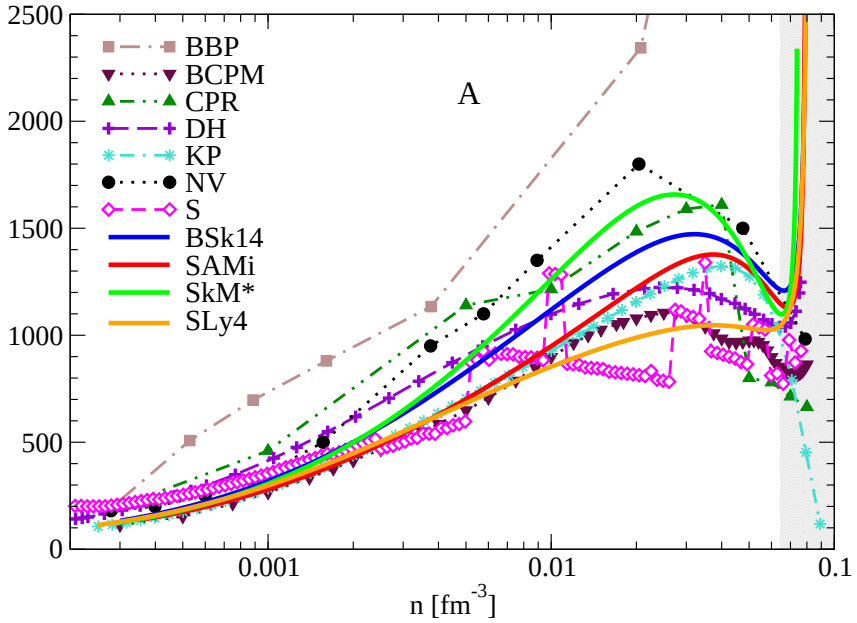

Figure 4.1: Total baryon number per cell A as a function of the baryon number density n.

As it is show in Figure 4.1, the value of A varies quite a lot: the range of allowed total baryon number can be compared with (*70*) in which a similar analysis is shown. Our parametrizations BSk14, SAMi, SkM*, SLy4 are well included in the range of possible values given by the works that we use as references. Excluding BBP, all the models present an increasing trend and then a decrease: they start from the neutron drip density with $100 - 200$ baryons and they have a peak, more or less accentuated, in the range of $0.02 - 0.04$ fm^{-3} counting from 1050 to 1800 baryons, with some oscillations of S from 770 to 1330. In the bottom layers of the inner crust, the global trend is a decrease of the baryon number with minimum values included in $660 - 1200$ for densities $0.05 - 0.08$ fm^{-3} and with an absolute minimum of ~ 110 given by KP. The high values reached by our parametrizations at ~ 0.075 fm^{-3} and beyond can be considered as unrelated errors maybe due to the impossibility of the EoS

used to describe uniform matter and pasta phases. The only exception is given by the BBP model, which shows a highly increasing value of baryons from 200 to 15000 in the density range of our interest. The number of total baryons has a strong dependence on the structure of the model used to describe the EoS and also depends on the choice of the parametrization. For example, we see how our four curves, even if obtained with the same algorithm and similar in trend, represent different systems, in which the maximum value of A varies from 1658 (SkM*) to 1046 (SLy4). In addition we notice in Figure 4.1 how CPR and BSk14 use the same Skyrme interaction, and how the results displayed in the graph are far from being close (same discussion for DH and SLy4).

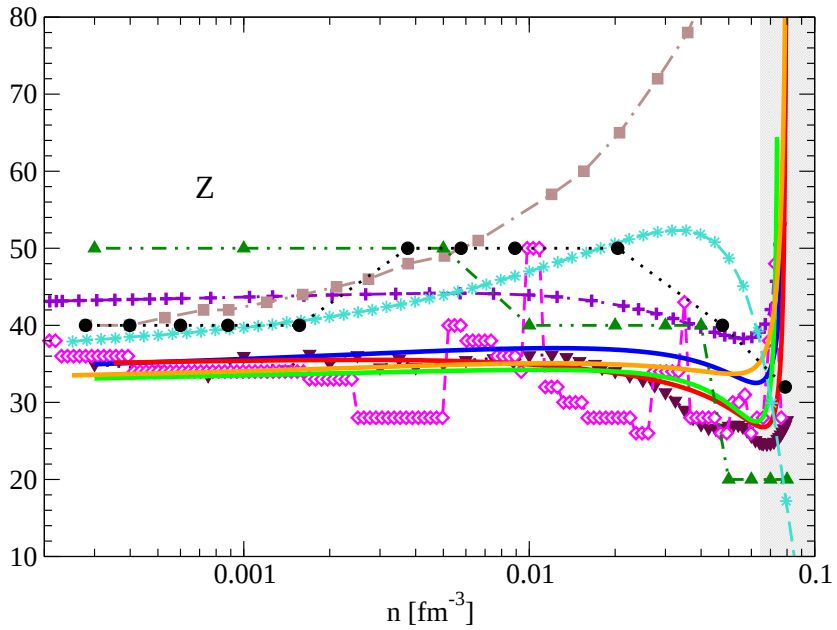

Figure 4.2: Proton number per cell Z as a function of the baryon number density n. The legend is the same as in Figure 4.1.

The value of Z (Figure 4.2) is included in the range $20 - 50$ for almost all the models mentioned. The number of protons has small variations for BSk14, SAMi, SkM*, SLy4 (around 35 ± 3) till higher densities, where our framework is characterized by a decreasing amount of protons as a function of the increasing density. A similar behaviour can be seen also for BCPM (the closest to our parametrizations), CPR and DH even if the initial value of protons is higher. The S model shows an oscillating trend, counting from 25 to 50 Z. Other models like NV and KP present an increasing number of protons and then a decreasing Z for densities up to 0.01 fm^{-3}. Again, the behaviour of BBP is

an exception: it starts from less than 40 Z at the beginning of the inner crust and reaches over 120 protons at $n \sim 0.08$ fm^{-3}.

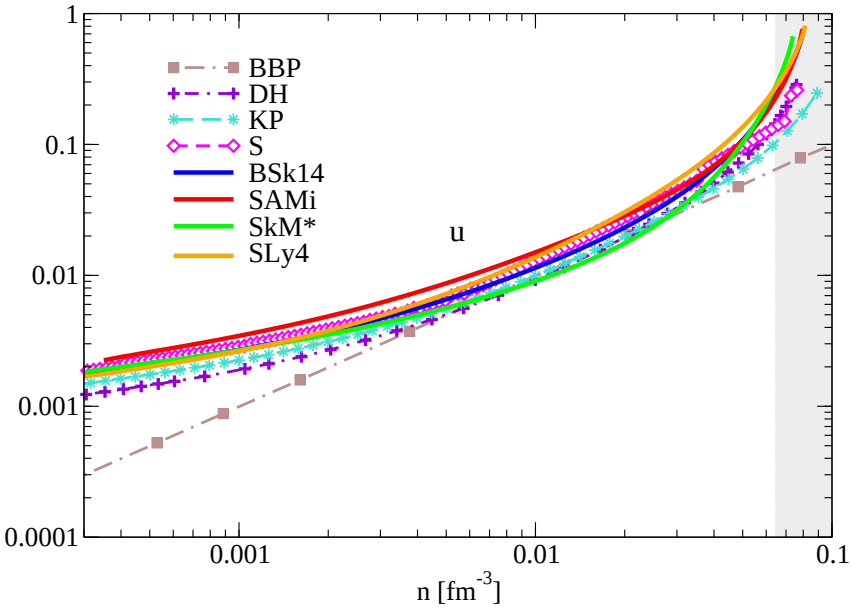

Figure 4.3: The volume fraction u as a function of the baryon number density n.

The values of u in our framework made with the four Skyrme interactions chosen differ by about 65% at 0.01 fm^{-3} and this difference increases with the density. Up to 0.05 fm^{-3} the SkM* has smaller volume fraction and after that density it inverts its trend. The trend of u for our model indicates a possible transition with uniform matter for half the values of the saturation density but, as told before, we can not exclude that the trend at higher density may be driven by other effects such as the appearance of different phases. The DH and S models reach the same value of $u \approx 0.3$ at ~ 0.076fm^{-3} and for lower densities the values of S are systematically higher than the DH ones. Data from KP allow simil maximum for u but reached at higher density, ~ 0.09fm^{-3}. The slope of BBP is the smallest: the volume fraction is 0.08 at ~ 0.08 fm^{-3} and converges to ~ 0.15 around the saturation density (not displayed in figure).

In Figure 4.4 the behaviour of the total proton fraction Y_e for densities over 0.005 fm^{-3} is quite similar for all the models: the values vary for example at 0.01 fm^{-3} from ~ 0.05 for KP to ~ 0.025 for SkM*. As long as the density decreases, the differences among the models become more relevant. At lower densities, BBP has a rapidly decreasing proton fraction, 0.08 at 5.3×10^{-4} fm^{-3}, compared for example with 0.13 of S and 0.18 of CPR. Close to the neutron drip density, S has the smallest proton fraction (0.19) and KP the biggest (0.36). It is interesting to underline that the percentage variation of Y_e in Figure 4.4

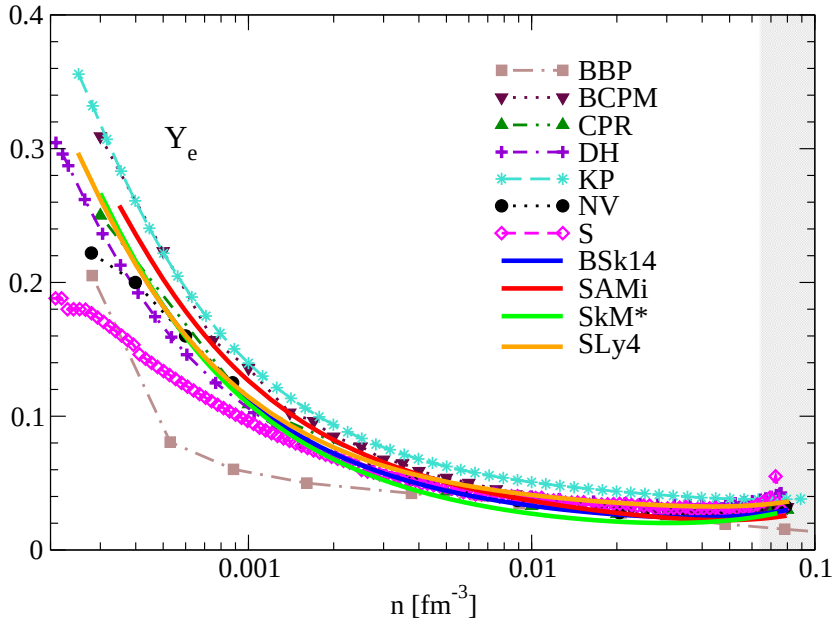

Figure 4.4: The total proton fraction Y_e as a function of the baryon number density n.

among all the models mentioned for the whole density range is relevant, around 100%.

4.2 Pressure and adiabatic index

We study the pressure of our model, how it varies in function of the density, and how it can be compared with other works. We also calculate the value of the adiabatic index Γ and briefly report what this parameter suggests about the physics of the crust of NS.

The pressure P of a system with total energy per baryon e, having total baryon density n, is defined in (2.23). From the studies of EoS for dense matter and star structure (*1*), it is known that the pressure is a key element to determine the mass-radius relation in NS. The crustal pressure is provided by the Fermi gas of electrons and by the superfluid dripped neutrons (*44*), while the dominant contribution to the total pressure of NS is the degeneracy pressure of neutrons (*1*). The adiabatic index Γ is defined as

$$\Gamma = n\frac{\partial P}{\partial n}. \tag{4.1}$$

The adiabatic index is very sensitive to how the transition from nuclei to uniform matter is taken into account (*38*), but also to the value at which

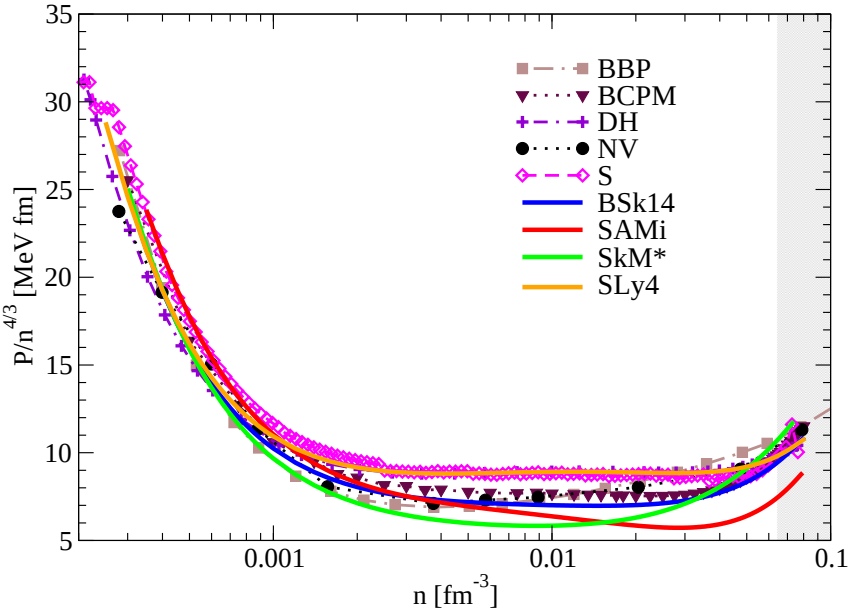

Figure 4.5: Pressure as a function of the total baryon number density of the cell n.

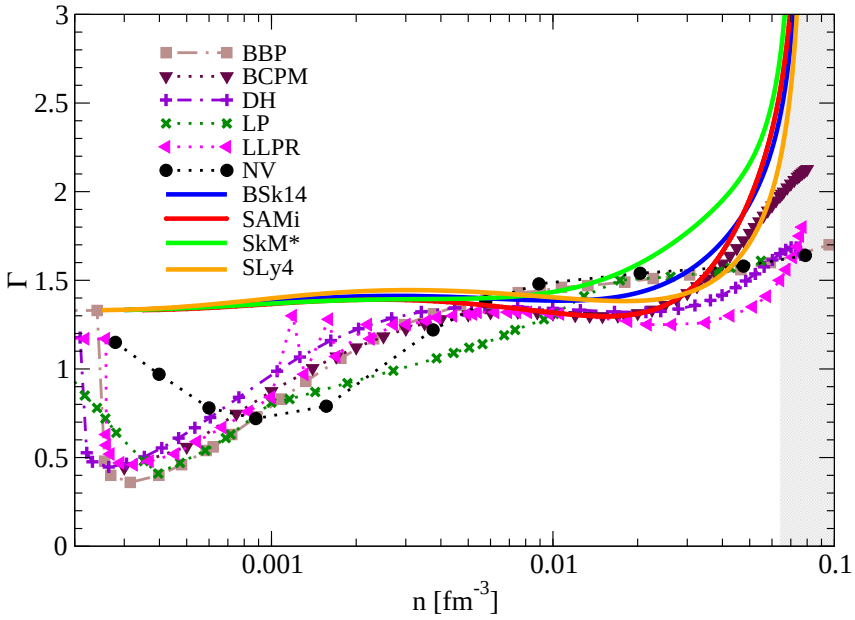

Figure 4.6: Γ as a function of the total baryon number density of the cell n. Data in LP (*7*) are taken from (*14*) and LLPR indicates (*40*).

this transition happens (i.e. to the neutron drip density value). This may contribute to explain why our model can not reproduce the diminish in Γ values above the neutron drip density, displayed in Figure 4.6 for other works.

For lower densities, from 10^{-8} to 10^{-4} fm^{-3}, we have $\Gamma \sim \frac{4}{3}$. This is because in the outer crust layers, the pressure is very well approximated by the sum of the main contribution given by the ultrarelativistic electron Fermi gas (*1*) and a second contribution given by the lattice, which both have the same density dependence $\propto n^{4/3}$ (*2*). At neutron drip, the pressure is almost entirely due to electrons but as the density increases, the free neutrons dripped from nuclei supply an increasingly larger fraction of the total pressure (*1*, *2*). For example, at 0.001 fm^{-3}, the contributions of electrons and neutrons in our model (calculated for the four Skyrme parametrizations BSk14, SAMi, SkM*, SLy4) are $P_e/P \approx 0.80$ and $P_n/P \approx 0.20$. When we reach densities of the order of 0.003 fm^{-3}, in the external part of the inner crust, the contribution given by the neutron gas outside the nuclei is comparable with the electronic one. At 0.01 fm^{-3} we have $P_e/P \approx 0.25$ and $P_n/P \approx 0.75$. We see in the range $n_{drip} \lesssim n \lesssim 10n_{drip}$ in Figure 4.6 how the value and the behaviour of the adiabatic index vary. This is mainly due to the fact that this is a transition region in which the pressure is not dominated by a single contribution. Since the composition of the inner crust is EoS dependent, the values of P_e/P, P_n/P depends on the choice of the model used. The more we approach to the crust-core transition density, the strongest becomes the contribution of the neutron gas. The density dependence of the superfluid neutrons is not a simple gas dependance $\propto n^{5/3}$ because they are interacting particles (*38*).

The decrease of Γ for $n \gtrsim n_{drip}$ indicates a softening of the EoS in the density region following the neutron drip point (*2*), which corresponds to an increase in slope of the density distribution (*39*). This means, in particular, that no stable stars can exist with central densities around neutron drip density, because the compressibility of the matter is too low. Then the EoS stiffens gradually, with a significant increase of Γ at the bottom layers of the inner crust (*2*, *39*) due to the flatness of the density distribution near nuclear density.

4.3 Static analysis

4.3.1 Fitting parameters

In subsection 2.1.2 we have shown that the bulk energy (2.6) can be written as a function of some parameters. It comes from the assumption that, to the lowest order expansion, the energy per particle $e(n, \delta)$ in infinite asymmetric nuclear matter of density $n = n_n + n_p$ (n_n is the neutron density and n_p is the proton density) and relative neutron excess $(1 - 2Y) = \frac{n_n - n_p}{n}$ (also known as δ), can be approximately written as the sum of the energy per nucleon of

symmetric matter $e(n, 0.5)$ and an asymmetry term $S(n)$ (*71*) as

$$e(n, Y) = e(n, 0.5) + S(n)(1 - 2Y)^2 + \mathcal{O}((1 - 2Y)^4) \tag{4.2}$$

where

$$S(n) \equiv \frac{1}{2}\frac{\partial^2 e(n, Y)}{\partial Y^2}\bigg|_{Y=0.5}. \tag{4.3}$$

The equation (4.2) can be expanded around the saturation density n_∞ as follows

$$e(n, 0.5) = e(n_\infty, 0.5) + \frac{1}{2}\frac{\partial^2 e(n, 0.5)}{\partial n^2}\bigg|_{n=n_\infty}(n_\infty - n)^2 + \dots \tag{4.4}$$

$$S(n) = S(n_\infty) - \frac{dS(n)}{dn}\bigg|_{n=n_\infty}(n_\infty - n) + \frac{1}{2}\frac{\partial^2 S(n)}{\partial n^2}\bigg|_{n=n_\infty}(n_\infty - n)^2 + \dots . \tag{4.5}$$

We define

$$e_\infty \equiv e(n_\infty, 0.5) \tag{4.6}$$

$$K_\infty \equiv 9n_\infty^2 \frac{\partial^2 e(n, 0.5)}{\partial n^2}\bigg|_{n=n_\infty} \tag{4.7}$$

$$J \equiv S(n_\infty) \tag{4.8}$$

$$L \equiv 3n_\infty \frac{dS(n)}{dn}\bigg|_{n=n_\infty} \tag{4.9}$$

$$K_{sym} \equiv 9n_\infty^2 \frac{\partial^2 S(n)}{\partial n^2}\bigg|_{n=n_\infty} \tag{4.10}$$

and substituting these parameters in (4.2) leads to the expression (2.6), apart from the Δ term and the K_{sym} term.

We now introduce the role of these parameters for our study in determining and conditioning the characteristics of a system.

The **nuclear saturation density** for SNM n_∞ is one of the basic parameters of nuclear models and its value is equal to 0.160 ± 0.005 fm^{-3}. The value of saturation density is almost a constant because it strictly depends on the saturation property of the nuclear force. It is known that the nucleons interact with each other through the strong force, which acts in a short range. In this way, every single nucleon can interact only with a finite number of other nucleons surrounding it, on average with all the remaining particles far from it. The n_∞ value is suitable for most of the nuclei, in particular for those which we consider here. It may vary according to the type of potential chosen to describe the nuclear force, so it can be slightly different in different models, but even in

this case, the variation can not be significant. In our analysis for example its value varies less then 5%. In case of a wider variation of the saturation density (the order of $\gtrsim 10\%$ from the mean value of 0.16 fm^{-3}) the model is not able to reproduce the property of ordinary nuclei.

The **nucleon radius** r_o is calculated from the saturation density, so its range can not be wide too. Its mean value is 1.15 fm with a variation less then 1%.

A similar way of thinking can be done for the **binding energy** per nucleon e_∞ calculated at the saturation density for SNM. It has a mean value of ≈ 16 MeV and the variation in our Skyrme analysis is less than 1%. Values of the saturation energy are derived from nuclear mass formula fits (*49*). This term could not significantly vary from the mean value, but it is still possible to have a slightly different value depending on the Skyrme parametrization chosen, like for the saturation density. The importance to consider these parameters as contant allows us to simplify the sensitivity analysis and to hold in check a minor number of free parameters, without lacking in generality or loosing sight of the importance of our study; on the contrary this is a valid solution to outline and eliminate the unnecessary.

The **bulk modulus** (or nuclear incompressibility) K_∞ indicates the incompressibility of a nucleus. It is related to the curvature of the bulk energy per particle in SNM around the saturation point by the definition (4.7). The magnitude of the incompressibility is determined by the choice of the approach, whether classical (CLDM) or microscopic (Skyrme HF). In very truth, the parameter K_∞ does not perform an influential role concerning the binding energy, because into the formula of the bulk energy (2.6) appears as a second order correction $\propto (n/n_\infty)^2$. For our analysis, we can not examine in depth the variations caused by different values of the incompressibility modulus because the range allowed for reasonable K_∞ is small, 245 ± 15 MeV. However, we can figure out that the bulk modulus indicates the energy required to compress a WS cell; for lower values of K_∞, this imply to have bigger WS cells and consequently bigger r_C. Keeping the neutron gas density n_o almost constant, the total number of baryons A must increase. The nucleus is modified because of the Coulomb repulsion among cell for diminishing values of K_∞: we see a bit bigger nucleus (r_N raises) with an increment of internal density n_i and of the number of nucleons A_i. Moreover, the number of protons Z grows, in order to keep the internal proton fraction Y_i roughly constant and as a result, also the total proton fraction Y_e is quite constant.

The symmetry energy is the energy cost of creating an isospin asymmetry in nucleonic matter. In particular the **symmetry energy coefficient** J (4.8) is correlated to the binding energy of uniform matter: as J becomes larger,

the n-p asymmetry decreases because the energy required to create a neutron from a proton increases. The parameters J and its slope L (4.9) are widely studied as the range of possible values for our analysis are $J = 29 \pm 3$ MeV and consequentely $L \approx 50 \pm 20$ MeV (this two parameters have been shown to be correlated). So the reduction of symmetry energy J indicates the trend of the matter to enlarge its asymmetry instead of its symmetry, and the number $N-Z$ inside the nucleus must increase. In fact we can see that, as J enlarges, the number of protons Z becomes smaller, and the value $\frac{A_i-2Z}{A_i}$ becomes bigger (for a more detailed discussion, see (*72*)). The nuclear radius r_N decreases and the internal density n_i increases, as follows the number of nucleons A_i is reduced (in general, we have also to consider the role of L and so it is more difficult to understand exactly which is the cause of a particular effect). Because of the presence of less protons, the Coulomb repulsion among different WS cells fades. This allows to have smaller cells, with smaller r_C, filled with a minor number of baryons A, but keeping a roughly constant neutron gas density n_o. Finally, the total proton fraction Y_e must decrease.

The **effective mass** m^* is the mass that a particle seems to have when responding to forces, or seems to assume in a thermal distribution together with other identical particles. In the band theory of solids the motion of particle subject to a potential can be difficult to study, so the effective mass is used to simplify band structures by creating an analogy to the behavior of a free particle with $m = m^*$. We can imagine that, since a bigger mass can be correlated with lower values of the kinetic energy (and consequentely a smaller number of states avaliable), as m^* increases, the number of A allowed per cell should diminish, as well as for Z and A_i. As a consequence, the cell radius and the nuclear radius are smaller. The total proton fraction Y_e decreases while the internal proton fraction Y_i may increase by the fact that, for bigger effective masses, the percentage diminish of the inner baryon number is major with respect to the proton one.

The effects due to the **surface symmetry energy** S_s may not be immediately clear. We see that the surface symmetry energy S_s plays a role into the definition of σ. If we analyse numerically which is the most important term into σ, we notice that S_s enters both in the numerator and in the denominator as a fraction. Since the numerator is numerically bigger than the denominator for every value of Y_i, we obtain that σ strictly depends on the inverse of S_s. As S_s increases, σ decreases, and consequently the nuclear radius r_N becomes smaller. The nucleus looses nucleons, so both Z and A_i decrease, even if the internal density n_i increases a few percent its value. The diminishing of Coulomb repulsions among cells allow to reduce the value of r_C and consequently the number of baryons A inside the cell (keeping n_o quite constant). We see an

increment in Y_i because the loss of neutrons is percentage greater compared to the loss of protons, and also an increment in Y_e.

Another important parameter in our model is σ_s, the **surface tension** of SNM. In literature is often used the surface energy a_s instead of our σ_s. For simplicity, we decide to use the more common parameter, and we use the relation (2.9) to pass from one to the other (where we remember that the value of r_o is calculated by using the value of n_∞). An increment of a_s implies an increment of σ, obtaining a greater nucleus caused by an increment of r_N. The number of baryons A_i inside the nucleus rises, observing a more considerable growth in neutrons with respect to protons: this is the reason why the internal proton fraction Y_i decreases. The resulting WS cell is larger and receives a major number of baryons A, supporting a constant value of neutron gas density n_o, while the total proton fraction Y_e is reduced.

4.3.2 Modified SAMi

The variation of the values of the parameters may modify the composition and the characteristics of the system. This is the reason why we are interested in make a sensitivity analysis for our observables. We focus on the Skyrme parametrization SAMi: it allows to modify one parameter at a time without compromising the others since it is made ad hoc for sensitivity analysis. The nuclear properties of all the modified SAMi interactions used are similar and reasonable accurate for the description of quantities like nuclear masses and densities.

We modify the values of K_∞, J, m^*, underlining the differences and how the model reacts under the variation of a single condition and comparing the results with the original SAMi. We use the following values (from here, for semplicity we use the notation $K = K_\infty$); K: 230 (SK230), 260 (SK260) [MeV]; J: 27 (SJ27), 29 (SJ29), 31 (SJ31) [MeV]; $m*$: 0.6 (Sm6), 0.75 (Sm75), 0.85 (Sm85) [m]. The analysis made with the SAMi Skyrme allows us to study the variations of static quantities like A, Z, u and others.

Symmetry energy at saturation density J

The symmetry energy J and its slope at the saturation density L play a crucial role in the description of the inner crust. They are important parameters which variation can cause significant changes regarding the composition of the inner crust matter. For the SAMi parametrization we have that an increment in the value of J corresponds to an increment of L, so we can refer to J or L equally.

In Figure 4.7, for lower densities < 0.005 fm^{-3}, smaller values of J (and consequently of L) correspond to a bigger amount of baryons in WS cell. The

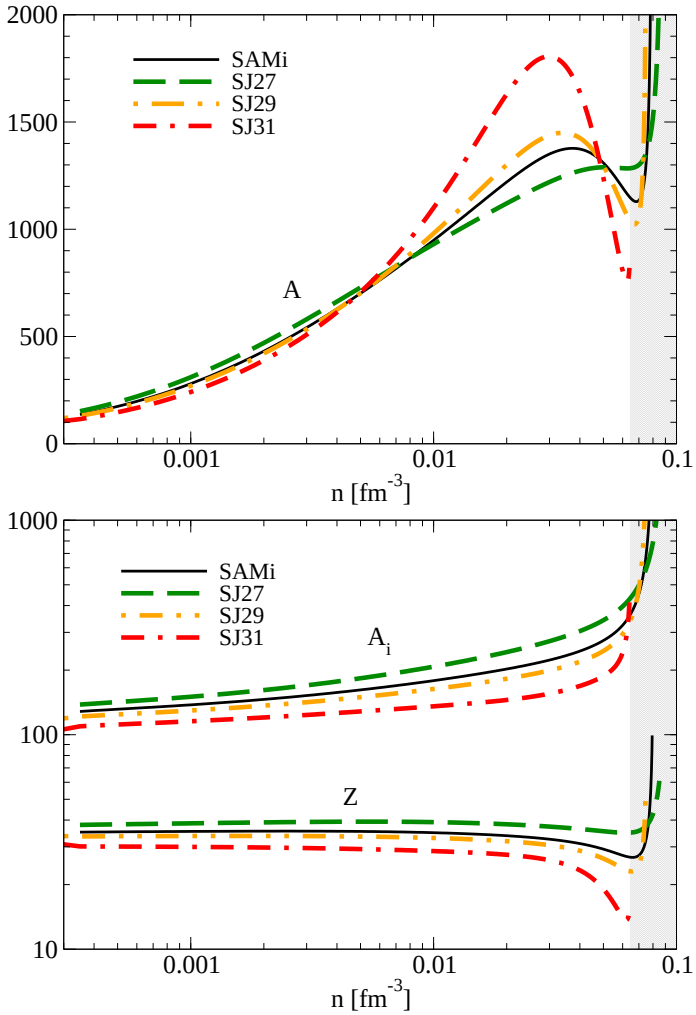

Figure 4.7: The total number of baryon per WS cell A (up) and the proton number Z and the baryon number inside nuclei A_i (down) as a function of the total baryon number density of the cell n.

differences among the parametrizations in this range are of the order of 100 baryons: at ~ 0.0014 fm^{-3} the maximum difference is about $\sim 30\%$ in baryon number. In the interval $0.005 - 0.05$ fm^{-3} there is a strong change in the trend: SJ31 grows with a major slope as a consequence of the fact that in this density range the bigger the J, the bigger the value of A. We see how the peak of the distribution is less pronounced and appears at higher densities for small J: for SJ31 are counted 1800 baryons at 0.03 fm^{-3} while for SJ27 there are 1280 baryons at 0.05 fm^{-3}. From 0.05 fm^{-3} the trend is newly inverted.

The behaviour of Z and A_i, displayed in Figure 4.7, says that we have fewer protons in the nucleus for bigger value of J and in general fewer baryons to

form the nucleus. The proton number does not have a remarkable variation till 0.02 fm^{-3}, where effects due to the increasing number of dripped neutrons may occur. At the lower limit of the inner crust we have 38 protons for SJ27 and 30 for SJ31, while at 0.03 fm^{-3} there are 37 protons for SJ27 and 25 for SJ31. The number of baryons inside the nucleus grows slowly and constantly, starting from about 105 (SJ31) and 135 (SJ27) close to n_{drip} to 183 (SJ31) and 335 (SJ27) at 0.05 fm^{-3}. Since the proton number is nearly constant, the increase is due to the large number of neutrons. In agreement with the results from (*35*) there is a strong correlation between L and the charge number of nuclei as well as with density region containing bubbles and non-spherical nuclei; pasta region diminishes with increasing L and vanishes with $L \sim 100$ MeV (*22*). The latter statement can be seen in the smoother behaviour of SJ27 than of SJ31 close to the n_{edge} for A and Z. A larger value of L also favours neutron drip and a smaller surface tension in asymmetric matter (*73*), which may explain the higher value of A close to the bottom layers.

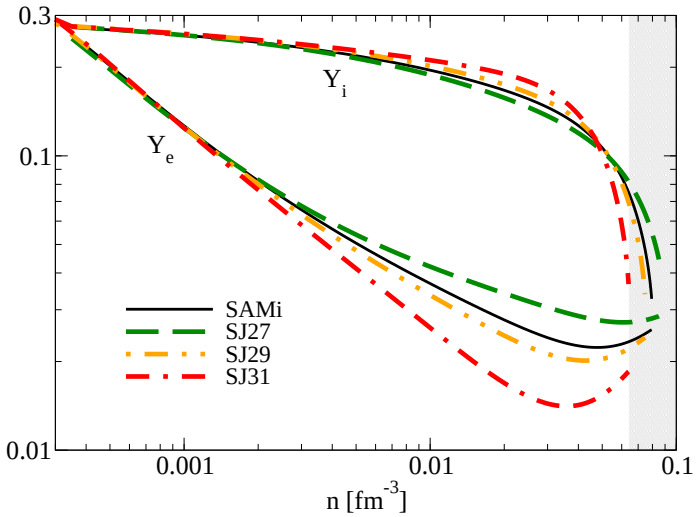

Figure 4.8: The total proton fraction Y_e and the proton fraction inside nuclei Y_i as a function of the total baryon number density of the cell n.

Below 0.001 fm^{-3} the proton fraction among the parametrizations varies around 5% with a tendency to have slightly bigger Y_e for SJ31, in accordance with the idea that for SJ31 correspond less protons and even lesser baryons than for SJ27. Over 0.001 fm^{-3}, the maximum deviation from the original SAMi takes place at ~ 0.035 fm^{-3} where the SJ31 curve has a value of 0.0137 and 0.029 for SJ27. This is caused by the high number of dripped neutrons generated by the SJ31 parametrization.

The proton fraction inside nuclei starts with the value 0.3 and has a nearly smooth behaviour till 0.001 fm^{-3}, then has an accentuate decrease reaching

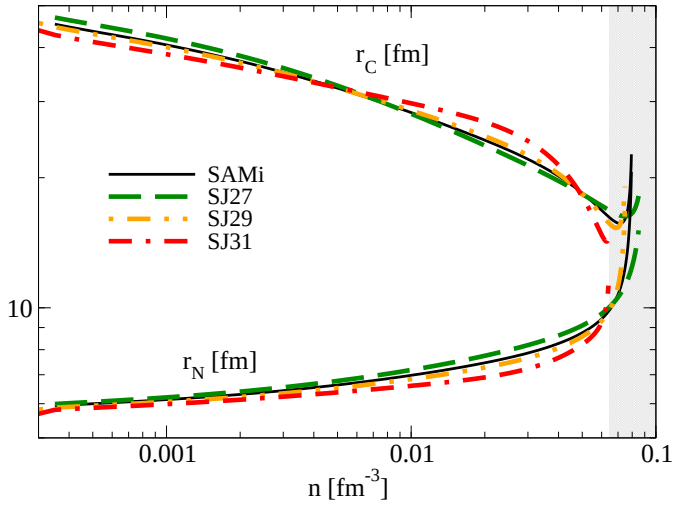

Figure 4.9: The radius of the WS cell r_C and the radius of the nucleus r_N as a function of the total baryon number density of the cell n.

1/3 of its initial value. The parametrization SJ31 allows bigger values of Y_i, i.e. more protons form the nucleus with respect to the quantity of internal baryons. Thus indicates that a bigger J permits smaller values of $N_i - Z$ which confirms the idea of maintain the symmetry inside the nucleus as much as possible. At 0.05 fm^{-3} we observe the usual change in trend, where the SJ31 drops and its internal proton fraction becomes smaller than the SJ27.

The radius of the cell in Figure 4.9 follows the same trend of the baryon number, i.e. for bigger values of the symmetry energy coefficient we observe smaller radii at lower densities and a growth of the cell at higher densities. The turning point occurs at ~ 0.005 fm^{-3} for the value of ~ 32 fm. As for A, for 0.05 fm^{-3} we have another trend change that we can relate to the possible beginning of the other phases. The maximum differences between SJ27 and SJ31 at 0.004 fm^{-3} and 0.025 fm^{-3} are few fm. It is interesting to notice that the deviation from the original SAMi with $J = 28$ MeV is smaller for SJ29 than for SJ27, especially for the upper layers of the inner crust.

The trend of the nucleus radius is consistent with the growing number of baryons inside nuclei. Nuclei are slightly bigger for smaller symmetry energy coefficients, even if the maximum difference caused by the parametrization is less than 15% and takes place at 0.03 fm^{-3}. Values of r_N start from 6 fm at two times the neutron drip density and reach the order of 10 fm at n_{edge}. The fraction of volume occupied by nuclei u (displayed in Figure 4.10) shows that for smaller J the model allows bigger nuclei till ~ 0.055 fm^{-3}. For example at ~ 0.04 fm^{-3} the value of u for SJ27 is almost the double of the SJ31 value. For higher densities it is pointed out which is the density limit

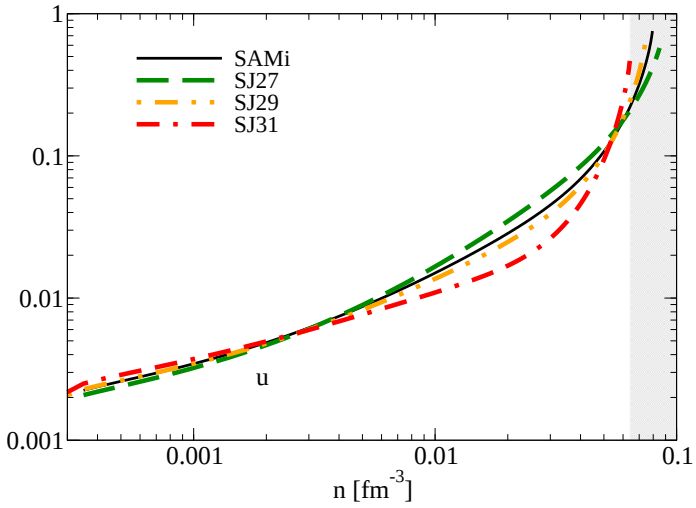

Figure 4.10: The volume fraction u as a function of the total baryon number density of the cell n.

for every parametrization and may be possible to understand how to explain it. Since a big value of L indicates a small region containing pasta phases, our model based on spherical nuclei can be a good description till 0.064 fm^{-3} (SJ31) for which the transition with the liquid core may occur. The possibility to reach $\sim$ 0.084 fm^{-3} (SJ27) can indicate the probable existence of multiple phases, including the spherical one, which may coexist.

Effective mass m*

As for the J, we observe in Figure 4.11 three regions in which the relation between effective mass and baryon number is inverted. Lower than 0.005 fm^{-3} the parametrization Sm6 is characterized by a larger number of baryon in every cell. The maximum percentage difference with the Sm85 happens at 0.0014 fm^{-3} and is less than 20%. Upper than 0.005 fm^{-3} and till 0.05 fm^{-3} the increment in slope of Sm85 reveals that for higher densities are allowed more baryons for bigger values of the effective mass. This is because the surface energy and the Coulomb energy contributions are stronger for bigger m^* at high densities, which means that neutrons prefer to be bounded to nuclei than to drip. The behaviour of the Sm85 and Sm75 distributions are quite similar while the Sm6 differs for a higher percentage from the SAMi. The peak of Sm85 is at 0.032 fm^{-3} and counts $\sim$ 1460 baryons; there is a fall to 950 baryons at 0.07 fm^{-3}. The Sm6 reaches $\sim$ 1250 baryons at 0.047 fm^{-3} and then has a nearly flat trend till the bottom layers of the inner crust.

The proton number shows a very smooth trend for all the parametrizations

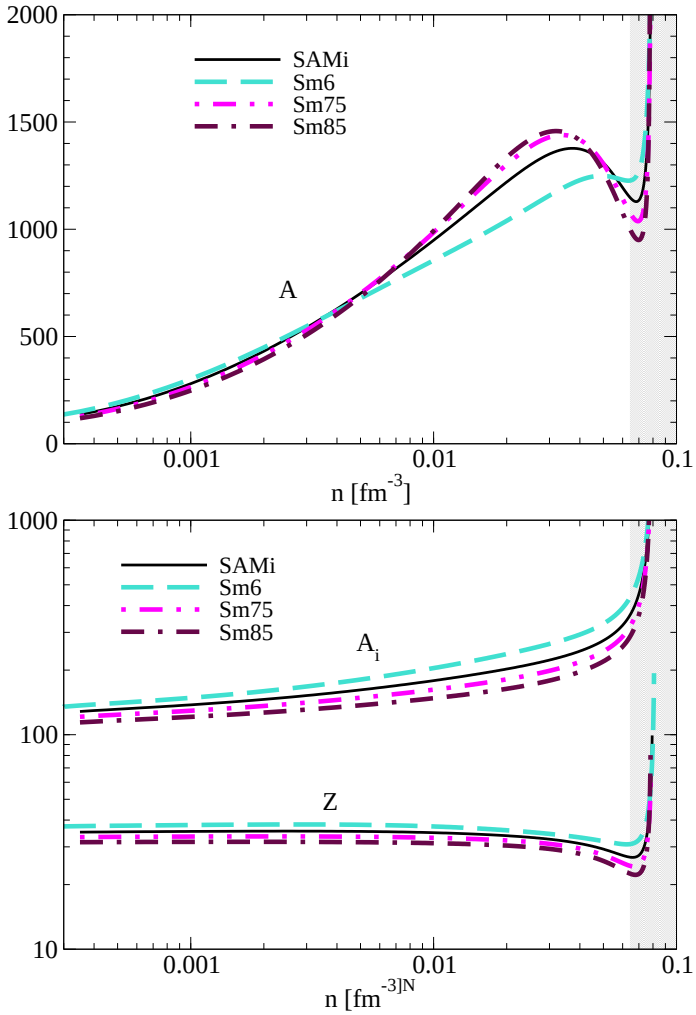

Figure 4.11: The total number of baryon per WS cell A (up) and the proton number Z and the baryon number inside nuclei A_i (down) as a function of the total baryon number density of the cell n.

throughout almost all the inner crust, save the region around n_{edge}. For Sm85 there are 31 protons till 0.018 fm^{-3} and a minimum value of 22 at 0.07 fm^{-3}. The protons allowed for Sm6 are more than for Sm08 and vary from 31 to 38 for all the densities. The number of baryons inside nuclei has a increasing trend, where the major number of A_i corresponds to a minor value of m^*. Close to the saturation density, the values of inner baryons are 120 (Sm6) and 115 (Sm85) and grow to 550 (Sm6) and 360 (Sm85) at 0.07 fm^{-3}.

Even if for lower densities up to 0.0012 fm^{-3} there is not a considerable difference (around 6%) among the parametrizations, it is possible to see that the total proton fraction assumes higher values for bigger effective mass. As

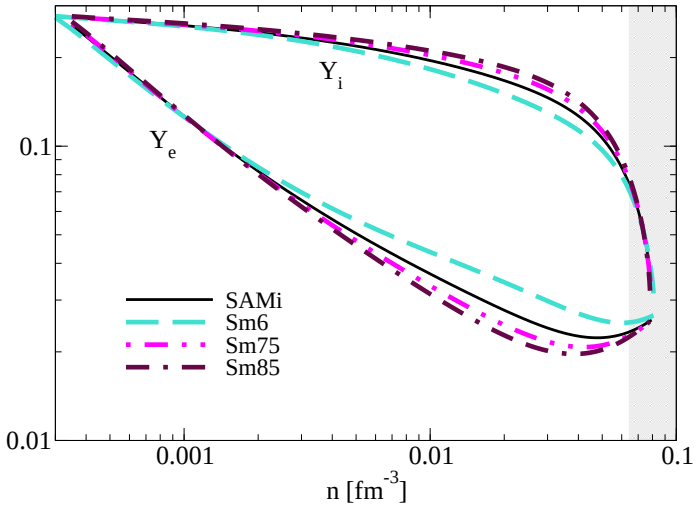

Figure 4.12: The total proton fraction Y_e and the proton fraction inside nuclei Y_i as a function of the total baryon number density of the cell n.

the density increases, the separation between the curves increases, especially for Sm6 and Sm85, while Sm75 has a similar behaviour with respect to Sm85. Sm85 has a pronounced minimum at 0.038 fm^{-3} with a value 0.0197 and Sm6 has a minimum in 0.06 fm^{-3} with 0.025.

The proton fraction inside nuclei has higher values for bigger effective mass. This can be commented by the fact that for smaller m^*, the nuclei are more particle rich, but a smaller number of protons can be bounded to nuclei because of the Coulomb repulsion with respect to great number of neutrons allowed. Having less particles inside nuclei leads to a higher ratio between Z and N_i. The difference among the parametrizations increase with the density, has a maximum of about 30% at ~ 0.03 fm^{-3} and becomes null close to the transition with the core.

We can notice how, for high densities, the parametrizations in Figure 4.12 converge to about the same Y_e and Y_i values, in spite of what shown in Figure 4.8. In fact J affects the kind of interaction, and as a consequence the structure of the model varies while m^* modify the geometric dimensions of the system (i.e. radii), but the interaction which is acting does not change because the parameters such as K, J, L are equal in the m^* analysis.

The cell radius is bigger for smaller values of effective mass below the density 0.05 fm^{-3} and becomes smaller over that density, in accordance with the total baryon number in every cell. Close to the neutron drip density we have 43 fm for Sm85 and 46 fm for Sm6. The minimum values of the curves are very similar, 15 (Sm85) and 16 fm (Sm6) at ~ 0.07 fm^{-3}. Throughout all the density range, the differences of r_C between the parametrizations are less

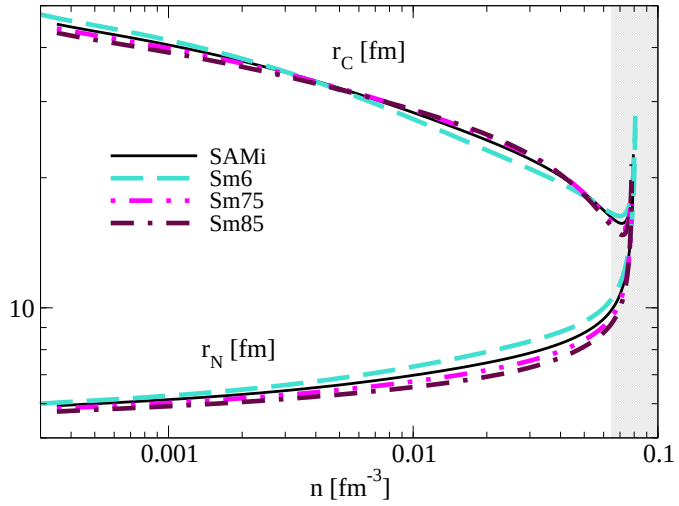

Figure 4.13: The radius of the WS cell r_C and the radius of the nucleus r_N as a function of the total baryon number density of the cell n.

than 10%, which means that the value of the effective mass does not have a relevant role in determining the dimensions of the cells.

As a consequence of the analysis about the inside baryons, the radius of the nuclei is slightly bigger due to the bigger number of bound particles for smaller effective masses (*74*). The difference grows with the density but similarly with the cell radius, the nuclear radius has not a serious variation for the different values of m^*: the maximum difference is 15% at 0.03 fm^{-3}. Over 0.072 fm^{-3} we

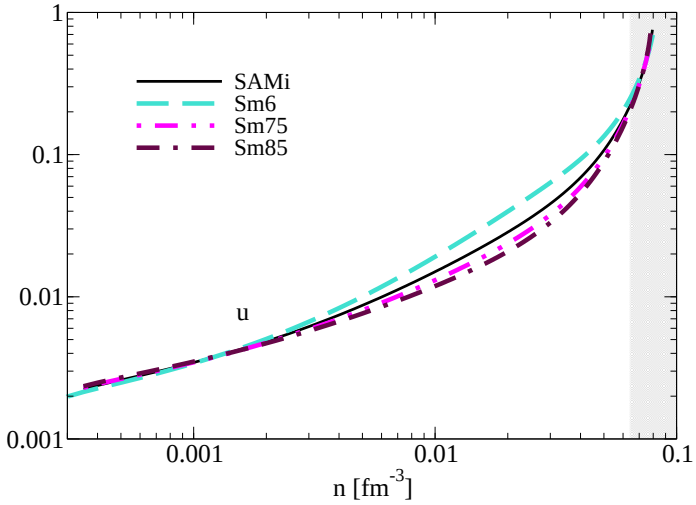

Figure 4.14: The volume fraction u as a function of the total baryon number density of the cell n.

also observe an increase of the r_C ad eventually, close to 0.08 fm^{-3}, the values of cell radius and nuclear radius coincide. Even if these results are interesting and may be used to give an idea of the behaviour of the matter at the bottom layers of the inner crust, we can not discriminate between the actual transition with a uniform matter or an effect due to the algorithm.

The fraction of volume occupied by the nuclei u increases with small effective masses as a result of the dimensions of cell and radius till 0.075 fm^{-3}, where the trend undergoes to an inversion. The differences among the values of m^* are smaller than 50% and become significant over 0.01 fm^{-3}. It is interesting to notice how all the parametrizations at high densities tend to a similar value of u, for example the fraction volume value of 70% is reached at 0.078 fm^{-3} for Sm85 and at 0.08 fm^{-3} for Sm6. In fact, as discussed before, the variation of the effective mass does not affect the characteristics of the framework and so the transition density may be slightly dependent on the effective mass value.

Bulk modulus K

The variation of the bulk modulus K does not affect significantly neither the structure nor the characteristics of our framework. A change in the value of K for the SAMi Skyrme does not cause any change in the other parameters, as for m^*/m.

As shown in Figure 4.15, the number of total baryon per cell as well as

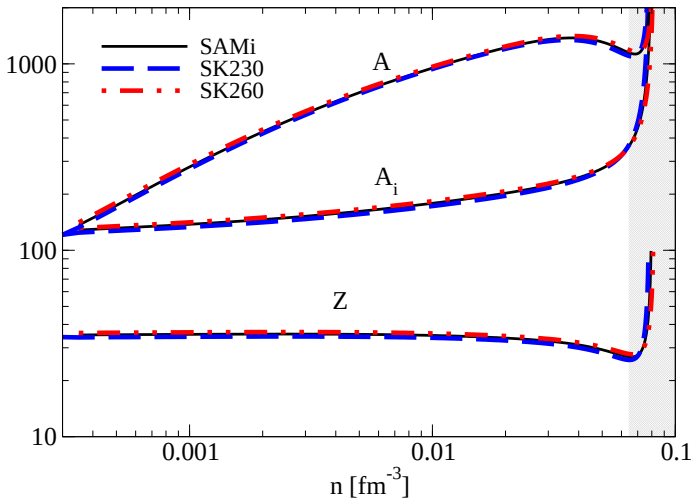

Figure 4.15: The total number of baryon per WS cell A, the proton number Z and the baryon number inside nuclei A_i as a function of the total baryon number density of the cell n.

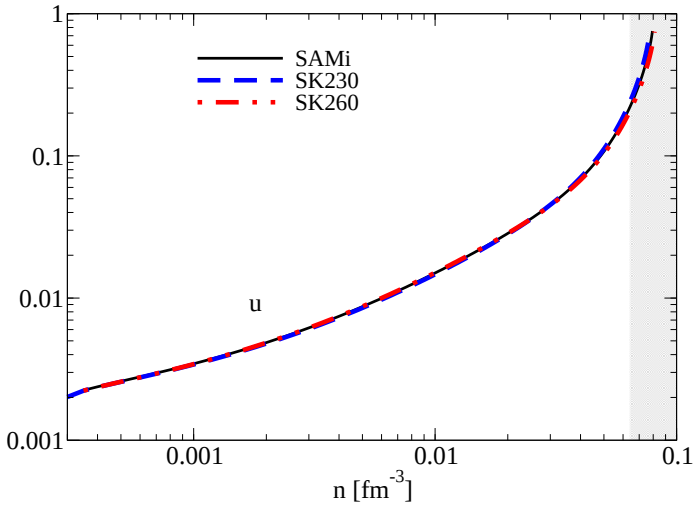

Figure 4.16: The volume fraction u as a function of the total baryon number density of the cell n.

the proton number and baryons inside nuclei weakly depends on the value of K. The variations between SK230 and SK260 are less than 10% for all the density range. It can be seen however how a bigger value of K produces bigger nuclei and bigger cells, which means to have more protons and neutrons inside nuclei and a major number of baryons in every cell until ~ 0.05 fm^{-3}. Over this density, the trend of the nuclear radius is inverted as well as the number of inside baryons. Since a smaller incompressibility gives a smaller surface tension (*73*), the behaviour described is well predicted.

The volume fraction u has corresponding values for both SK230 and SK260 until ~ 0.04 fm^{-3}. For high densities, the differences increase with the density and the value of $u \approx 0.70$ is reached at 0.077 for SK230 and at 0.08 for SK260. The total proton fraction does not show any relevant variation caused by the different value of the bulk modulus. Similarly, the inner proton fraction is quite similar up to 0.042 fm^{-3}, from where the parametrizations take distances from each other for a maximum difference of 15%.

Chapter 5

Numerical results from the collective modes

Similarly of what has be done in the previous chapter, we first present a qualitative discussion about the dynamic quantities, making a comparison with few other works. Then we focus on our model, showing the results of a sensitivity analysis made on the velocities of the modes for a variation of some parameters. In closing, we consider different values of entrainment parameter and how this quantity is relevant in modifying the dispersion relations.

5.1 General overview

We briefly underline few behaviours and state some approximations that can be considered as general in our system when we set the entrainment parameter $\alpha = 0$ (3.1).

The velocity mode of the lattice v_p has a nearly flat behaviour for almost all the inner crust density range with a more accentuate increasing trend close to the bottom layers of the crust.

The superfluid mode velocity v_n has an increasing trend through the inner crust. It is known that the velocity of propagation of a sound wave depends on the density of the material in which it is propagating: as long as the density increases, so does the velocity.

We notice how, at lower densities, the behaviours of v_- and v_+ are similar to v_n and v_p. We consider the definition of $v_\pm$ in (3.28): the term v_{np}^4 is one order of magnitude smaller than the other terms under the square root. If we neglect it, (3.28) is easily solved and the exact solutions are $v_+ = v_p$ and $v_- = v_n$. The validity of the approximation $v_{np} \approx 0$ is acceptable until ~ 0.03 fm^{-3}: for SAMi at 0.02 fm^{-3} the difference between the values of $v_n - v_-$ is less than 1%

and reaches $\sim 10\%$ at 0.036 fm^{-3}. The differences $v_+ - v_p$ calculated at the same densities are just few percentage smaller.

The transverse mode velocities are defined as in (3.22). We can rewrite that equation underlining which are the dominant quantities: since $m(n_p + n_n^b) \sim mn_i u^{-1}$ (in case of $\alpha = 0$ in (3.1) this relation is exact) and the shear modulus in (3.35) is proportional to $Z^2 r_c^{-4}$, we obtain

$$v_t \propto \frac{Z\sqrt{u}}{r_c^2\sqrt{mn_i}}. \tag{5.1}$$

Even if in literature the velocities are often calculated with respect to the bare mass m, we prefer to use the effective mass m^* for our numerical analysis. We simply apply the substitution $m \to m^*$ in all the equations concerning the calculation of the velocities.

5.2 Comparative analysis

A pioneering calculation of modes of the inner crust is performed by Epstein (*11*): even if the role of entrainment is taken into account, it is not considered the role of the coupled modes, i.e. the reciprocal effects caused by the superfluid and the lattice together. Collective modes under the hydrodynamic approximation, made by KP (*75*) and CPR (*46*), are more similar to what we make in our study. So we make a comparison between our model, using the four parametrizations BSk14, SAMi, SkM*, SLy4 and the works of CPR (*46*), KP (*75*) and Page & Reddy (PR) (*26*). The velocities from these models, used for our analysis and displayed in Figure 5.1 and Figure 5.2, are calculated without considering the entrainment effect and in our framework we set $\alpha = 0$ in (3.1).

For the lattice mode velocity we recognize two classes of behaviour. Our model is characterized by a smoother trend, allowing a slightly increasing values for lower densities (more accentuated in particular for SLy4) and a successively decrease until reaches a minimum value around one third of the saturation density. After that, we have a pronounced increase. Similarly, PR has an increasing trend and a maximum value in correspondence of our minimum and then a little accentuated decrease. CPR and KP instead show a slightly increasing trend throughout all the inner crust. We can assume that the almost constant value of v_p for our four parametrizations is a consequence of the choice of the model, since CPR and BSk14 use the same Skyrme interaction but they have a different trend.

The superfluid mode velocity has increasing values for all the models considered. At the neutron drip density it starts with $0.007c - 0.013c$ (respectively

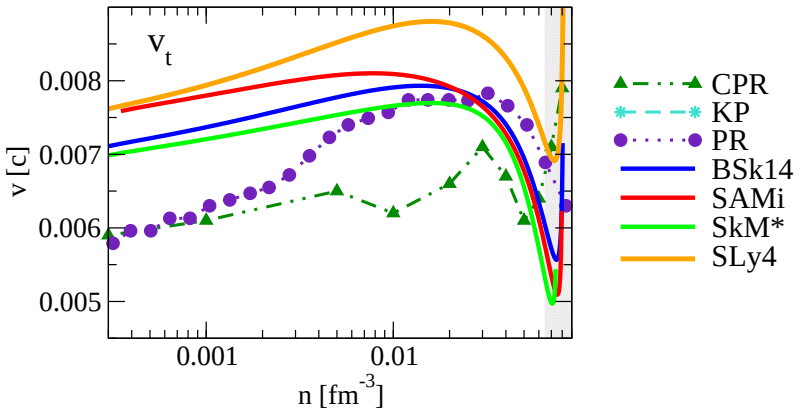

Figure 5.1: A comparison between the velocities of the transverse mode v_t in units of the light velocity c calculated for our model with $\alpha = 0$ and by CPR (*46*) and PR (*26*) without the entrainment.

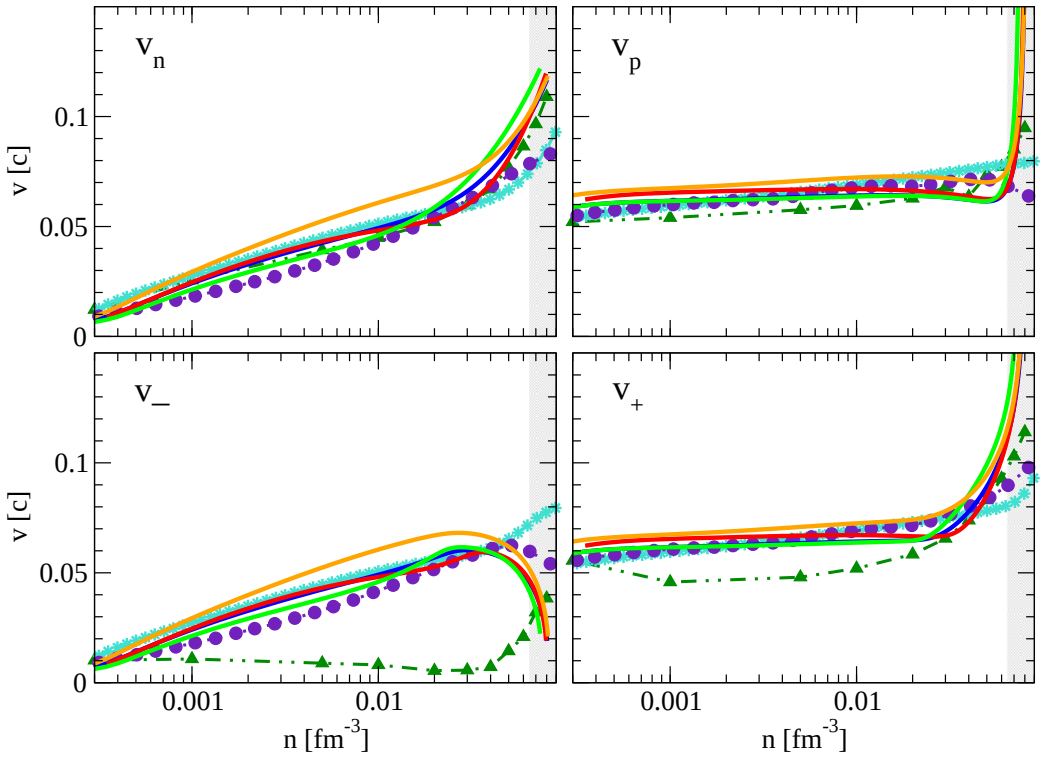

Figure 5.2: A comparison between the velocities of the longitudinal modes v_n, v_p (including coupled modes $v_\pm$) in units of the light velocity c calculated for our model with $\alpha = 0$ and by CPR (*46*), KP (*47*) and PR (*26*) without the entrainment.

SkM*-KP) and reaches values in the range $0.066c - 0.095c$ (KP-SkM*) at $\sim 0.3n_\infty$. Around 0.01 fm^{-3} we notice a subtle diminish in the slope of v_n and a following increment after 0.03 fm^{-3}. The SLy4 has a stronger increment than the others, in fact at 0.01 fm^{-3} the velocity has a value $20\% - 35\%$ greater than mean values $0.043c - 0.050c$, while PR shows a slower increase for densities below 0.01 fm^{-3}.

For the v_- we see how our model, PR and KP data have an increasing trend from the beginning of the inner crust and till 0.03 fm^{-3}. From there KP continues increasing while our parametrizations and PR decrease: the maximum value allowed in this range is $0.068c$ for SLy4. CPR has significantly smaller values of v_-, more than one order of magnitude, with a minimum value of $5.5 \times 10^{-3}\, c$ and a growing trend at the bottom layers of the inner crust. Similarly, for the v_+ CPR has a different behaviour with respect to the other data used. It presents a minimum around 0.001 fm^{-3}, 30% smaller than the value assumed by KP for the same density. It increases and eventually for high density it becomes comparable with our model. The trend of KP and PR are smoother than CPR and slightly increasing, while for our model we see a more flat behaviour. Definitely, the coupled mode velocities calculated by CPR do not respect the approximate condition $v_{np} \approx 0$.

The transverse modes velocity for CPR has oscillating values that are part of the range $6 \times 10^{-3}\, c - 8 \times 10^{-3} c$; the values for our model are at least 15% bigger till the bottom layer of the crust. Close to neutron drip density, the values for PR are the same order of CPR's.

5.3 Dynamic analysis

5.3.1 Modified SAMi

The analysis made with the SAMi Skyrme sets concerns the study of the dynamic quantities such as the velocities of transverse and longitudinal modes v_t, v_n, v_p, v_+, v_- when we vary the values of K, J, m^*. The velocities are calculated considering $\alpha = 0$.

Symmetry energy at saturation density J

The velocity mode of the lattice v_p has a mean value around $0.065c$ and reaches a nearly accentuated minimum in the range $0.045 - 0.055$ fm^{-3} depending on the value of J (major density for smaller J). After the minimum, v_p has a sharp increase which happens firstly for higher symmetry energies. The lattice mode does not show a relevant dependence on the value of the symmetry

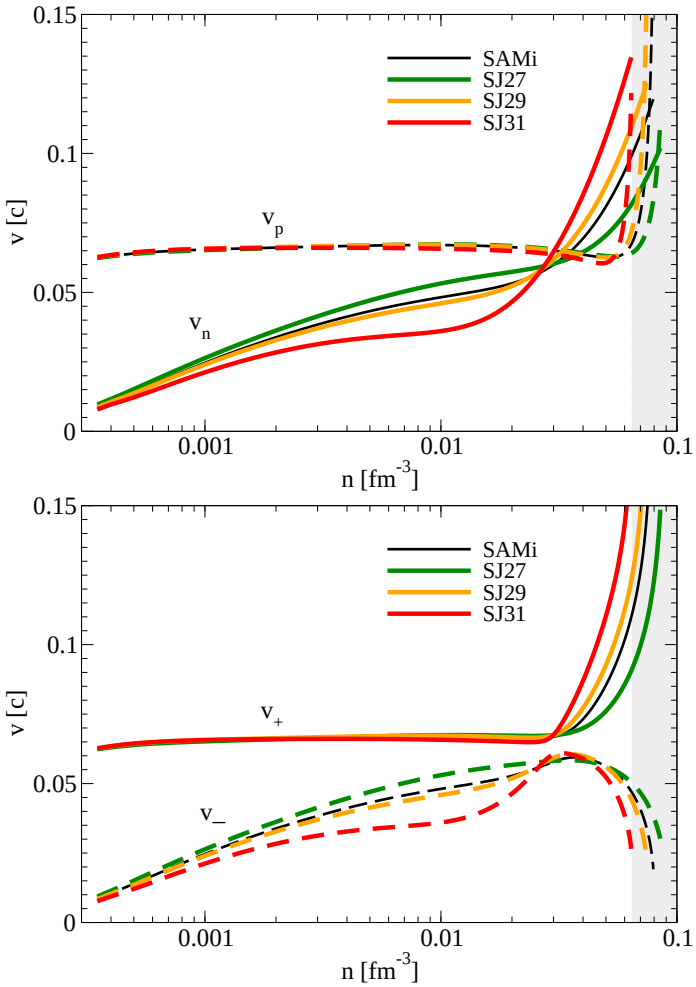

Figure 5.3: The decoupled modes velocities (up) and the coupled mode velocities (down) as a function of the total baryon number density of the cell n.

energy coefficient J, in fact we have a maximum variation of 3% among the parametrizations up to the minimum density value.

The superfluid mode has an increasing behaviour throughout all the inner crust; has smaller values for bigger J until 0.03 fm^{-3} and after that we see an inversion of the trend, in which SJ31 allows higher velocities with respect to SJ27 for the same density. The SJ27 has a smooth trend like the original SAMi and SJ29, and SJ31 also presents a hump around 0.01 fm^{-3}. As from the definition of v_n (3.25), the velocity of the superfluid mode is proportional to the product of E_{nn} and the neutron superfluid density. Since the neutron density is quite constant under a variation of J for all the densities considered, and given the definition of E_{nn} (3.13), we conclude that the behaviour of v_n is

dominated by the derivative of μ_n in function of n_n, or equally it depends on $\frac{\partial^2 \epsilon}{\partial {n_n}^2}$ which indicates the curvature of the internal energy density.

We know that, at lower densities, $v_- \approx v_n$ and $v_+ \approx v_p$. At 0.03 fm^{-3} we have a trend inversion for v_+: at lower densities the slightly major value of the coupled velocity mode corresponds to a minor value of J while over that density SJ31 has a bigger increase than SJ27. For v_- we see a peak with a maximum value around 0.035 and then a decrease behaviour, in particular SJ31 has a slightly higher peak value and a successive stronger decrease.

It is interesting to underline how the differences between v_-, v_n and v_p, v_+ have a weak dependence on the variation of J: for example the value $v_n - v_- \sim 0.1$ is obtained at 0.039 fm^{-3} for SJ27 and at 0.031 fm^{-3} for SJ31.

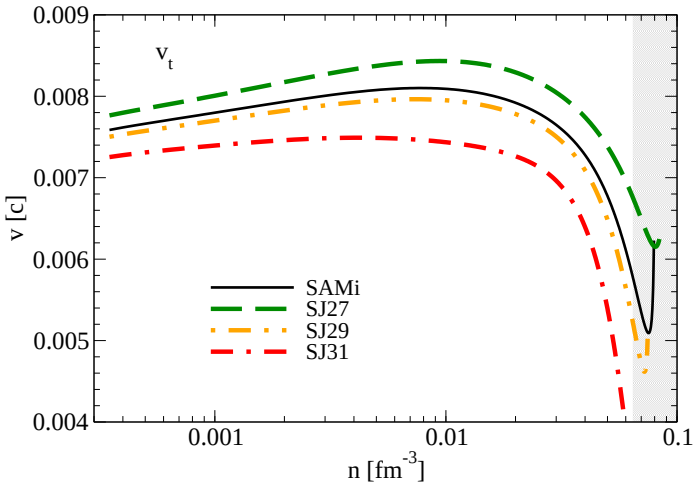

Figure 5.4: The transverse modes velocity as a function of the total baryon number density of the cell n.

The transverse mode velocity v_t shows a dependence on the value of the symmetry energy coefficient. At the upper limit of the inner crust the percentage difference among the parametrizations is less than 10% and increases with the density until the maximum difference reaches around 0.01 fm^{-3}. The velocity values also dimly increase with the density (the increment is more evident for SJ27) and reach a maximum around the density of maximum difference. After that, the velocity decreases for a few percentage (SJ29) or even for the half of the initial value (SJ31). The behaviour of the parametrization in Figure 5.4 shows that bigger values of J correspond to smaller transversal velocities. From (5.1), we think that the velocity dependence from J may be led by the Z term (following the discussion in subsection 4.3.2), because m^* has a fixed value and n_i, r_C have shown smaller variations compared to the variation of the proton number.

As for the static analysis, we notice how the differences between the original SAMi (with $J = 28$) and SJ27 and SJ29 are not similar, particularly for v_p (v_+) and v_t velocities: SJ29 has closer values than SJ27 with respect to SAMi.

Effective mass m*

The lattice mode velocity has an increasing value if calculated with smaller effective mass. The mean value goes from $0.068c$ for Sm6 to $0.058c$ for Sm85. As shown in Figure 5.5, the variation of the effective mass causes a translation of the function v_p, depending on the value of m^*, but does not cause any change in the form, in particular the velocity increases for smaller values of the effective mass. This trend can be explained by the fact that the velocity of

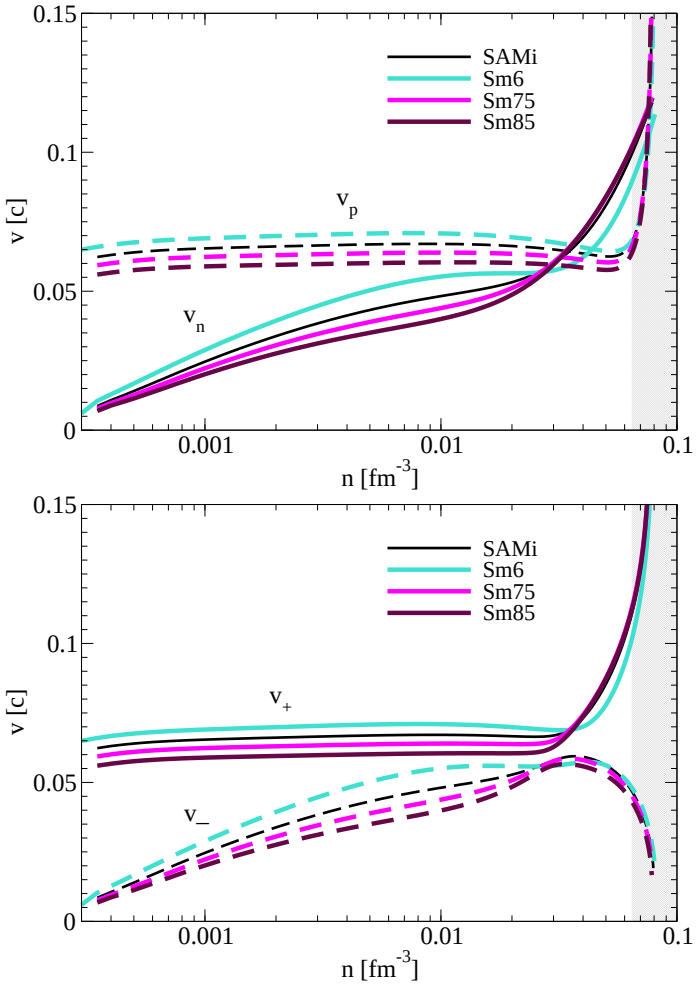

Figure 5.5: The decoupled modes velocities (up) and the coupled mode velocities (down) as a function of the total baryon number density of the cell n.

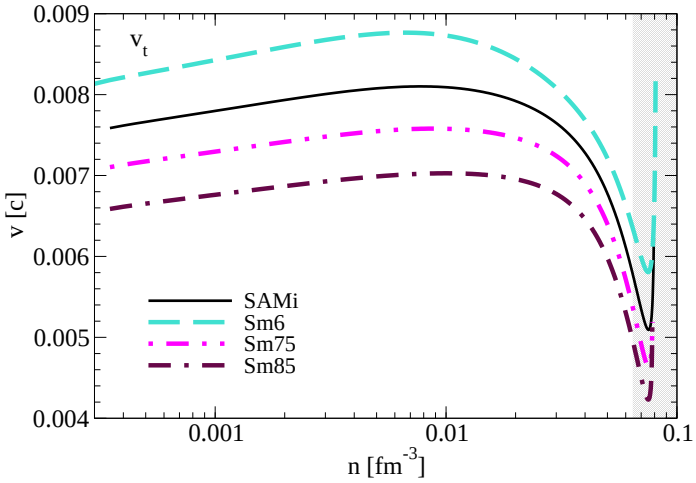

Figure 5.6: The transverse modes velocity as a function of the total baryon number density of the cell n.

the lattice mode depends on the value of the effective mass as $v_p \propto m^{*-1}$, since the other parameters which enter into the definition (3.26) do not vary during the sensitivity analysis of the m^* (as discussed in subsection 4.3.2). Close to the bottom layers of the inner crust we see how the different parametrizations show the same behaviour at the same density: this may be caused by the fact that the variation of the effective mass does not affect the physics which is leading the model and for high densities the presence of pasta phases or the transition with the outer core generate errors inside the algorithm.

For the superfluid mode velocity we see how the values of v_n increase for smaller m^* until 0.027 fm^{-3}, from which we observe that Sm85 has a stronger growth with respect to Sm6. Close to the neutron drip density, typical values are the order of $0.008c \pm 0.002c$. The bigger difference among the parametrizations happens at ~ 0.01 fm^{-3} with velocity of about $0.04c$ for Sm85 and $0.055c$ for Sm6, which also has a nearly flat trend until 0.03 fm^{-3}. The major value of the velocity due to smaller effective mass may be explained with the inertia of the particles: superfluid neutron with smaller masses may oscillate more easily and allow the wave to propagate more efficiently.

For lower densities, the first coupled mode velocity $v_+ \sim v_p$ is included in the range $0.055c - 0.075c$ for all the parametrizations. From 0.035 fm^{-3} the parametrization Sm6 allows smaller velocities while the other three are almost indistinguishable. The behaviour of the second coupled mode velocity $v_- \sim v_n$ is growing till ~ 0.035 fm^{-3} where the parametrizations decrease with a similar trend.

At the upper layers of the inner crust, the transversal mode velocity differs

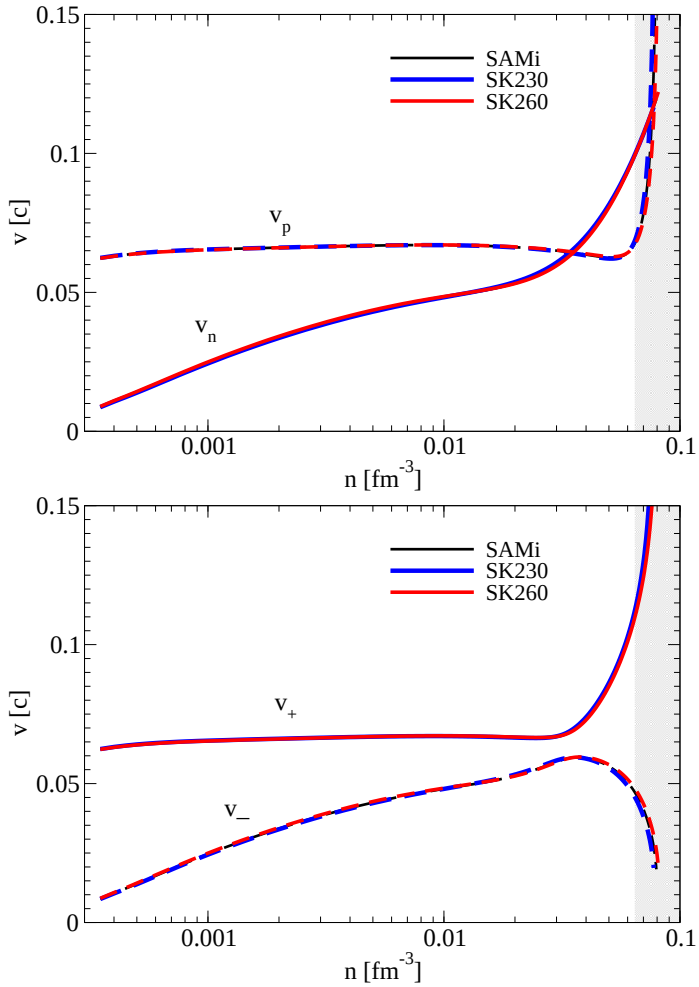

Figure 5.7: The decoupled modes velocities (up) and the coupled mode velocities (down) as a function of the total baryon number density of the cell n.

from $6.6 \times 10^{-3}c$ for Sm85 to $8.2 \times 10^{-3}c$ for Sm6; it increases with the density, following the same trend for all the Skyme used, till approx 0.01 fm^{-3} and then decreases. The minimum values of v_t, reached at half the saturation density, are at most two thirds of their initial values. As we see in Figure 5.6, an increment of the effective mass causes a diminish in transversal velocities. Following the discussion we make in subsection 4.3.2 and using (5.1), in this circumstance we may say that the trend of v_t is leads by $Zm^{*-1/2}$: both the quantities contribute to accentuate the differences among the parametrizations used.

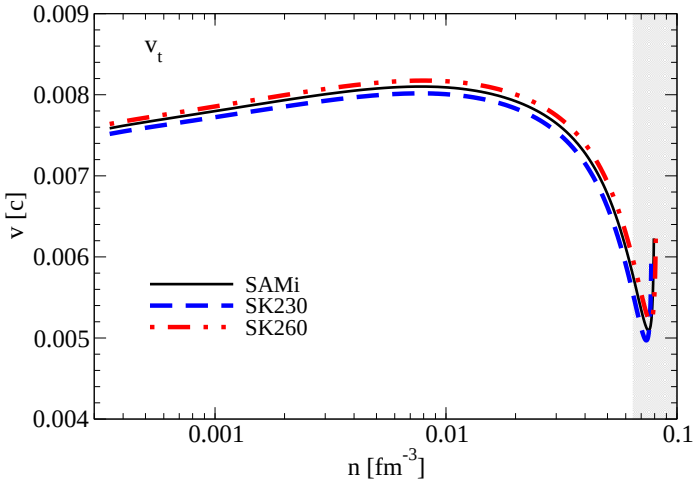

Figure 5.8: The transverse modes velocity as a function of the total baryon number density of the cell n.

Bulk modulus K

As we notice in subsection 4.3.2, the bulk modulus variation does not significantly affect the system neither causes any relevant effect. The differences between SK230 and SK260 are responsible of a percentage variation less than 2% for all the mode velocities.

5.4 Entrainment analysis

In this section we analyse how our results depend on the choice of the entrainment parameter α. In the next Chapter we will consider some values of the entrainment parameter which are close to the choice made by CPR (*46*) and we will discuss potential differences and similarities.

As discussed in (*46*), the presence of entrainment is expected to reduce the velocities of the transverse, the lattice phonon and the superfluid boson modes. In addition we know that entrainment induces a strong mixing between the longitudinal lattice mode and the superfluid mode, generating the coupled modes with velocities v_+, v_- and splitting these into a high velocity sound mode and a low velocity mode. The results may be relevant for the study of seismic activity correlated to giant flares in SGRs and binary NS mergers.

We use the SAMi interaction to show the effects due to entrainment for our model. We choose four values of the α (3.1) parameter: 0.0 (α_0), 0.3 (α_3), 0.6 (α_6), 0.9 (α_9) in order to cover a wide range of possibilities.

In Figure 5.9 the transverse mode trend changes depending on the value

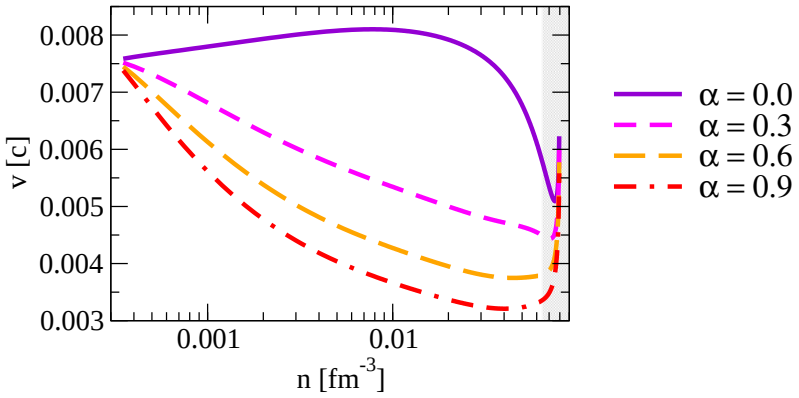

Figure 5.9: Transversal mode velocities (in c units) using SAMi Skyrme as a function of the total baryon number density of the cell n for some values of the entrainment parameter α.

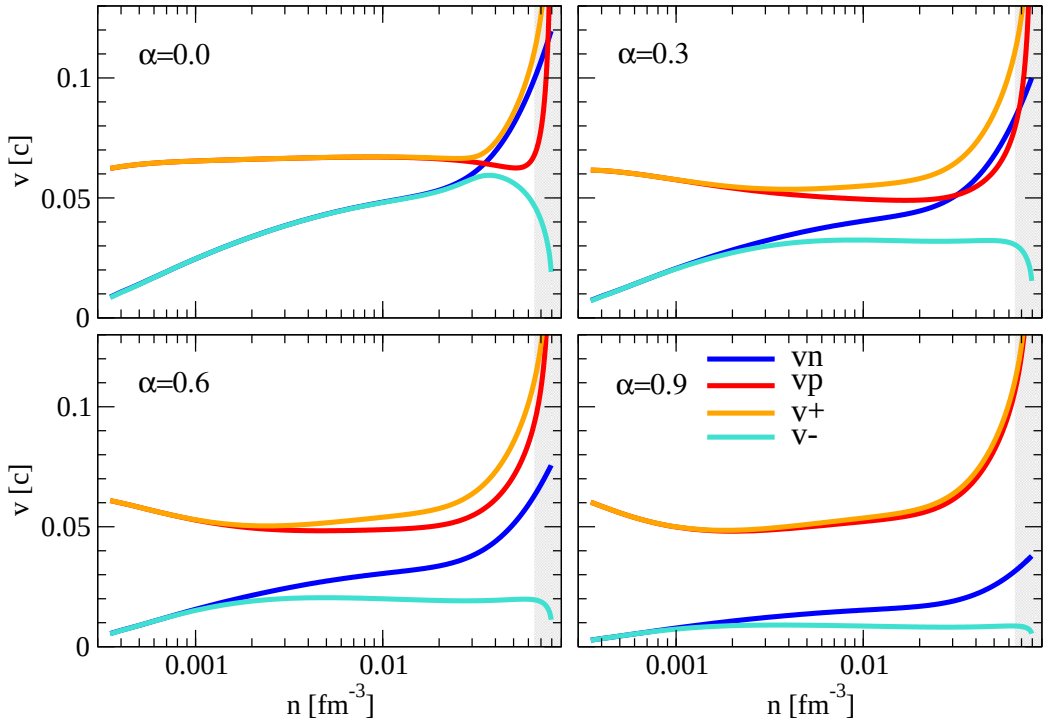

Figure 5.10: Longitudinal modes velocities (in c units) using SAMi Skyrme as a function of the total baryon number density of the cell n for some values of the entrainment parameter α.

of the entrainment parameter. When α_0 displays a maximum at 0.08 fm^{-3} of $0.008c$, the other values of α have a decreasing behaviour for all the inner crust and reach values from $0.0045c$ (α_3) to $0.0033c$ (α_9) close to the mantle transition density.

For the longitudinal modes in Figure 5.10, we see how the lattice and the superfluid react differently for a variation of α. The lattice mode velocity for α_0 has a quite flat behaviour around $0.065c$ for all the density range. When α assumes values different from zero, the behaviour of v_p changes and it shows a decreasing trend and successive increases till the bottom layers of the inner crust. The density at which we have the minimum of v_p diminishes when the entrainment parameter becomes bigger. For example when α_9 the minimum is around 0.002 fm^{-3} while when α_3 it happens at 0.016 fm^{-3}.

The trend of the superfluid mode is the same independently of α whereas the values of the velocities change remarkably. At 0.01 fm^{-3} we have $0.05c$ (α_0) and $0.015c$ (α_9) and there is a maximum value of $0.1c$ (α_0) and $0.032c$ (α_9) close to n_{edge}. The trend of v_n with increasing values of α is what we expect: since more neutrons are entrained, the superfluid gas is composed by less particles and the volume available does not change, so the density of superfluid neutrons n_n^s diminishes and the velocity of propagation of the sound wave decreases.

The values of v_+ are roughly included in the range $0.050c - 055c$ till approximate density 0.04 fm^{-3} for all the values of α. We observe how, for bigger entrainment, this coupled mode velocity is strongly similar to the lattice mode velocity. The coupled mode velocity v_- shows decreasing values when increasing the entrainment. At 0.037 fm^{-3} there is a maximum of $0.06c$ (α_0) and at the same density we calculate $0.032c$ (α_3) and $0.008c$ (α_9), about 8 times smaller than the original value.

As shows by CPR (*46*), the presence of entrainment reduces the velocity of the transverse modes, with halved values of v_t from densities above 0.005 fm^{-3}. Also lattice phonon mode and the superfluid boson mode are significantly reduced, around one third of the values calculated without entrainment from 0.01 fm^{-3}. Making a comparison between Figure 5.9 and Figure 5.10 with the analysis made in PR (*26*), we see how the entrainment causes similar modifications to the velocities, except for v_p and v_+ which are well splitted for higher entrainment in (*26*).

For the modified SAMi analysis (made with the parameters J, m^*, K) we calculate the effects of entrainment only for v_n, v_p and v_t, without considering the coupled mode velocities for simplicity.

Symmetry energy at saturation density J

The major difference underlined in Figure 5.11 is that, while the lattice mode velocity has a little dependence on J for α_0, we see how other values of the entrainment parameter cause a split in v_p based on the symmetry energy parameter value. In particular the split can be observed from density ~ 0.001 fm^{-3} because in the lower density region the velocities are quite overlapped. The minimum of SJ31 lays in the range $0.010 - 0.015$ fm^{-3} and its value is $\sim 0.04c$ independently of α.

The diversity among SJ31 and SJ27 from v_n tends to become smaller with increasing values of the entrainment parameter. As we discuss in general, the transverse velocities diminish for bigger α.

Effective mass m*

When the entrainment parameter is modified, the percentage variation between Sm6, Sm85 and SAMi in the lattice mode velocities v_p is not subject to drastic changes. It can be noticed however the trend of Sm85 to approach SAMi at lower densities as α increases.

For the superfluid mode velocity v_n we have, as for the symmetry energy coefficient, that the differences among the parametrizations seem to becoming null as the entrainment parameter enlarges.

A similar behaviour can be observed also for transverse mode velocities in which, for densities below 0.001 fm^{-3}, the values calculated for Sm85 are closer to SAMi than for higher densities when α increases.

Bulk modulus K

As already discussed in subsection 4.3.2, the variation of K does not cause any appreciable effect on the velocity, neither when the entrainment parameter is modified.

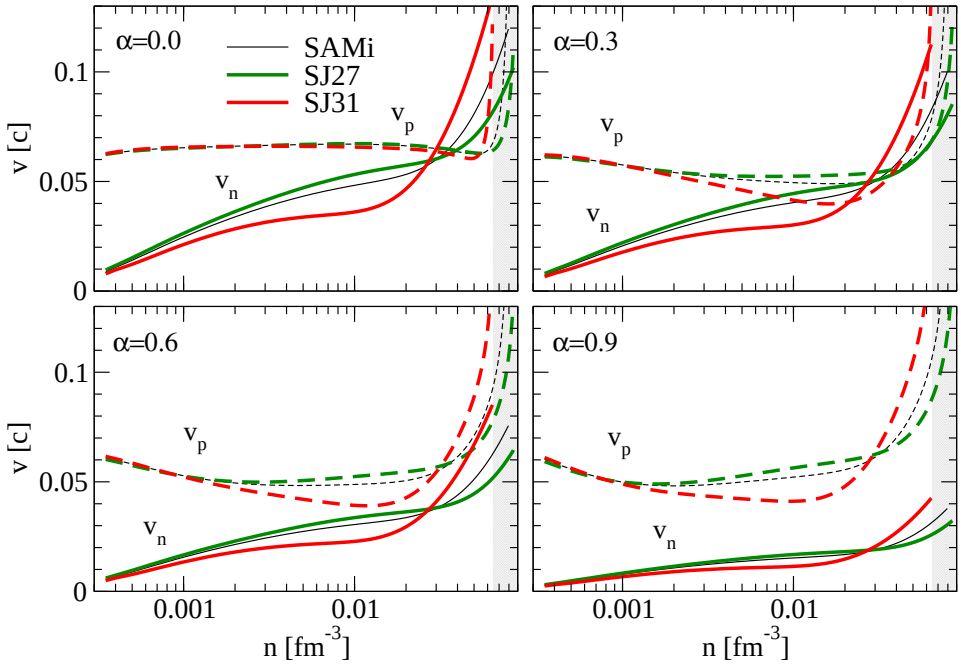

Figure 5.11: The longitudinal modes velocities v_p (dashed lines) and v_n (full line) in c units as a function of the total baryon number density of the cell n for some values of the entrainment parameter α.

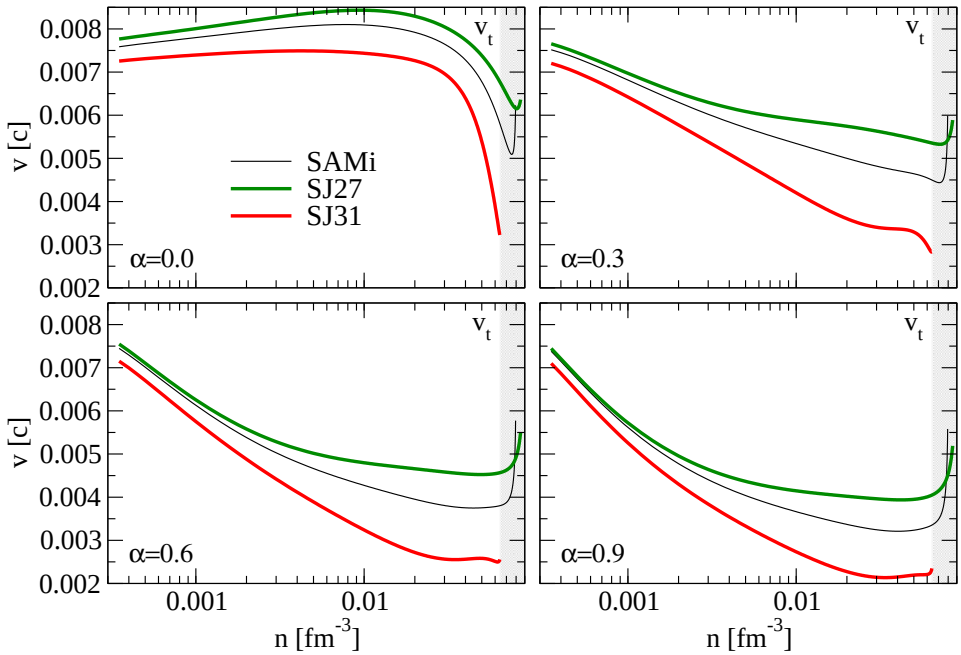

Figure 5.12: The transverse modes velocity v_t in c units as a function of the total baryon number density of the cell n for some values of the entrainment parameter α.

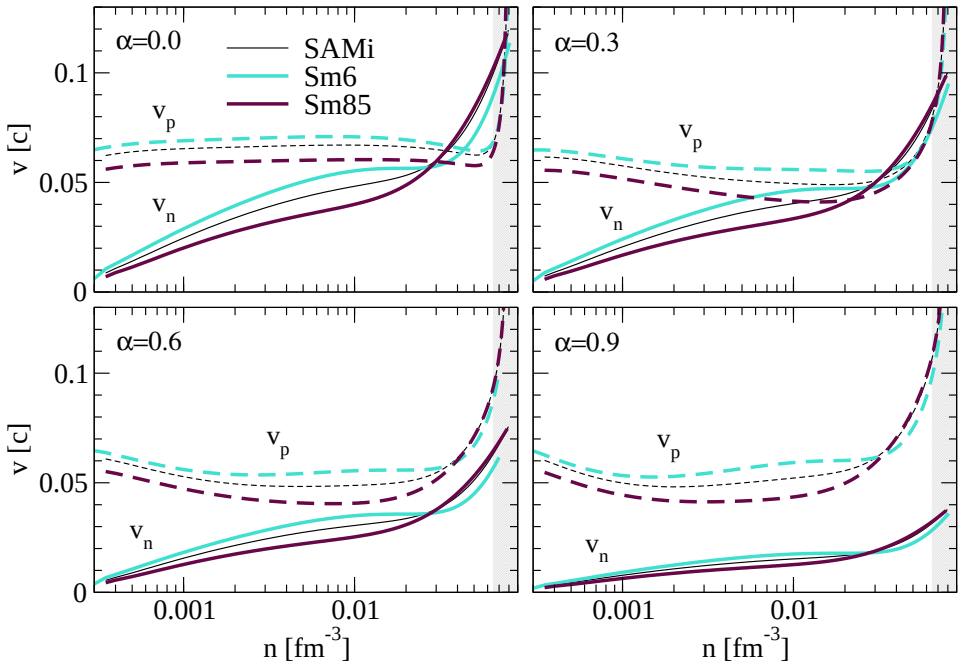

Figure 5.13: The longitudinal modes velocities v_p (dashed lines) and v_n (full line) in c units as a function of the total baryon number density of the cell n for some values of the entrainment parameter α.

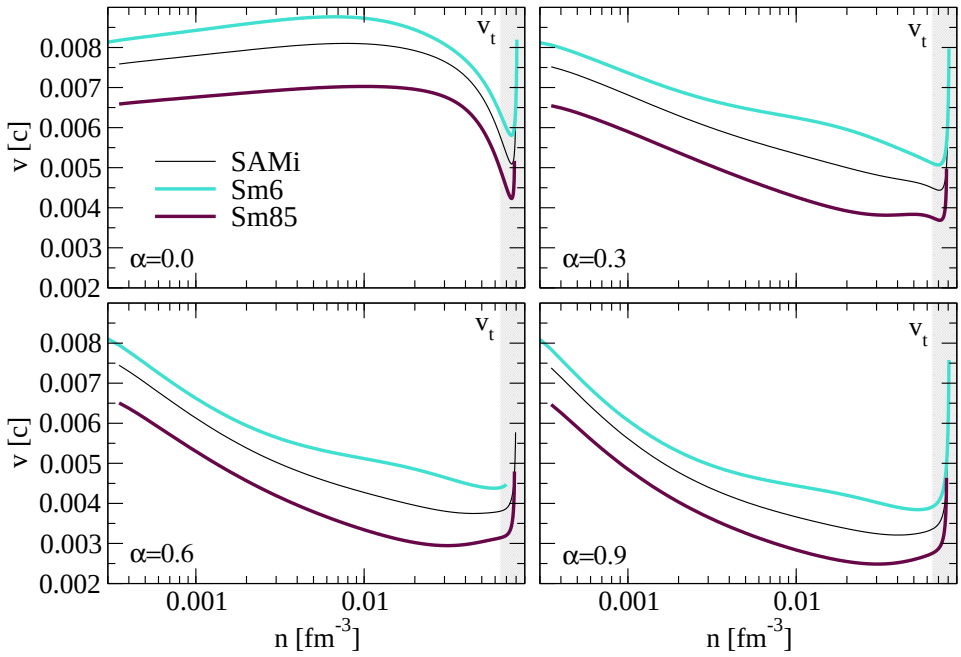

Figure 5.14: The transverse modes velocity v_t in c units as a function of the total baryon number density of the cell n for some values of the entrainment parameter α.

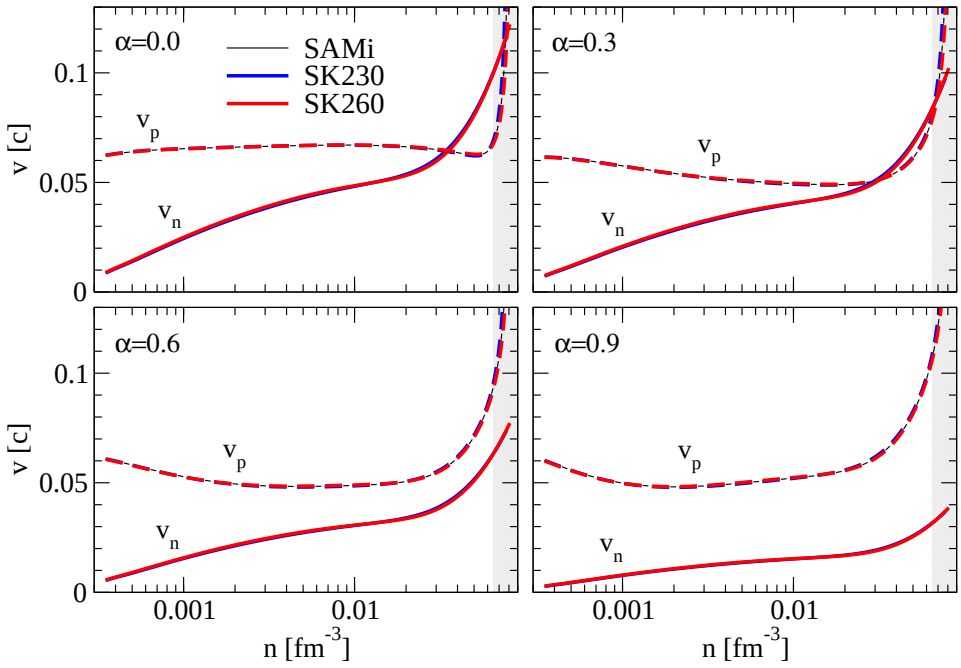

Figure 5.15: The longitudinal modes velocities v_p (dashed lines) and v_n (full line) in c units as a function of the total baryon number density of the cell n for some values of the entrainment parameter α.

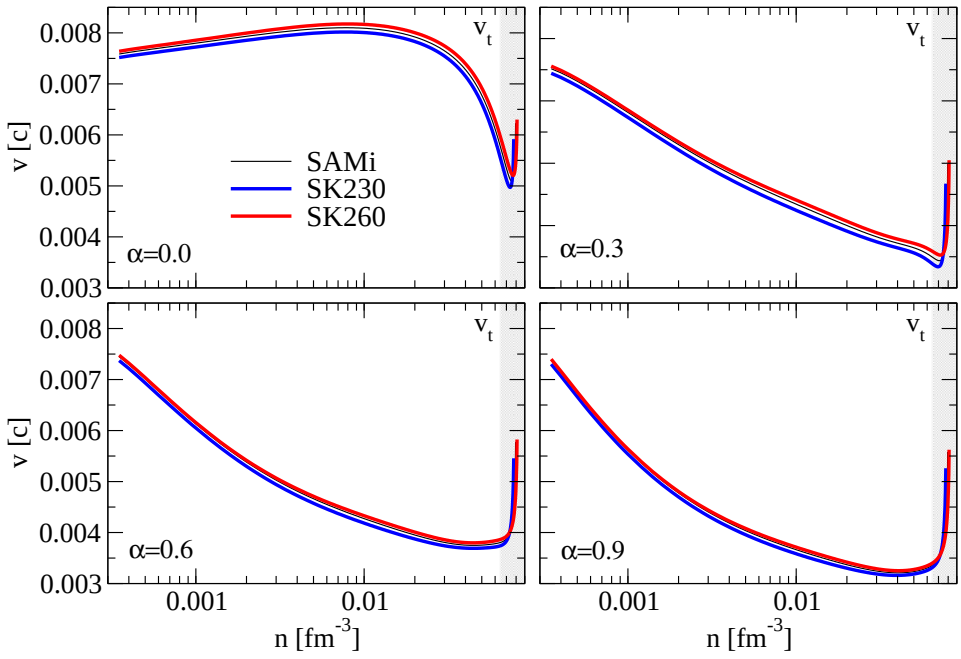

Figure 5.16: The transverse modes velocity v_t in c units as a function of the total baryon number density of the cell n for some values of the entrainment parameter α.

Chapter 6

Implications for the neutron star cooling

In this chapter we make an example of application of our results. Following the arguments in CPR (*46*), we calculate the heat capacity with its different contributions, in our framework, and we compare the results obtained with the ones from CPR.

6.1 Thermal evolution

The cooling process of a NS is a useful mechanism to achieve information about the evolution and the characteristics of the star. Since thermal evolution calculations are model dependent, a wide range of thermal histories is possible. The cooling models are sensitive for example to the adopted nuclear EoS, the neutron star mass, the magnetic field strength, the presence of superfluidity, the exotic degrees of freedom inside the core (*1*).

Not only the observations of isolated neutron star thermal evolution are of great interest, but also the behaviour of neutron stars in close binaries that undergo transient accretion outbursts are relevant. Observations of the temperatures of these NSs systems have been used to limit the neutrino emissivity of the neutron star core, which sensitively depends on the composition, and to show that long-term monitoring after accretion outbursts provides information on neutron star crust physics (*76*). How the neutron star cools during the relaxation period, after accretion ends, depends mainly on the thermal conductivity and heat capacity of the crust (*18*) including the pasta regions in the mantle (*77*).

The initial temperature of a newly born NS is $\sim 10^{11}$ K. The predominant cooling mechanism which acts on the NS immediately after its formation is the

neutrino emission: it is a very effective process with an initial cooling timescale of seconds. After about a day, the internal temperature drops by one order of magnitude while the crust stays hot. Because of the thermal gradient, the heat gradually flows inward through the conduction mechanism while the cooling wave propagates from the center to the surface. This is the so-called thermal relaxation epoch and lasts about 10-100 years, when the cooling wave has reached the surface. After this period the internal temperature has dropped to about $T = 10^9$ K: at this temperature the neutron star becomes entirely transparent to neutrinos and may be considered as isothermal. For $\sim 10^3 - 10^5$ years the neutrino cooling dominates the thermal evolution. They are overtaken by photon emission from the surface only when the internal temperature falls to $\sim 10^8$ K, with a corresponding surface temperature roughly two orders of magnitude smaller. The temperature of $T = 10^7$ K in reached after a longer period of time, more than 10^5 years. Then the NS continues to cool for millions of years.

6.2 Heat capacity contributions

The heat capacity C indicates the variation of the heat (energy) of a system as a result of a change in the temperature. It is useful to work in terms of the heat capacity per unit volume C_V, which is defined as

$$C_V = \frac{1}{V}\frac{\partial E}{\partial T}\bigg|_V .$$

In our framework V indicates the volume of the WS cell, E is the total internal energy and T is the temperature: the dimensions of C_V are erg K^{-1} fm^{-3}. In order to make a comparison with CPR, we decide to use their notation and we define the heat capacities C_V in units of k_B (which indicates the Boltzmann constant), so dimensions become fm^{-3}.

We need to define the heat capacity for the components present in our model. The heat capacity of an electron Fermi gas for which $k_B T \ll \mu_e$ is

$$C_V^e = \frac{1}{3}\frac{\mu_e^2}{(\hbar c)^3} k_B T \tag{6.1}$$

where the condition of low temperature is well verified for temperatures smaller than 10^{11} K.

The heat capacity of a collective excitation characterized by a dispersion relation $\omega = vk$ is given by

$$C_V^c m = \frac{3 n_p}{Z x_D^3} \int_0^{x_D} \frac{x^4 e^x}{(e^x - 1)^2} dx$$

in which $x_D = \Theta_D/T$. The quantity $\Theta_D = (\hbar/k_B)k_D v$ is the Debye temperature of the collective mode and $k_D = (6\pi^2 n_N)^{1/3}$ is the Debye wave number (we remember that $n_N = V_C^{-1}$ and V_C indicates the volume of the WS cell). In case of low temperature, so $T \ll \Theta_D$, the standard Debye result for vibrational excitations is

$$C_V^{cm} = \frac{2\pi^2}{15}\left(\frac{k_B T}{\hbar v}\right)^3 \tag{6.2}$$

where v indicates the generic velocity of the collective mode: we calculate the heat capacity of superfluid neutrons C_V^n and of the lattice C_V^p using v_n (3.25) and v_p (3.26), the mixed modes contributions $C_V^{\pm}$ with $v_{\pm}$ (3.28) and the transverse modes C_V^t with v_t (3.22). The minimum values calculated for Θ_D in our framework are $\sim 10^{10}$ K, so the condition of low temperature is respected for temperatures below this limit.

Considering all the contributions from the modes just mentioned, we can write the total heat capacity of the whole crust as

$$C_V \simeq C_V^e + \frac{2\pi^2}{15}\left(\frac{k_B T}{\hbar \bar{v}}\right)^3 \tag{6.3}$$

with

$$\frac{1}{\bar{v}^3} = \frac{2}{v_t^3} + \frac{1}{v_-^3} + \frac{1}{v_+^3}.$$

6.3 Temperature analysis

We calculate the heat capacity of the collective modes components and of the electron Fermi gas with the BSk14 Skyrme interaction since it is the same choice made by CPR. We study three cases characterized by different temperatures (as made in (*46*)) as they represent three moments in the evolution of a neutron star.

- $T = 10^9$ K ≈ 0.086 MeV is the temperature reached by young NSs once became isothermal. This case does not have observable confirmations because of the radiation emission of the newly formed nebula, which hides the presence of the young NS;

- $T = 10^8$ K $\approx 8.6 \times 10^{-3}$ MeV is considered an average temperature for NS. This is a very interesting case in which different cooling processes coexist;

- $T = 10^7$ K $\approx 8.6 \times 10^{-4}$ MeV is the temperature of very old NSs.

We also vary the entrainment parameter α (3.1) because we want to discuss how the entrainment modifies the heat capacity as a function of the temperature and how it plays a role in determining the leading contributions. We calculate the values of the entrainment parameter starting from the effective neutron mass defined in (*30*, *60*) as

$$m_n^* = m_n \frac{n_n^f}{n_n^c}$$

where n_n^f indicates "free" neutrons (i.e. dripped from nuclei) and n_n^c are the conduction neutrons (in analogy with the conduction electrons in ordinary metals). In our framework they are labeled as $n_n^f = n_o$ and $n_n^c = n_n^s = (1-\alpha)n_o$, so we can express the entrainment parameter as

$$\alpha = \frac{m_n^*/m_n - 1}{m_n^*/m_n}. \tag{6.4}$$

The effective mass in (6.4) is a function of the density and then in CPR model the entrainment is not constant for the whole crust; in particular, as underlined by the numerical values in (*60*), entrainment is very strong in the intermediate region of the inner crust ($n \sim 0.02-0.04$ fm^{-3}) where only $\sim 10\%$ of total dripped neutrons are superfluid and the remaining are entrained, while in the other regions the fraction n_n^c/n_n^f grows up to $\sim 80\%$. In our model we take α as a fixed parameter for all the densities studied. We assign to α the values 0.7778 ($\alpha_{0.8}$) and 0.9265 ($\alpha_{0.9}$), which correspond respectively to $m^*/m = 4.5$, a reasonable value for low and high densities (~ 0.001 fm^{-3} and ~ 0.05 fm^{-3}) and $m^*/m = 13.6$ that is the maximum value calculated in (*60*), suitable for intermediate densities. We also consider the limit case $\alpha = 0$, i.e. $m^*/m = 1$.

Cold neutron stars

For old NSs with temperatures of 10^7 K the total heat capacity is dominated by the electron Fermi gas and, as shown in Figure 6.1, this term is independent from the value of the entrainment parameter. For values of α close to unity, however, we see how at 0.003 fm^{-3} the heat capacity of the lower coupled mode may contribute to the total heat capacity. Close to neutron drip density, the logarithm of total heat capacity has value ~ -7.55 for α_0 and $\alpha_{0.8}$ (-7.38 for $\alpha_{0.9}$) and grows to -6.7 at the beginning of the mantle. Calculating the values of C_V at n_{drip} for α_0 and $\alpha_{0.9}$ we have that the percentage difference among them is about 50%, but since involves a small range of density (till 0.006 fm^{-3}) it does not influence the main trend.

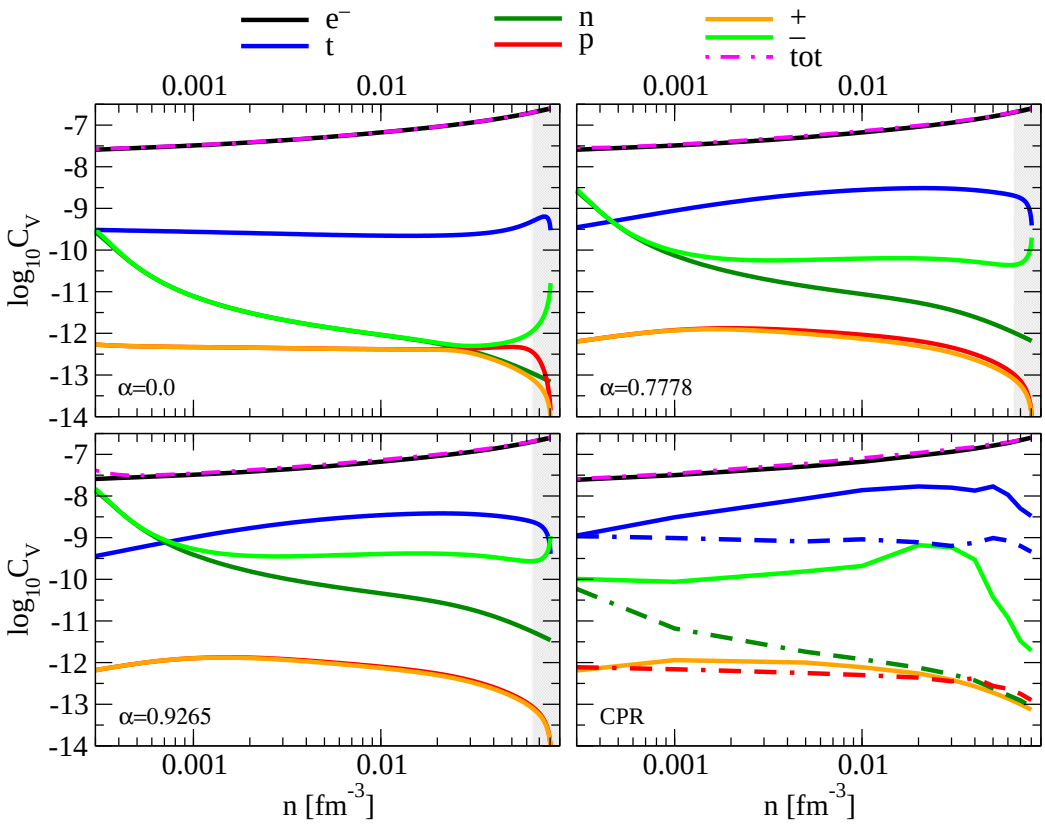

Figure 6.1: The heat capacity contributions and the total heat capacity at $T = 10^7$ K in function of the total baryon number density of the cell n calculated with the BSk14 interaction. They are calculated for different values of the entrainment parameter α. The right-down panel shows the results obtained using the data from CPR (*46*). The labels indicate the superfluid boson (n), the lattice phonon (p), the mixing modes (±), the transverse modes (t), the electron Fermi gas (e) and the total contribution (tot). The dashed-dotted lines of t, n, p in CPR indicate the results without entrainment.

As long as α increases, the contribution due to the transverse mode grows up to one order of magnitude and the heat capacity of low mixed mode starts from -9.51 (α_0) and ~ -7.6 ($\alpha_{0.9}$) at n_{drip} and varies up to -12.3 (α_0) and -9.45 ($\alpha_{0.9}$) in the inner crust density range. Values of $\log_{10} C_V^n$ are similar to $\log_{10} C_V^-$ at low densities and then the difference increases with n. The heat capacity of the high coupled mode with v_+ is completely negligible.

The results obtained are coherent with the ones in CPR's work, in particular we notice how the trend of the electron contribution is similar to our results. Even if the transverse mode contribution without entrainment has a similar flat behaviour, the values close to the neutron drip density are ~ 3 times bigger compared to our values of C_V^t. This effect is due to the different values of the

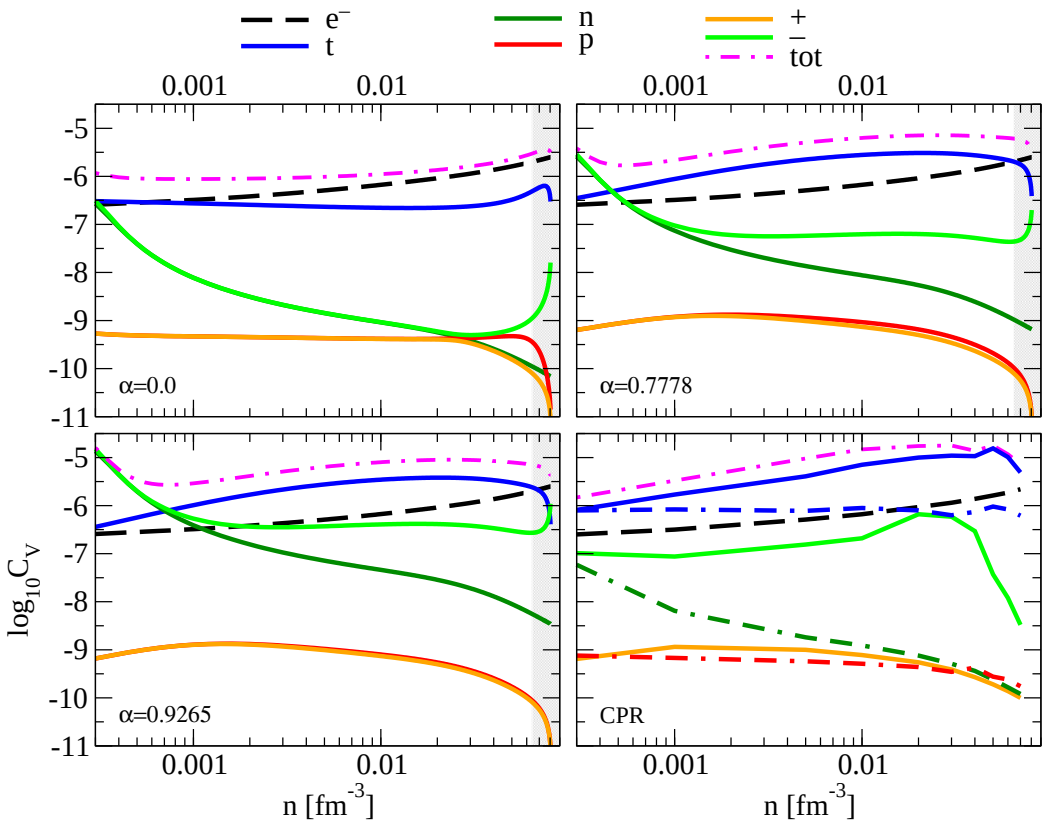

Figure 6.2: Same as in Figure 6.1 with $T = 10^8$ K.

v_t, as shown in section 5.2. At the same density, also the low coupled modes are different: the smallest beginning value calculated for our model is -9.51 at n_{drip} for α_0, while for CPR we have -9.99. Indeed the trends of the high coupled modes are very similar.

Average neutron stars

In the case $T = 10^8$ K we see how the total C_V changes as a function of the entrainment parameter. For α_0 the dominant contribution at high densities above 0.01 fm^{-3} is given by $\log_{10} C_V^e$, while at lower densities we have to take into account also the transverse phonons, since their contribution has the same magnitude of the electron term, as for $\log_{10} C_V^-$ at n_{drip}. When α increases, close to the neutron drip density and till $2n_{drip}$ the low coupled mode (and equally the superfluid mode) gives the largest contribution. It reaches -5.54 ($\alpha_{0.8}$) and -4.82 ($\alpha_{0.9}$) at n_{drip}, around 20% and 30% bigger values than $\log_{10} C_V^e$ and $\log_{10} C_V^t$ (~ -6.5) at the same density. Then, for the remaining densities, C_V^t leads the values of the global heat capacity of the inner crust

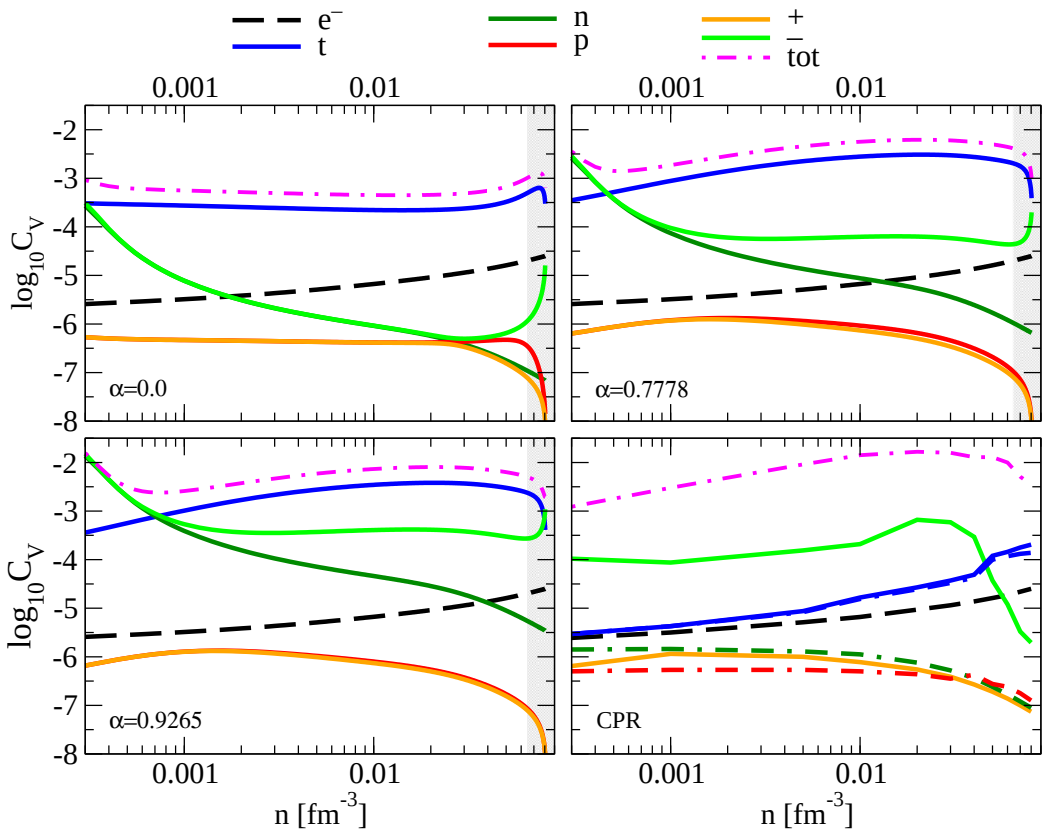

Figure 6.3: Same as in Figure 6.1 with $T = 10^9$ K.

by a factor 5 over C_V^e and over C_V^- for $\alpha_{0.9}$; the contributions of electrons and low coupled mode phonons have to be considered anyway. As for the previous case, the heat capacities of the lattice phonons and the high coupled mode are three orders of magnitude smaller than the total C_V, so they are neglected.

In the work of CPR we see that, without the effects of entrainment, the leading contributions are the transverse phonons for densities below ~ 0.015 fm^{-3} and the electrons for higher densities. If the entrainment is taken into account, the C_V^t term becomes dominant for the whole inner crust. The difference with our model for α_0 is caused by the values of v_t as told previously: a variation the order of $0.001c$ for transverse velocity generates a C_V^t contribution in our model 3 times smaller than the one calculated by CPR. As noticed in the previous section, the values of $\log_{10} C_V^-$ al low densities are smaller than the ones we calculated, as at n_{drip} we have -6.5 in the case of α_0 whereas CPR has -7 at the same density.

In conclusion, the results concerning the total C_V contributions at $T = 10^8$ K are model dependent.

Hot neutron stars

When $T = 10^9$ K, the dominant contribution to the total heat capacity is given by the transverse phonons through the majority of the inner crust for all the entrainment parameters. However, at the neutron drip density in the case of α_0 the contribution due to C_V^- has the same order of magnitude of C_V^t, so the two contributions have equal importance. For $\alpha_{0.8}$, $\alpha_{0,9}$ and below 0.001 fm^{-3}, the low coupled mode term is even more relevant than the transverse term; in fact at n_{drip} we have $\log_{10} C_V^t \sim -3.45$ while $\log_{10} C_V^-$ is -2.54 ($\alpha_{0.8}$) and -1.82 ($\alpha_{0,9}$), which means that C_V^- is respectively ~ 8 and ~ 40 times bigger than the transverse mode term.

The electron contribution is two orders of magnitude smaller than the transverse term and its values have small effect on the total C_V. The high coupled mode term is few orders of magnitude smaller than the transverse and the electron contributions, so it does not affect the global heat capacity.

The main difference with respect to our model is that for CPR the leading contribution to the total heat capacity is given by the low coupled mode, since $\log_{10} C_V^-$ is more than ore order of magnitude bigger than $\log_{10} C_V^t$ close to the neutron drip, and has a quite flat behaviour till 0.01 fm^{-3}. For high densities however it diminishes by a factor 100 and the transverse mode contribution becomes relevant. All the remaining terms are too small and their effect can be neglected. As a matter of fact, the values of $\log_{10} C_V^-$ in Figure 6.3 calculated from the values of v_- given in (*46*) and using (6.2) are not similar to those which are displayed in Figure 6 in (*46*).

6.3.1 Total heat capacity comparison

As a final discussion, to show the role of entrainment and the differences due to the choice of the model, we make a comparison between the logarithm of the total heat capacity of the inner crust calculated with the data from CPR and with our resulting values. Since we have underlined the fact that the effective mass in CPR model is density-dependent while in our model is a constant parameter, we expect that at different densities we may find some analogies between the total C_V^{CPR} in CPR and different values of C_V^α in our work. To be precise, for densities below ~ 0.001 fm^{-3} and above ~ 0.05 fm^{-3} we may see a good agreement between C_V^{CPR} and $C_V^{\alpha_0}$ while for intermediate densities the most similar curve may be $C_V^{\alpha_{0.9}}$.

What we observe in Figure 6.5 and Figure 6.6 is that, meanwhile at intermediate densities the values of $C_V^{\alpha_{0.9}}$ are the closest to the ones from CPR, at low and high densities we can not see a clear agreement with $C_V^{\alpha_0}$. These effects may be caused by the role of different leading contributions in generat-

ing the total C_V, as we have discussed previously. In Figure 6.4 however we observe a better agreement close to the neutron drip density and to the mantle transition.

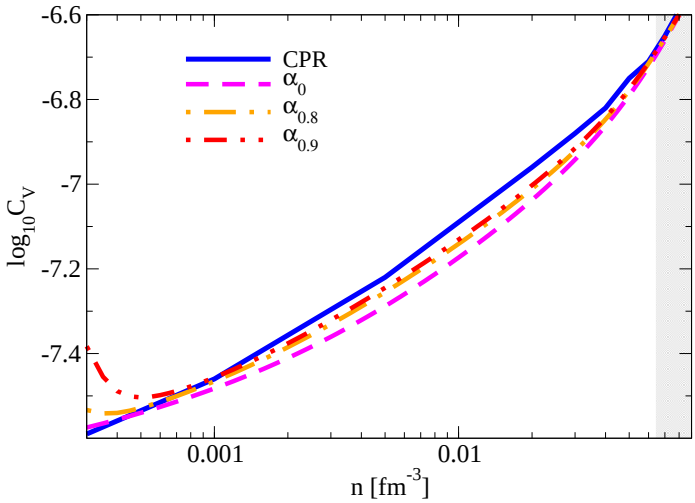

Figure 6.4: Comparison between the logarithm of the total heat capacity C_V for the inner crust calculated by CPR (*46*) and by our model for the three entrainment parameters α_0, $\alpha_{0.8}$, $\alpha_{0.9}$ at $T = 10^7$ K as a function of the total baryon number density n.

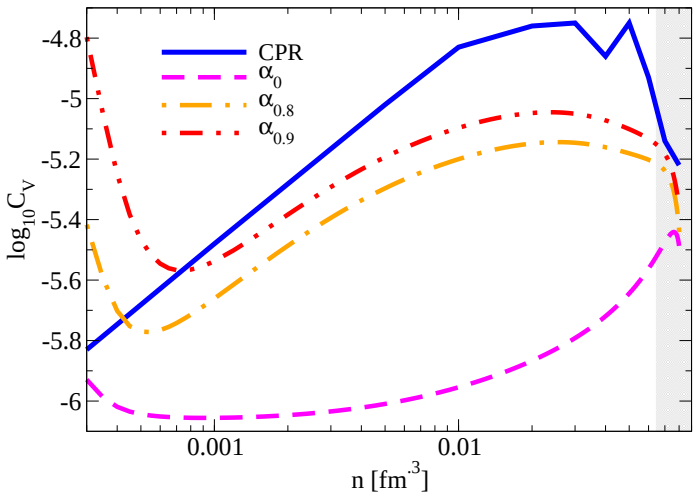

Figure 6.5: Same as in Figure 6.4 with $T = 10^8$ K.

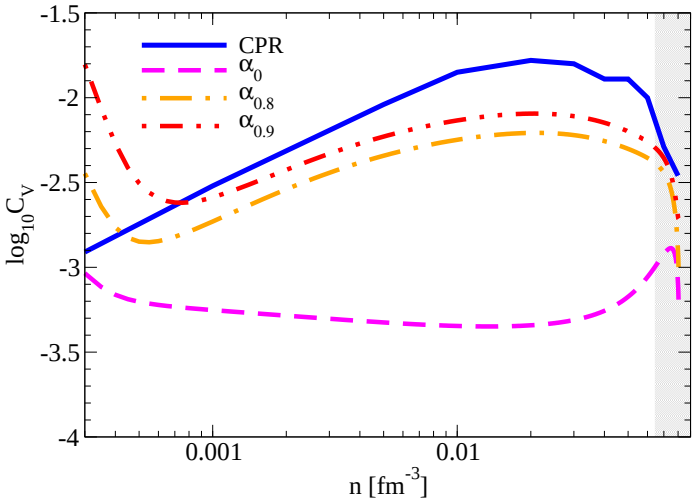

Figure 6.6: Same as in Figure 6.4 with $T = 10^9$ K.

Conclusions

In this thesis we have developed a model to describe the composition of the matter in the crust of neutron stars, with particular emphasis on the inner crust. The model has allowed us to calculate the velocities of the collective modes and to evaluate how the variations of some physical parameters can affect the properties of the crust in our predictions.

The main components in our model are the electron Fermi gas, the neutron rich nuclei forming a bcc lattice and the superfluid gas of dripped neutrons. We use the Wigner-Seitz approximation (which means that the physical unit cell of the lattice is replaced by one of equal volume and spherical shape) in order to obtain the composition and the structure of the cells with respect to mechanical and chemical equilibrium.

We choose the compressible liquid drop model to describe the energy of nuclei, various equations of state to describe the nucleons and the free Fermi gas energy for electrons. Since other different approaches exist (for example the extended Thomas-Fermi), from the comparison made with a few more works, we notice that large discrepances may appear. The results not only depend on the choice of the model as we expect, but also on the interaction implemented to describe the bulk energy term, as we verified for our model by using four Skyrme parametrizations.

When varying the values of the nuclear incompressibility K, the effective mass m^* and the symmetry energy coefficient J we discover how the composition of the cell, which means in particular the total baryon number per cell and the number of protons and baryons inside nuclei, has a stronger dependence on the symmetry energy coefficient than on the effective mass. The variations of the bulk modulus do not generate any significant modification. So the composition of the inner crust is sensitive to J and m^* and it is almost independent from K.

Regarding the collective modes, the effective mass causes the most notable changes in determining the superfluid bosons, the lattice phonons and the coupled modes velocities, as well as the transversal velocities. A variation of the symmetry energy coefficient influences the superfluid mode velocity and the

transverse velocities but is not significant for the lattice phonons till densities close to the bottom layers of the inner crust. As we expected, the bulk modulus does not cause any relevant variation.

Entrainment plays a very important role in characterizing the configuration of the WS cell and consequently in determining the velocities of the collective modes and the resulting heat capacities. The transverse velocities are reduced by a maximum factor of 3 for densities close to the mantle, as the effect of entrainment increases with the density. Longitudinal modes are affected too: the superfluid mode velocities become smaller as entrainment increases and the differences caused by the variation of the quantities J and m^* tend to be negligible, while the lattice mode velocities do not experience great variations. In particular the comparative analysis we have made, using four Skyrme interaction in our framework and the results from other works, both considering and neglection entrainment, allow us to distinguish between the errors due to a variation of the interaction choosen from the ones due to the choice of the model.

Concerning the heat capacities, the results obtained for cold ($\sim 10^7$ K) and hot ($\sim 10^9$ K) neutron stars are coherent with the expectations. For average temperatures ($\sim 10^8$ K) however the role of entrainment is essential in determining the leading contributions, since the role of electrons diminishes and the importance of transverse mode increases the total heat capacity as the entrainment parameter takes values different from zero.

Furthermore, a minor contribution but anyway essential in evaluating the total heat capacity is given by the low coupled modes. If the contributions due to collective modes are neglected, the calculations of the total heat capacities are not reliable and may not correspond to observations. So the study of collective modes is crucial to propose reasonable models to describe the cooling of neutron stars. The results of such studies have been shown to be highly model-dependent. We have seen that is of utmost importance to identify the effects caused by the choice of the model and those caused by the interaction.

Appendix A

Lattimer & Swesty model

We briefly write the expression of the bulk energy terms based on the model of Lattimer and Swesty (*38*).

They reproduce the Skyrme energy with an approximated potential, characterised by a formula which includes the kinetic energy term, an energy potential term, that depends on density to account in an effective way for many-body effects, and other corrections.

A.1 Bulk energy term

$$\begin{aligned}\tilde{e}_{bulk}(n,Y) =& \frac{1}{n}\Bigg[\frac{3}{5}\frac{\hbar^2}{2m^*}(3\pi^2)^{2/3} n^{5/3}\left[Y^{5/3}+(1-Y)^{5/3}\right]+ \\ &+\left(a+4bY(1-Y)\right)n^2 + cn^{1+\delta} - Yn\Delta\Bigg].\end{aligned} \tag{A.1}$$

We construct this formula starting from symmetric nuclear matter (SNM): kinetic energy of the first term indicates the non relativistic kinetic energy of a non interacting Fermi gas made of two species, neutrons and protons, at zero temperature and the second term $\sim a$ describes the nucleon-nucleon interaction by a local two-body potential. In case of asymmetric nuclear matter (ANM), we need a term $\sim b$ describing the proton-neutron (two body) interaction and a further term $\sim \Delta$ which considers the difference between proton and neutron masses because this bulk binding energy is referred to the neutron mass. Finally, the term $\sim c$ represents a many-body interaction, and its exponent δ determines to a large extent K_∞. The variable m^* indicates the effective mass.

We want to relate these two expressions of bulk energy by expressing the

parameters used in (A.1) as functions of the experimental quantities in (2.6)

$$E_c = \frac{3}{5}\frac{\hbar^2}{2m}\left(\frac{3\pi^2}{2}n_\infty\right)^{2/3} \quad \text{[MeV]} \tag{A.2a}$$

$$\delta = \frac{K_\infty + 2E_c\dfrac{m}{m^*}}{3E_c\dfrac{m}{m^*} + 9E_\infty} \quad \text{[MeV fm}^3\text{]} \tag{A.2b}$$

$$b = \frac{1}{n_\infty}\left[E_c\frac{m}{m^*}(2^{2/3}-1) - J\right] \quad \text{[MeV fm}^3\text{]} \tag{A.2c}$$

$$a = \frac{1}{(1-\delta)n_\infty}\left(\delta\left[E_c\frac{m}{m^*} + E_\infty\right] - \frac{2}{3}E_c\frac{m}{m^*}\right) - b \quad \text{[MeV fm}^3\text{]} \tag{A.2d}$$

$$c = \frac{K_\infty + 2E_c\dfrac{m}{m^*}}{9\delta(\delta-1){n_\infty}^\delta} \quad \text{[MeV fm}^6\text{]} \tag{A.2e}$$

$$\Delta = (m_n - m_p)c^2 \quad \text{[MeV]}. \tag{A.2f}$$

A.2 Energy contributions

The expressions of the energy for the superfluid neutrons and the nuclear matter in our model are

neutron gas outside nuclei

$$e_o = (1-u)\left[\frac{3}{5}\frac{\hbar^2}{2m^*}\left(3\pi^2\right)^{2/3}{n_o}^{2/3} + an_o + c{n_o}^\delta\right]; \tag{A.3}$$

nucleons inside nuclei, both neutrons and protons

$$\begin{aligned} e_N =& u\left(\frac{3}{5}\frac{\hbar^2}{2m^*}\left(3\pi^2\right)^{2/3}{n_i}^{2/3}\left[{Y_i}^{5/3} + (1-Y_i)^{5/3}\right] + \right. \\ &\left. + (a + 4bY_i(1-Y_i))n_i + c{n_i}^\delta - Y_i\Delta\right) + \\ &+ u\left(\frac{3}{r_N n_i}\sigma_{LS}(Y_i, T=0) + \frac{4\pi}{5}e^2{Y_i}^2{r_N}^2 n_i D(u)\right). \end{aligned} \tag{A.4}$$

For the sake of simplicity, we define

$$X = \frac{3}{10}\frac{\hbar^2}{m}(3\pi^2)^{2/3}\frac{m}{m^*} \simeq 119.073\frac{m}{m^*} \quad \text{[MeV fm}^2\text{]}.$$

We write σ_{LS} as

$$\sigma_{LS}(Y_i) = \sigma_s \frac{16 + Q}{{Y_i}^{-3} + Q + (1 - Y_i)^{-3}} \tag{A.5}$$

where we define (*38*)

$$Q = \frac{384\pi\sigma_s}{S_s}\left(\frac{3}{4\pi n_\infty}\right)^{2/3} - 16 \tag{A.6}$$

and substituting the values of σ_s, S_s, n_∞ available in the paper, we obtain $Q = 24.3986$.

Still for simplicity, we divided the energies into several terms, giving us

$$e_o = (1 - u)\left[X {n_o}^{2/3} + a n_o + c {n_o}^{\delta}\right] \tag{A.7}$$

$$e_{kin} = u X {n_i}^{2/3}\left[Y_i^{5/3} + (1 - Y_i)^{5/3}\right] \tag{A.8}$$

$$e_{vol} = u\Big(\left[a + 4bY_i\left(1 - Y_i\right)\right] n_i + c {n_i}^{\delta} - Y_i \Delta\Big) \tag{A.9}$$

$$e_s = \frac{3u}{r_N n_i}\sigma \tag{A.10}$$

$$e_C = \frac{4\pi}{5} q^2 {Y_i}^2 {r_N}^2 n_i u D. \tag{A.11}$$

Appendix B

Energy dimensions

As we see in subsection 2.1.5, we give the total energy contributions for the inner crust matter. We now show explicitly the correct dimensions of all these terms to allow us to sum them.

Since the electron gas energy is evaluated for leptons, we multiply the Fermi gas energy by the term $Y_e = \frac{n_e}{n}$ to obtain an energy per baryon

$$e_{Fermi} Y_e = e_e \to \frac{E}{Z}\frac{Z}{A} = \frac{E}{A}. \tag{B.1}$$

The bulk energy has the dimension of a free energy per particle of the species we are considering. In the case of the neutron gas energy outside nuclei we have

$$\tilde{e}_{bulk}(n_o) = \tilde{e}_{bulk,o} \to \frac{E}{N_o} \tag{B.2}$$

and for the bulk energy for protons and neutrons inside nuclei

$$\tilde{e}_{bulk}(n_i, Y_i) = \tilde{e}_{bulk,i} \to \frac{E}{A_i}. \tag{B.3}$$

First we consider the neutron gas. To obtain the final expression for the energy per baryon, we have to consider the fraction of volume $1 - u$ occupied by the gas and the ratio of the density of outer neutrons respect of the total density.. We multiply these terms to gain

$$(1-u)\tilde{e}_{bulk,o}\frac{n_o}{n} = e_o\frac{n_o}{n} \to \frac{V_o}{V_C}\frac{E}{N_o}\frac{N_o}{V_o}\frac{V_c}{A} = \frac{E}{A}. \tag{B.4}$$

For the nuclear matter, we can add together the bulk energy inside nuclei, the surface and the Coulomb energies, because all these terms are energy per baryon inside nuclei. We multiply the bulk term by the volume fraction u and the ratio of density inside nuclei rescpect of the total density to obtain

$$u(\tilde{e}_{bulk,i} + \tilde{e}_s + \tilde{e}_C)\frac{n_i}{n} = e_N \frac{n_i}{n} \rightarrow \frac{V_N}{V_C}\frac{E}{A_i}\frac{A_i}{V_N}\frac{V_C}{A} = \frac{E}{A}. \tag{B.5}$$

Appendix C

Compton and de Broglie wavelength

We are going to show how the different components of a neutron star matter (electrons, protons and nuclei) can be treated. We define the thermal de Broglie wavelength λ_T as follows

$$\lambda_T = \frac{h}{p} \tag{C.1}$$

where p is the momentum of the particle, and the Compton wavelength as

$$\lambda_C = \frac{h}{mc}. \tag{C.2}$$

We evaluate the typical length scale of our system ℓ, the mean distance among particles, given by the definition of unit volume

$$V = \frac{4}{3}\pi n \ell^3 = 1. \tag{C.3}$$

In an ideal gas, the length λ_T establishes the nature of the particles if compared with ℓ. If $\ell \gg \lambda_T$, the system will be quantal; if $\ell \ll \lambda_T$, the system will be degenerate. Similarly, the comparison between λ_C and ℓ indicates the degree of relativity of the system. If $\ell \gg \lambda_C$, the system will be non relativistic; if $\ell \ll \lambda_C$, the system will be ultra relativistic.

We verify if the classical limit is respected by the electrons and the nucleons. We suppose for simplicity that the particles are non relativistic, so the momentum p can be obtained by the expression of kinetic energy

$$E_{kin} = \frac{p^2}{2m} \approx k_B T \rightarrow p \sim \sqrt{m k_B T}.$$

The orders of magnitude for a neutron star are: $\rho \simeq 3 \cdot 10^{14}$ g cm^{-3}, which means $n_N \sim 0.1$ fm^{-3} for nucleons and $n_e \sim 10^{-3}$ fm^{-3} for electrons (we considered to have 1 electron per 100 nucleons (*1*)); $T \simeq 10^8$ K, which means $k_B T \sim 10^{-2}$ MeV.

We can now calculate for the electrons

$$\ell \sim \frac{1}{{n_e}^{1/3}} \sim 10 \text{ fm}$$

$$\lambda_T \sim \frac{\hbar c}{\sqrt{m_e c^2 k_B T}} \sim \frac{200 \text{ MeV fm}}{\sqrt{0.5 \text{ MeV } 10^{-2} \text{ MeV}}} \sim 10^3 \text{ fm}$$

and for nucleons

$$\ell \sim \frac{1}{{n_N}^{1/3}} \sim 1 \text{ fm}$$

$$\lambda_T \sim \frac{\hbar c}{\sqrt{m_N c^2 k_B T}} \sim \frac{200 \text{ MeV fm}}{\sqrt{1000 \text{ MeV } 10^{-2} \text{ MeV}}} \sim 10^2 \text{ fm.}$$

Since $\ell \ll \lambda_T$ in both cases, the electrons and the nucleons can be considered degenerate.

For the relativistic limit, we calculate for the electrons

$$\lambda_C \sim \frac{\hbar c}{m_e c^2} \sim \frac{200 \text{ MeV fm}}{0.5 \text{ MeV}} \sim 4 \cdot 10^2 \text{ fm}$$

and for nucleons

$$\lambda_C \sim \frac{\hbar c}{m_N c^2} \sim \frac{200 \text{ MeV fm}}{1000 \text{ MeV}} \sim 0.2 \text{ fm.}$$

The electrons are ultra relativistic because $\ell \ll \lambda_C$, but the nucleons are non relativistic since $\ell > \lambda_C$.

As further result, we demonstrate why we can neglect the screening effect of electrons. In fact, in the region closer to the outer crust where the cells are bigger, we calculate that the mean cell radius is less than 100 fm, while the de Broglie wavelength for electrons is ~ 1000 fm. Since the scattering wavelength is bigger than the typical cell dimension, the electrons behave as they do not feel the presence of free neutrons and nuclei.

Bibliography

1. S. L. Shapiro, S. A. Teukolsky, *Black Holes, White Dwarfs, and Neutron Stars: The Physics of Compact Objects* (Wiley-Interscience, 1983).
2. N. Chamel, P. Haensel, *Living Rev. Relativity* **11**, 10 (2008).
3. J. M. Lattimer, M. Prakash, *Science* **304**, 536 (2004).
4. J. M. Lattimer, *Annual Rev. Nucl. Part. Sci.* **62**, 485 (2012).
5. J. M. Lattimer, M. Prakash, *Astrophys. J.* **550**, 426 (2001).
6. P. B. Demorest, T. Pennucci, S. M. Ransom, M. S. E. Roberts, J. W. T. Hessels, *Nature* **467**, 1081 (2010).
7. J. M. Lattimer, M. Prakash, *Phys. Rept.* **621**, 127 (2016).
8. R. C. Duncan, C. Thompson, *Astrophys. J. L.* **392**, L9 (1992).
9. A. Colaiuda, H. Beyer, K. D. Kokkotas, *Mon. Not. R. Astron. Soc.* **396**, 1441 (2009).
10. S. Mereghetti, *A&AR* **15**, 225 (2008).
11. R. I. Epstein, *Astrophys. J.* **333**, 880 (1988).
12. K. Glampedakis, D. I. Jones, arXiv:1307.7078, (2014).
13. F. Douchin, P. Haensel, *Phys. Lett. B* **485**, 107 (2000).
14. G. Baym, C. J. Pethick, P. Sutherland, *Astrophys. J.* **170**, 299 (1971).
15. C. J. Horowitz, A. Schwenk, *Nucl. Phys. A* **776**, 55 (2006).
16. R. Nandi, D. Bandyopadhyay, *J. Phys.: Conf. Ser.* **420**, 012144 (2013).
17. L. Di Gallo, M. Oertel, M. Urban, *Phys. Rev. C* **84**, 045801 (2011).
18. J. M. Lattimer, K. A. V. Riper, M. Prakash, M. Prakash, *Astrophys. J.* **425**, 802 (1994).
19. B. K. Sharma, M. Centellas, X. Viñas, M. Baldo, G. F. Burgio, *A&A* **584**, A103 (2015).
20. A. W. Steiner, A. L. Watts, *Phys. Rev. Lett.* **103**, 181101 (2009).

21. W. G. Newton, M. Gearheart, B. A. Li, *Astrophys. J. S.* **204**, 9 (2013).

22. H. Sotani, K. Nakazato, K. Iida, K. Oyamatsu, *Phys. Rev. Lett.* **108**, 201101 (2012).

23. K. Oyamatsu, *Nucl. Phys. A* **561**, 431 (1993).

24. G. Baym, H. A. Bethe, C. J. Pethick, *Nucl. Phys. A* **175**, 225 (1971).

25. C. P. Lorenz, D. G. Ravenhall, C. J. Pethick, *Phys. Rev. Lett.* **70**, 379 (1993).

26. D. Page, S. Reddy, *Neutron Star Crust* (Nova Science Publishers, 2012).

27. N. Chamel, J. M. Pearson, S. Goriely, *ASPCS* **466**, 203 (2012).

28. G. Baym, C. J. Pethick, D. Pines, *Nature* **224**, 673 (1969).

29. C. J. Pethick, N. Chamel, S. Reddy, *Prog. Theor. Phys. Suppl.* **186**, 9 (2010).

30. N. Chamel, *Phys. Rev. Lett.* **110**, 011101 (2013).

31. B. Carter, N. Chamel, P. Haensel, *Nucl. Phys. A* **748**, 675 (2005).

32. B. Carter, N. Chamel, P. Haensel, *Int. J. Mod. Phys. D* **15**, 777 (2006).

33. J. Erler *et al.*, *Nature* **486**, 509 (2012).

34. H. Abusara, A. V. Afanasjev, P. Ring, *Phys. Rev. C* **85**, 024314 (2012).

35. K. Oyamatsu, K. Iida, *Phys. Rev. C* **75**, 015801 (2007).

36. C. J. Pethick, D. G. Ravenhall, *Ann. Rev. Nucl. Part. Sci.* **45**, 429 (1995).

37. M. Hashimoto, H. Seki, M. Yamada, *Prog. Theor. Phys.* **71**, 320 (1984).

38. J. M. Lattimer, F. D. Swesty, *Nucl. Phys. A* **535**, 331 (1991).

39. J. W. Negele, D. Vautherin, *Nucl. Phys. A* **207**, 298 (1973).

40. J. M. Lattimer, C. J. Pethick, D. G. Ravenhall, D. Q. Lamb, *Nucl. Phys. A* **432**, 646 (1985).

41. A. W. Steiner, *Phys. Rev. C* **77**, 035805 (2008).

42. E. P. Wigner, F. Seitz, *Phys. Rev.* **46**, 509 (1934).

43. N. Chamel, *Nucl. Phys. A* **747**, 109 (2005).

44. J. M. Pearson, N. Chamel, S. Goriely, C. Ducoin, *Phys. Rev. C* **85**, 065803 (2012).

45. F. Douchin, P. Haensel, *A&A* **380**, 151 (2001).

46. N. Chamel, D. Page, S. Reddy, *Phys. Rev. C* **87**, 035803 (2013).

47. D. Kobyakov, C. J. Pethick, *Phys. Rev. C* **87**, 055803 (2013).

48. W. D. Myers, W. J. Swiatecki, *Ann. Phys.* **55**, 395 (1969).

49. W. D. Myers, W. J. Swiatecki, *Ann. Phys.* **84**, 186 (1973).

50. E. Chabanat, P. Bonche, P. Haensel, J. Meyer, R. Schaeffel, *Nucl. Phys. A* **627**, 710 (1997).

51. J. M. Lattimer, *Annual Rev. Nucl. Part. Sci.* **31**, 337 (1981).

52. G. Coló, N. V. Giai, J. Meyer, K. Bennaceur, P. Bonche, *Phys. Rev. C* **70**, 024307 (2004).

53. M. Warda, X. Viñas, X. Roca-Maza, M. Centelles, *Phys. Rev. C* **80**, 024316 (2009).

54. B. M. Santos, M. Dutra, O. Lourenço, A. Delfino, *J. Phys.: Conf. Ser.* **630**, 012033 (2015).

55. D. G. Ravenhall, C. J. Pethick, J. M. Lattimer, *Nulc. Phys. A* **407**, 571 (1983).

56. N. W. Ashcroft, N. D. Mermin, *Solid State Physics* (Saunders College Publishing, 1976).

57. F. V. De Blasio *et al.*, *Phys. Rev. C* **56**, 2332 (1997).

58. S. Reddy, *Lecture 3, Physics of the Neutron Star Crust*, INT, Univ. of Washington.

59. A. Schmitt, *Introduction to Superfluidity: Field-theoretical Approach and Applications* (Springer, 2015).

60. N. Chamel, *Phys. Rev. C* **85**, 035801 (2012).

61. L. D. Landau, E. M. Lifshitz, *Theory of elasticity* (Pergamon Press, 2nd edition, 1970).

62. L. D. Landau, E. M. Lifshitz, *Fluid Mechanics* (Pergamon Press, 2nd edition, 1987).

63. T. Strohmayer, S. Ogata, H. Iyetomi, S. Ichimaru, H. M. V. Horn, *Astrophys. J.* **375**, 679 (1991).

64. S. Ogata, S. Ichimaru, *Phys. Rev. A* **42**, 4867 (1990).

65. H. Sotani, *Phys. Lett. B* **730**, 166 (2014).

66. H. Sotani, K. Iida, K. Oyamatsu, *Mon. Not. R. Astron. Soc.* **464**, 3101 (2017).

67. M. Onsi *et al.*, *Phys. Rev. C* **77**, 065805 (2008).

68. D. G. Ravenhall, C. J. Pethick, J. R. Wilson, *Phys. Rev. Lett.* **50**, 2066 (1983).

69. M. Baldo, P. Schuck, X. Viñas, *Phys. Lett. B* **663**, 390 (2008).

70. I. Tews, *Phys. Rev. C* **95**, 015803 (2017).

71. P. Danielewicz, R. Lacey, W. G. Lynch, *Science* **298**, 1592 (2002).

72. X. Roca-Maza, J. Piekarewicz, *Phys. Rev. C* **78**, 025807 (2008).

73. F. Grill, C. Providência, S. S. Avancini, *Phys. Rev. C* **85**, 055808 (2012).

74. J. W. Negele, *Phys. Rev. C* **9**, 1054 (1974).

75. D. Kobyakov, C. J. Pethick, *Phys. Rev. C* **94**, 055806 (2016).

76. A. Cumming *et al.*, *Phys. Rev. C* **95**, 025806 (2017).

77. C. J. Horowitz *et al.*, *Phys. Rev. Lett.* **114**, 031102 (2015).